Extending the Cutoff Wavelength of Thermophotovoltaic Devices via Band Structure Engineering

A dissertation submitted by

Abigail S. Licht

In partial fulfillment of the requirements for the degree of

Doctorate of Philosophy

in

Electrical and Computer Engineering

TUFTS UNIVERSITY

February 2018

ADVISOR:

Professor Thomas E. Vandervelde

ABSTRACT

Thermophotovoltaics (TPVs) convert infrared radiation, or heat, into electricity via a photovoltaic diode. While TPVs can in principle convert radiation from any heat source, in practice they have been limited to high temperature applications due to the relatively large bandgap diodes employed. Development of narrow bandgap TPV diodes is required to optimally convert longer wavelength radiation from lower temperature sources. Overcoming the intrinsic limit of these reduced bandgap diodes, however, is no trivial matter. As the bandgap of a TPV diode decreases, the intrinsic carrier concentrations and parasitic recombination increase, leading to large dark currents. The increased dark current causes the open-circuit voltage and power of the diode to drop, rendering narrow bandgap TPV diodes inoperable.

Our research aims to extend the operational cut-off wavelength of TPV devices to both a) more optimally convert the incident radiation from existing heat sources and b) enable lower temperature applications. With this goal in mind, we investigate a monovalent barrier structure, in which a wide bandgap barrier is inserted into the PN diode, for TPV devices. The barrier structure has proven successful at reducing dark currents in infrared photodetectors, which operate at low temperatures and reverse biases. TPV diodes must operate at higher temperatures, where the balance of dark current mechanisms differs. Here we explore the extent to which a monovalent barrier could be effective in reducing the dark current in narrow bandgap TPVs.

The barrier diode design is facilitated by the use of superlattice structures, which consist of alternating nanometer-scale layers of materials. Unlike bulk materials, where the electronic bands are fixed, the electronic bands of these structures can be tuned by varying the thickness and periodicity of the superlattice layers. In this work we use the 8x8 k·p method to design the band offsets for a barrier structure consisting of III-V superlattice materials. Structures were grown using molecular beam epitaxy and fabricated into diodes using standard photolithography methods. Dark current measurements were taken to examine the effect of a barrier structure on TPV performance.

ACKNOWLEDGEMENTS

First and foremost, I would like to express my sincere gratitude to Tom Vandervelde. He is an extraordinary mentor and I am grateful to have had his guidance throughout the years.

In addition to my adviser, I would also like to thank Dr. Rodolfo Salas, Dr. Kevin Grossklaus, and Professor Matt Panzer for serving on my committee; I greatly appreciate the time you took to consider my work and all of your feedback.

I would also like to thank the people on the photonic crystal project: Corey, Dante, and Emily for your work developing the PhC recipe. Thank you also to Kevin and Maggie, without whom the GenXplor would not be running.

Special thank you to all of the people of NanoMIR for graciously hosting me during my fellowship. Thank you to my Chateaubriand adviser JB and the detector team – Philippe, JPP, Marie, Remi, and Quentin. J'ai vraiment de la chance d'avoir travaillé avec une si bonne équipe!

Last but not least, I would like to thank my family and friends. Mom, Dad, Anna, Jacob, Angela & Emma – I am forever grateful for your tremendous love and support. Thank you.

TABLE OF CONTENTS

LIST OF TABLES

LIST OF FIGURES

1 Introduction

1.1 Thermophotovoltaics

Thermophotovoltaics (TPVs) convert infrared radiation, or heat, into electricity. TPVs have a wide range of applications due to the fact that they can be paired with any radiant heat source. Heat can be converted from combustion systems, radioisotopes, or high-temperature industrial processes, leading to applications in remote power supplies [1–7], deep-space power generation, [8],[9] and waste-heat recovery [10], respectively.

A TPV system consists of three main components: a heat source, an emitter, and a TPV diode, **Figure 1-1**. The heat source is typically between 1000 K and 2000 K. The emitter, which acts as an intermediate stage between the heat source and the TPV diode, allows for shaping of the radiated spectrum. The emitter can be either a blackbody that emits across all wavelengths, or a selective-emitter designed to radiate a narrow band of wavelengths tailored to the TPV diode. In addition to spectral shaping at the emitter stage, the spectrum may be further refined through filtering prior to the diode stage, **Figure 1-1**.

The core of a TPV system is the photovoltaic diode, which is the component that converts the incident radiation into usable power. The TPV diode generates a current and a voltage via the *photovoltaic effect*: if the incident light contains photons with energy greater than the bandgap of the diode, electrons may be excited from the valance band to the conduction band, where they can generate a current due to the

built-in voltage of the diode. Power is then delivered to the electrical load as the current runs through the circuit to the load. TPV diodes typically produce a current of approximately 1–3 A/cm^2 and a voltage of approximately 0.5 V for a power density of ~ 1 W/cm^2. This means that a 10x10 cm^2 array of TPV diodes can be used to generate 100+ Watts of power.

The overall TPV system efficiency is determined by the efficiency of each of the stages, and the energy transfer between the stages, **Figure 1-1**. Thus far, TPVs have demonstrated system efficiencies as high as ~20% [11]. Modeling indicates, however, that TPV system efficiencies could be even higher, as high as 40% [12], [13].

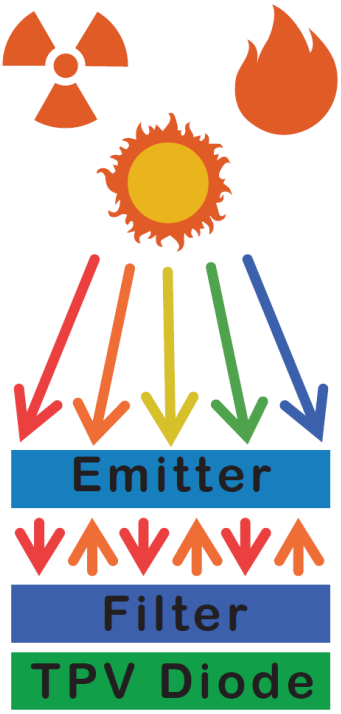

Figure 1-1: Thermophotovoltaic (TPV) system stages. Infrared radiation from a heat source is absorbed by an emitter, which re-radiates energy toward the TPV diode. This emitter stage is often designed to emit wavelengths in a narrow band matched to the TPV diode, in what is known as a selective emitter. Additional filtering may be incorporated prior to the diode stage using front-surface filters on the TPV diode. The final spectrum is then absorbed by the TPV diode, which generates a current and a voltage via the photovoltaic effect.

1.2 Extending the cutoff wavelength of TPV diodes

At present, TPV diodes are matched to only very high temperature sources (> 1000 K). This limitation stems from the bandgap of the TPV diode material. As stated previously, only photons with energy greater than the bandgap value (E_G) of the TPV diode may generate a photocurrent. Since energy is inversely proportional to wavelength, this means that a TPV diode cannot absorb radiation beyond a certain cutoff wavelength (λ_{cutoff}) determined by the bandgap value.

The cutoff wavelength of the most common TPV diode materials, gallium antimonide (GaSb) and GaInAsSb, are plotted in **Figure 1-2**, along with the spectra radiated from various temperature sources. The thermal radiation for a given temperature source is approximated by a blackbody spectrum, which is the temperature-dependent spectrum radiated by a non-reflecting body in thermal equilibrium with its surroundings. For a typical TPV temperature source, we note from **Figure 1-2** that much of the radiated spectrum is wasted since it lies beyond the cutoff wavelength of the TPV diode. A reduced, narrow bandgap diode with a longer cutoff wavelength would allow for more of the radiated spectrum to be absorbed. For example, a diode with a cutoff wavelength at 5 μm, marked by the black dotted line in **Figure 1-2**, would absorb a larger portion of the radiated spectrum from the 1000 K source than GaSb with a cutoff wavelength of 1.7 μm. Moreover, a diode with an extended cutoff wavelength could also be used to recuperate waste heat from even lower temperature sources, enabling an entirely new class of TPV applications. TPVs could then be used, for example, in the automobile industry to recycle lower temperature waste heat from car exhaust and engines. Given that narrow bandgap diodes with longer cutoff wavelengths allow for both more efficient conversion of the presently employed heat sources and extension to

lower temperature applications, this dissertation seeks to develop these narrow bandgap diodes for TPVs.

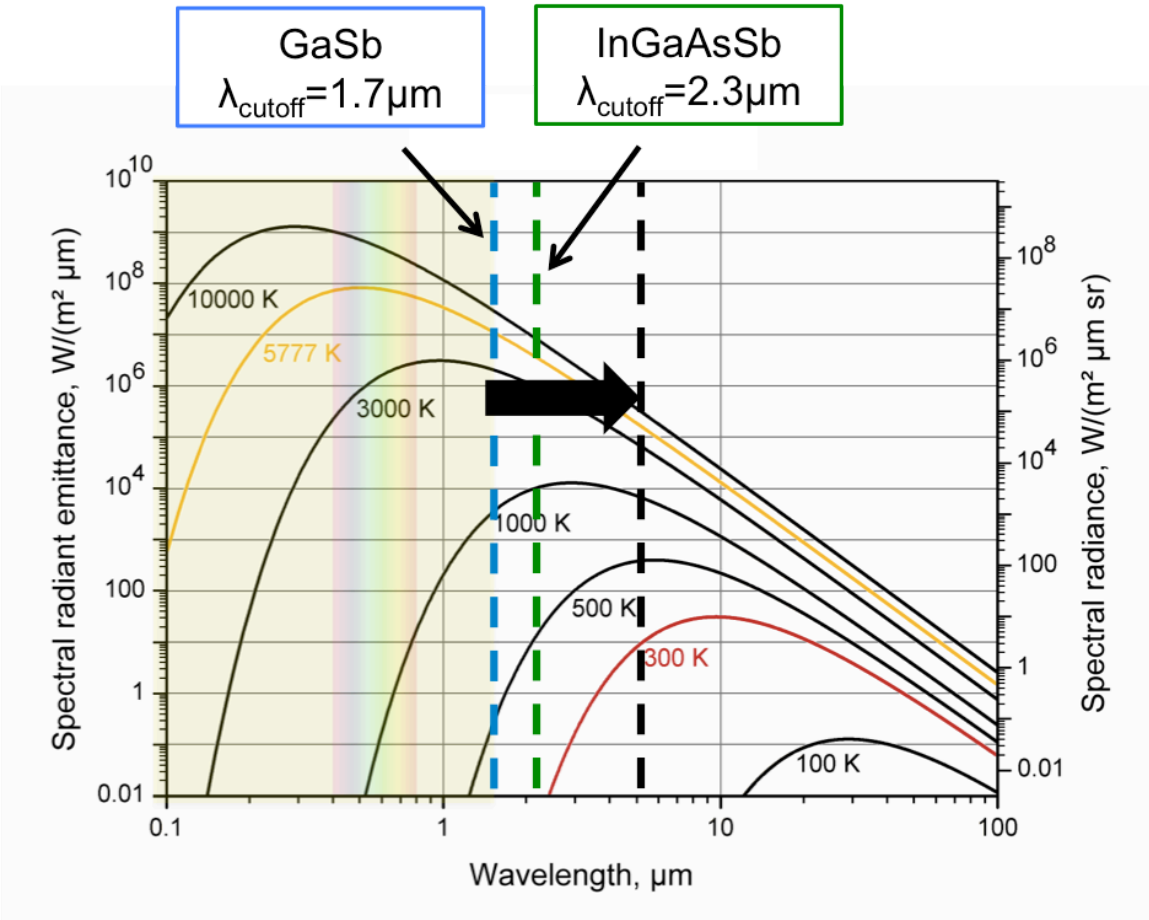

Figure 1-2: Blackbody spectrum for various source temperatures. The cutoff wavelengths of two of the most common TPV diode materials, gallium antimonide (GaSb) and the alloy InGaAsSb, are marked by the blue and green dotted lines respectively at 1.7 and 2.3 μm. If the cutoff could be extended to longer wavelengths, for example to 5 μm as shown by the black dotted line, the diode could absorb more of the radiated spectrum, yielding a higher photocurrent and conversion efficiency. A longer cutoff wavelength diode could also be used to absorb radiation from lower temperature sources, enabling new applications for TPVs. Figure adapted from reference [14].

1.3 Thesis Organization

The work in this dissertation entails designing new materials and device architectures for narrow bandgap TPVs. It also entails, to a lesser extent, developing GaSb TPV diodes with front-surface photonic crystals (PhCs). In order to provide context for the reader who does not have experience with these technologies, the necessary background is first presented in Chapter 2. In Chapter 2.1, background on photovoltaic diodes is presented, including everything from the formation of electronic bands to photovoltaic diode operation and metrics. In Chapter 2.2, a review of existing TPV diode materials is given. Lastly, in Chapter 2.3, the basic principles of photonic crystals are described.

In Chapter 3 we present the main research problems investigated in this dissertation. Chapter 3.1 details the narrow bandgap TPV diode project. Here the advantages of using narrow bandgap TPV diodes are described in full, as well as the challenges for developing these devices and our approach for overcoming these challenges. Chapter 3.2 details the GaSb/PhC project, including background on the previous work and limitations. In Chapters 4 and 5, the simulation and experimental methods are presented, respectively. Chapter 4 details the simulation methods for material and device design. Chapter 5 describes the experimental methods, which includes growth and characterization of the diode materials and fabrication and characterization of the diode devices. The results are then presented in Chapter 6 for the narrow bandgap TPV diode project and in Chapter 7 for the GaSb PhC project.

2 Background

2.1 Photovoltaic Diodes

2.1.1 Electronic Band Structure and Charge Distribution

2.1.1.1 The origin of electronic bands

The electronic bandstructure of a semiconductor material arises from the bond formations of the atoms in a crystal lattice. For a single atom, electrons can only take on specific discrete energy levels and are said to be quantized. When atoms are brought together to form a bond, their atomic orbitals will overlap. The Pauli exclusion principle, states, however, that no two particles in a quantum mechanical system can occupy the same state. As a result, upon bonding the molecular orbitals will split. This splitting continues as other atoms are brought together to form bonds, **Figure 2-1**. For a material made up of many atoms, the states form *bands* of allowed energies. Just as electrons can only occupy discrete energy levels for the single atom, these carriers can only occupy energy levels within the bands. The electrons will fill up the bands starting with the lowest energy level. The filled bands are the *valence bands* and the empty bands are the *conduction bands*.

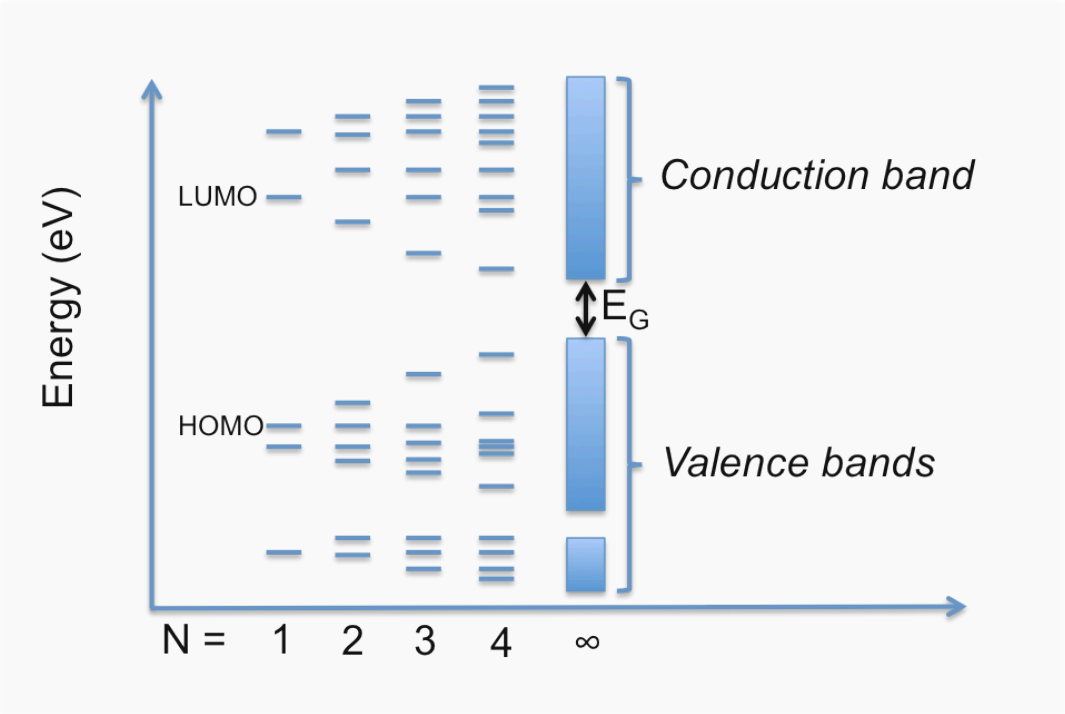

Figure 2-1: The electronic states split when atoms bond due to the Pauli exclusion principle. For a crystal material, made up of many atoms, the states form bands of allowed states. The highest unoccupied molecular orbital (HOMO) forms the valence band. The lowest unoccupied molecular orbital (LUMO) forms the conduction band. The difference in energy between these bands is the bandgap (E_G).

The energy difference between the highest valence band and lowest conduction band is the *bandgap* (E_G) of a material. This bandgap is a key parameter in determining the optoelectronic behavior of a material. If light, consisting of packets of energy as photons, contains photons with energy greater than the bandgap of the material, the energy from the absorbed photon can be imparted to an electron carrier, exciting it to the conduction band. With the electron in the conduction band, there is now the opportunity for the electron to hop into other states in the conduction band, which is necessary in order to generate a current. Additionally, when the electron is excited into the conduction band, a hole is left behind in the valence band. Electrons can move into the

empty hole state, thereby generating a current. Instead of referencing an electron moving in the valence band, the convention is to refer to the hole moving in the valence band, treating it as if it were a particle. The concept of a hole as a particle is simply a convenient fiction – it is easier to consider the motion of charge from the few holes in the valence band, than from all of the electrons.

2.1.1.2 Band structure

The allowed energy bands for charge carriers in a crystalline material can be calculated using the time-independent Schrodinger's equation, Equation **2-1**, where E_n is the energy value of band n, Ψ is the wave function, p is the momentum operator, V is the potential, and m is the carrier mass. Since carriers in a material will experience a periodic potential from the crystal lattice, the wave function psi can be written as a Bloch wave, Equation **2-2**, which is the product of a plane wave $e^{ik\cdot x}$ and the periodic function $u_{n,k}(x)$, Here k is the wave vector, n is the band index, and u_{nk} is a function with the same periodicity as the crystal lattice.

$$E_n\psi_n = \left(\frac{p}{2m} + V\right)\psi_n \qquad 2\text{-}1$$

$$\psi_{n,k}(x) = e^{ik\cdot x}u_{n,k}(x) \qquad 2\text{-}2$$

These equations can be used to solve for the energy levels of different bands. We can then plot the energy bands for different wave vector values, E(k). In Figure **Figure 2-2**, an example is given of the band structure E(k) of a zinc blend material. The energy value is plotted for k values between points of high symmetry in the crystal lattice, which are represented by the Brillouin zone, **Figure 2-2**. These plots are valuable

because they give information, such as, for example, the effective mass of a carrier. While an electron has some mass m_0, the forces experienced by the electron as it moves through the crystal structure will alter this mass. The effective mass can be calculated from second derivative of the E(k) diagram. For example, at the valence band maximum at the zone center, we observe two bands – the heavy (HH) and the light hole (LH) bands. The heavy hole band corresponds to the band with the larger effective mass, or the less steep slope in the E(k) diagram.

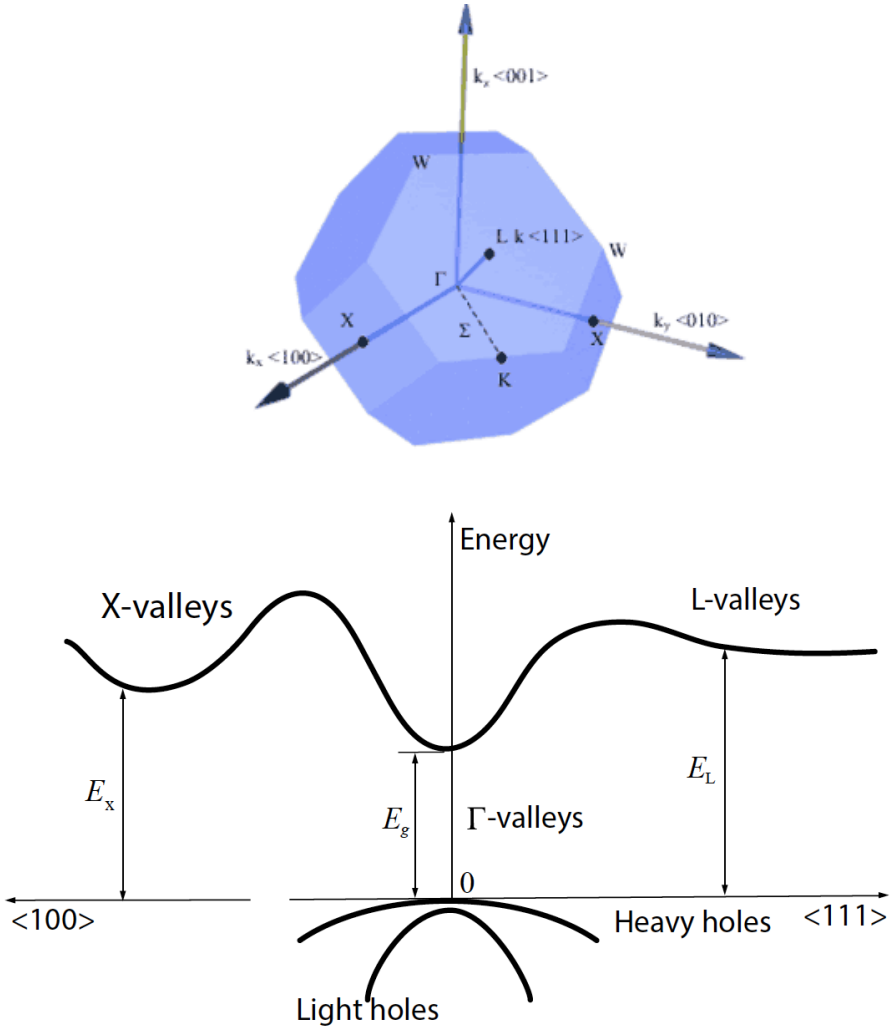

Figure 2-2: (top) Brillouin zone of a face-centered cubic (fcc) crystal system and points of high symmetry (schematic from ref. [15]). (bottom) example of band structure E(k) for zinc blend material.

The electronic band diagram also yields information such as the bandgap of the material. A material is said to have a direct bandgap if the lowest energy gap between the conduction band and the valence band occurs at the gamma point. For a direct bandgap material, many of the optical and electrical properties result from the primary transition at the gamma point. When examining the optoelectronic properties of a device we will therefore often only plot the conduction and valence band values around the gamma point.

2.1.1.3 Density of States

For a bulk material, the density of electronic states in the conduction and valence bands, $g_c(E)$ and $g_v(E)$, is given by Equations **2-3** and **2-4**, where h is Planks constant and m_e^* and m_h^* are the electron and hole effective masses, respectively.

$$g_c(E) = \frac{4\pi(2m_e^*)^{3/2}}{h^3}\sqrt{E - E_c} \qquad 2\text{-}3$$

$$g_v(E) = \frac{4\pi(2m_h^*)^{3/2}}{h^3}\sqrt{E_v - E} \qquad 2\text{-}4$$

While these equations describe how the electronic states are distributed as a function of energy, they do not reveal whether the states are occupied or unoccupied. The probability that a state with energy E will be occupied by an electron is given by the Fermi-Dirac probability distribution f(E), Equation **2-5**, where k_B is Boltzmann's constant,

T is the temperature, and E_F is the Fermi energy level. The Fermi energy level represents the energy level at which, under thermodynamic equilibrium, the energy level has a 50% probability of being occupied at any given time. The probability that a state is occupied by a hole is then given by 1-f(E).

$$f(E) = \frac{1}{1 + \exp\left(\frac{E - E_F}{k_B T}\right)} \quad \text{2-5}$$

If the quantity (E - E_F) is much greater than the thermal energy $k_B T$, the Maxwell-Boltzmann approximation can be made; the probability that a state is filled by an electron or a hole is then given by Equations **2-6** and **2-7**.

$$f(E) \approx \exp\left(\frac{E - E_F}{k_B T}\right) \quad \text{2-6}$$

$$1 - f(E) \approx \exp\left(\frac{E_F - E}{k_B T}\right) \quad \text{2-7}$$

The *total* density of electrons and holes, *n* and *p*, can be calculated by integrating the product of the density of states with the Fermi distribution, Equations **2-8** and **2-9**. Carrying out this integration, we can express the electron and hole concentrations by Equations **2-10** and **2-11**, where N_C and N_V are the *effective* conduction and valence band density of states.

$$n = \int_{E_C}^{\infty} g_c(E) f(E) dE \quad \text{2-8}$$

$$p = \int_{-\infty}^{E_V} g_v(E)[1 - f(E)]dE \qquad 2\text{-}9$$

$$n = N_C \exp\left(\frac{E_F - E_C}{k_B T}\right) \qquad 2\text{-}10$$

$$p = N_V \exp\left(\frac{E_V - E_F}{k_B T}\right) \qquad 2\text{-}11$$

$$N_c = 2\left(\frac{m_e^* k_B T}{2\pi\hbar^2}\right)^{3/2} \qquad 2\text{-}12$$

$$N_v = 2\left(\frac{m_h^* k_B T}{2\pi\hbar^2}\right)^{3/2} \qquad 2\text{-}13$$

For a semiconductor material at equilibrium, the product of the electron and hole carrier concentrations is constant and determines a material property known as the intrinsic carrier concentration, n_i, Equation **2-14**. The intrinsic carrier concentration can be viewed as the number of electrons thermally excited into the conduction band of semiconductor (or conversely the number of holes left behind in the valence band). From Equation **2-15**, we see that the intrinsic carrier concentration increases with growing temperatures and decreases for increasing bandgap values.

$$n_i{}^2 = np = N_c N_v e^{-\frac{E_g}{k_B T}} \qquad 2\text{-}14$$

$$n_i = \sqrt{N_c N_v}\, e^{-\frac{E_g}{2k_B T}} \qquad 2\text{-}15$$

2.1.1.4 Doping

At equilibrium, a semiconductor material will have the same number of electrons and holes, and the material is said to be intrinsic. A material can be made "extrinsic" through a process known as doping, in which impurity atoms are added to the material in a precise manner so as to introduce additional electron or hole carriers. Since the addition of these other atoms creates new bonds, the distribution of the electronic energy levels will be altered. *Doping is, therefore, what allows us to control the electronic properties of a material*.

For example, a negatively doped or "n-type" material is created by adding a large amount of *donor* atoms that contain extra bonding electrons. These donor atoms create extra energy states near the conduction band edge. As the energy difference between these introduced impurity levels and the conduction band edge is small, at room temperature the electrons from these donor atoms are excited to the conduction band. Since more electrons are in the conduction band, the Fermi level will shift upward for an N-type material (Figure 2-3, left).

Similarly, doping a material with *acceptor atoms*, which contain fewer electrons, forms a positively doped "p-type" material. Doping with acceptor atoms creates energy states near the valence band edge. At room temperature, these atoms ionize, as electrons from the valence band move to fill these holes. We can also think of this process as holes moving into the valence band. Since more holes are in the valence band, the Fermi level shifts downward (Figure 2-3, right).

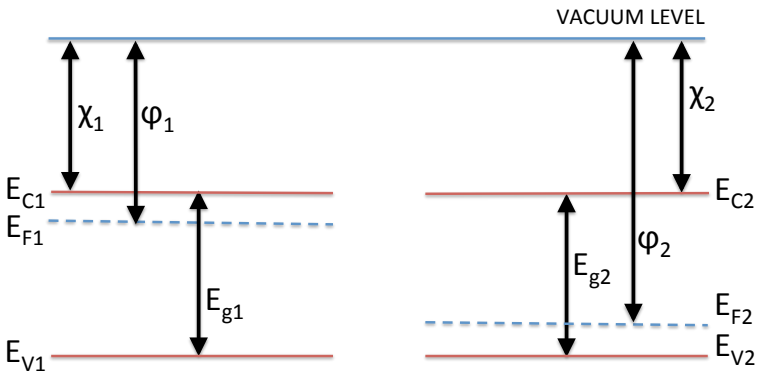

Figure 2-3: N-type (left) and p-type (right) band structures. In an n-type material, the doping of donor atoms shifts the Fermi level upward. In a p-type material, the doping of acceptor atoms shifts the Fermi level downward.

2.1.2 The PN Junction

Upon interfacing a p-type and n-type material together to form a junction, the excess electrons from the n-type material will diffuse into the p-type material, recombining with holes as they diffuse. Likewise, excess holes of the p-type material will diffuse into the n-type material, recombining with electrons as they diffuse. As the carriers recombine, positive ions are uncovered in the n-type region and negative ions are uncovered in the p-type region. The region of ions forms the space charge region (SCR), also called the depletion region, since the charge carriers have been depleted in this region. The remaining positive and negative ions will cause an electric field to be set up at the junction.

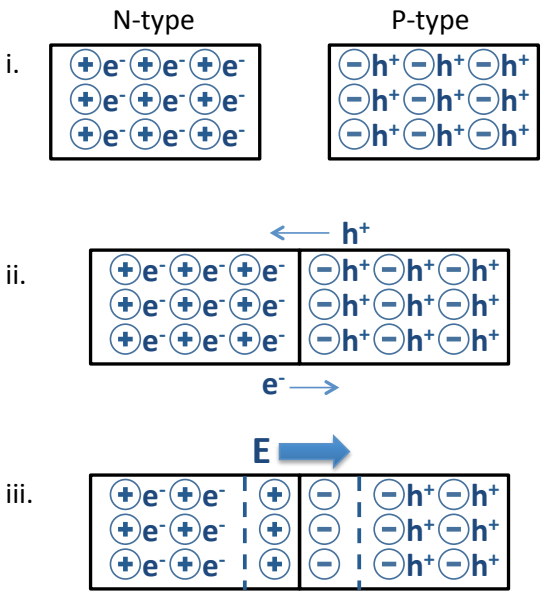

Figure 2-4: i. Isolated n-type and p-type materials ii. Upon interfacing an n-type and p-type material, electrons from the n-type material will diffuse into the p-type material, recombining with holes, while holes from the p-type material will diffuse into the n-type material, recombining with electrons iii. Positive ions are uncovered in the n-type region; negative ions are uncovered in the p-type region. An electric field is set up within the depleted region.

Since the Fermi level remains constant in equilibrium under zero applied bias, the bands of the n-type and p-type materials will bend upon formation of the junction, Figure 2-5. The electric field at the junction will extend over the entire band bending region.

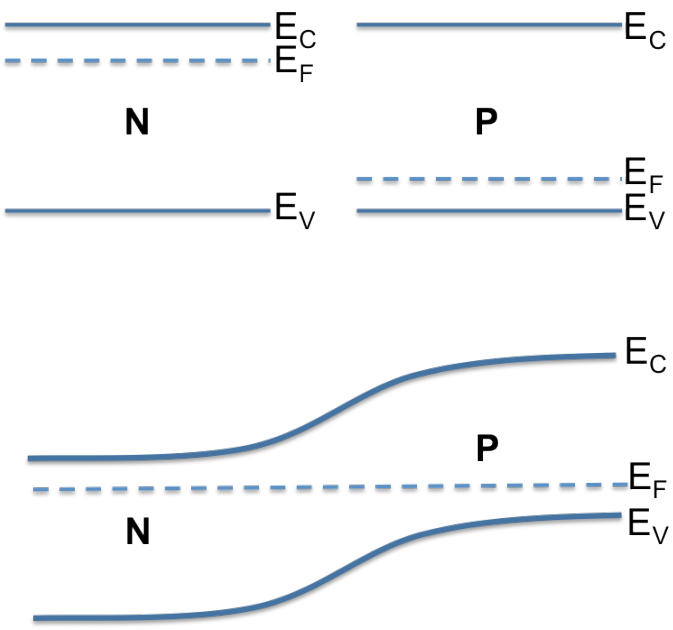

Figure 2-5: Band diagrams for isolated n-type and p-type materials (top) and a PN homojunction (bottom). For the n-type material, the Fermi level (E_F) is close to the conduction band edge (E_C). For the p-type material, the Fermi level is close to the valence band edge (E_V). The Fermi level remains constant for any material under zero bias under equilibrium; thus, when the p-type and n-type materials are combined to form a junction, band bending occurs at the interface. The built-in potential and electric field occur throughout the band-bending region.

2.1.3 The Ideal Diode

The interfacing of the p-type and n-type materials forms a PN diode. The built-in potential and doping profile of the diode result in a drift and diffusion current, respectively, Figure 2-6. The diffusion current results from *majority* carriers, electrons in the n-region (N_D) and holes in the p-region (N_A), with enough energy to overcome the barrier and move across the junction. The drift current consists of *minority* carriers, electrons in the p-region ("n_p") and holes in the n-region ("p_n"), within a diffusion length of

the depletion region. When these carriers diffuse to the depletion region, they are swept up by the electric field in this region, generating a current, Figure 2-6. This current depends on the product of the concentration of minority carriers with the carrier's effective velocity, which is the ratio of the diffusivity *D* to the diffusion length *L*, Equation 2-16. The diffusivity is proportional to the mobility (μ) and is given by Equation **2-17**. The diffusion length is proportional to the square of the diffusivity and the minority carrier lifetime τ, Equation 2-18. Using the fact that $np=n_i^2$, (and therefore $N_D p_n=n_i^2$ and $N_A n_p=n_i^2$) the drift current can be rewritten in terms of the intrinsic carrier concentration and the doping, Equation 2-19.

$$I_0 = qA\left(\frac{D_n}{L_n}n_p + \frac{D_p}{L_p}p_n\right) \qquad 2\text{-}16$$

$$D_{n,p} = \frac{kT}{q}\mu_{n,p} \qquad 2\text{-}17$$

$$L_{n,p} = \sqrt{D_{n,p}\tau_{n,p}} \qquad 2\text{-}18$$

$$I_0 = qA\left(\frac{D_n}{L_n}\frac{n_i^2}{N_A} + \frac{D_p}{L_p}\frac{n_i^2}{N_D}\right) \qquad 2\text{-}19$$

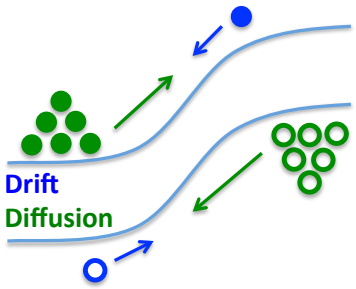

Figure 2-6**:** Schematic of the drift and diffusion currents. Electrons are represented by solid circles and holes are represented by open circles. Minority carriers, which generate a drift current, are shown in blue. Majority carriers, which generate the diffusion current, are shown in green. At zero applied bias, there is no net current and these current mechanisms are equal.

At zero applied bias, the drift current and diffusion current balance each other precisely. If a reverse bias is applied to the PN junction, the barrier height increases, blocking the flow of majority carriers. Minority carriers that diffuse to the depletion region still flow, generating a reverse bias current. Since the drift current is limited by the probability of a minority carrier reaching the SCR, and not the strength of the electric field, this current is essentially independent of the applied voltage and saturates after a few kT/q. This current is therefore known as the diode saturation current (I_0).

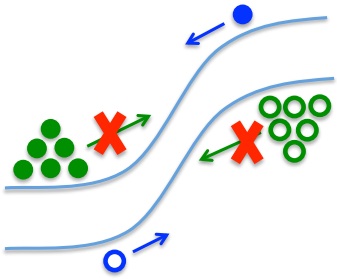

Figure 2-7: Diode current mechanisms in reverse bias. Electrons are represented by solid circles and holes are represented by open circles. Minority carriers, which result in a drift current, are shown in blue. The high potential barrier in reverse bias blocks majority carriers that make up the diffusion current. The current in reverse bias is therefore entirely minority carrier driven.

An applied forward bias decreases the barrier height. Here the same small number of minority carriers that diffuse into the depletion region remains constnat, but now more majority carriers are able to overcome the barrier, injecting themselves across the SCR where they become minority carriers. As the injected carriers diffuse further into the material, they recombine with majority carriers. As such, a gradient of minority carriers results in the flatband region at the edge of the depletion region, generating a diffusion current. This current increases exponentially with increasing bias.

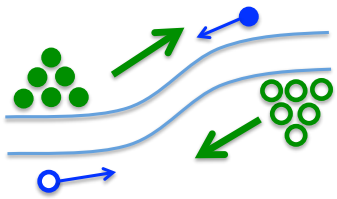

Figure 2-8**:** Diode current mechanism in forward bias. Electrons are represented by solid circles and holes are represented by open circles. Minority carriers, which result in a drift current, are shown in blue. The barrier height decreases with increasing applied forward bias, and the diffusion current due to the majority carrier injection increase exponentially.

Since the PN junction has only a very small current in reverse bias and a large current in forward bias, it exhibits a rectifying behavior, Equation **2-20**. The current-voltage curve looks like that in Figure 2-9. Substituting in the saturation current, the ideal diode current is written as Equation 2-21:

$$I_{ideal} = I_0\left(e^{\frac{qV_A}{kT}} - 1\right) \qquad 2\text{-}20$$

$$I_{ideal} = qAn_i^2\left(\frac{D_n}{L_n}\frac{1}{N_A} + \frac{D_p}{L_p}\frac{1}{N_D}\right)\left(e^{\frac{qV_A}{kT}} - 1\right) \qquad 2\text{-}21$$

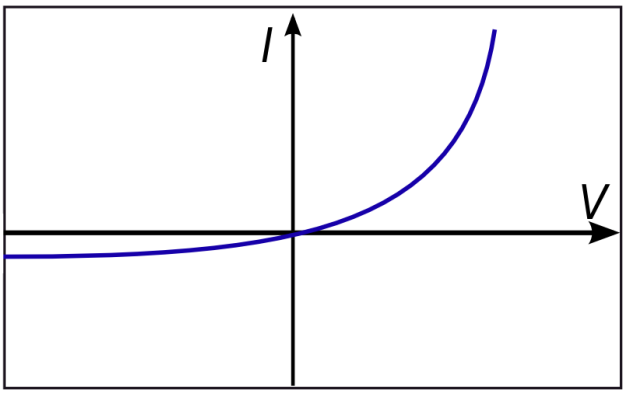

Figure 2-9**:** Current-voltage curve for an ideal diode. For reverse bias, the diode quickly approaches the saturation current. For forward biases, the current increases exponentially with increasing voltage.

2.1.4 Deviations from Ideality

In the previous section, we described the ideal diode current, which is due to drift and diffusion of carriers from *the flatband regions* of the diode. The ideal diode equation is accurate for diodes at low temperatures; however, at non-zero temperatures, parasitic thermal generation-recombination (GR) processes within *the depletion region* generate an additional current. The total current is then the sum of the ideal current (referred to henceforth as the diffusion current) and the GR current, Equation 2-22. Since the curve may differ in shape from that of the ideal curve, here we introduce the ideality factor *n* into Equation **2-23**. For the ideal diode n was assumed to be 1. For a practical diode, n is typically between 1 and 2 and varies as a function of voltage.

$$I_0 = I_{DIFF} + I_{GR} \qquad 2\text{-}22$$

$$I(V,T) = I_0\left(e^{\frac{qV}{nkT}} - 1\right) \qquad 2\text{-}23$$

The GR current is calculated by integrating the recombination rate across the depletion region and multiplying by the carrier charge q, Equation 2-24. Several types of recombination may occur, including radiative, Auger, and Shockley-Read-Hall. These recombination mechanisms are depicted in Figure 2-10 and are described in the following section.

$$I_{GR} = -qA\int_{-x_p}^{x_n} U_{GR}\,dx \qquad 2\text{-}24$$

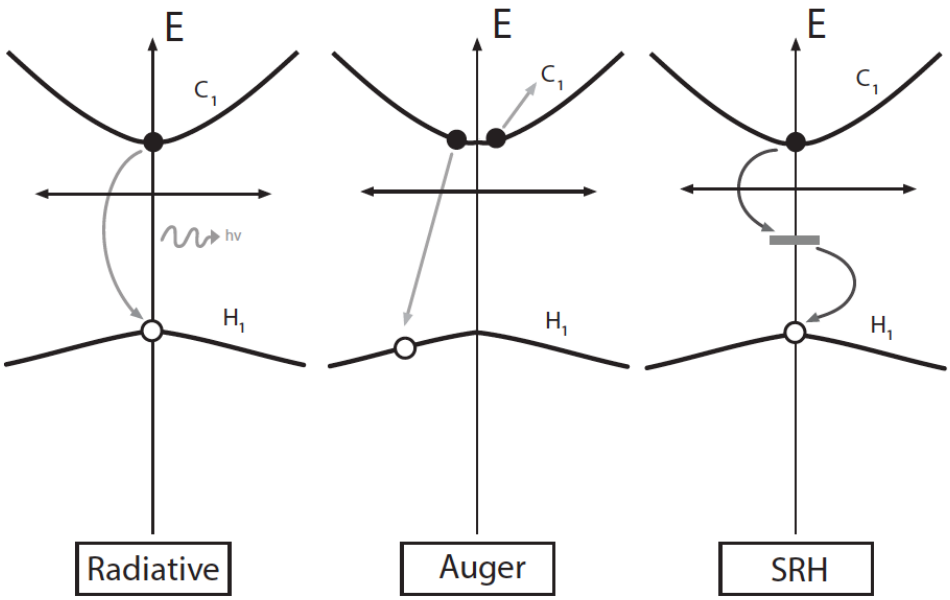

Figure 2-10: Types of recombination including (left) radiative, (center) Auger, (right) Shockley-Read-Hall

Radiative

In radiative recombination, an electron from the conduction band directly recombines with a hole in the valence band, releasing a photon. Radiative recombination occurs primarily in direct bandgap semiconductors and can be neglected in indirect semiconductors. The radiative recombination rate is given by Equation 2-25, where B_{rad}, the radiative recombination coefficient, is a property of the material.

$$U_{rad} = B_{rad}(np - n_i^2) \quad \text{2-25}$$

Auger

In Auger recombination, the collision of two carriers causes one to be excited to a higher energy and the other to recombine with a third carrier. Auger recombination is important in materials with low bandgaps and high intrinsic carrier concentrations where carrier interactions are stronger. For GaSb-based materials with bandgaps less than 0.5 eV, Auger recombination is the main non-radiative process at room temperature and limits the open-circuit voltage [16] [17]. The net Auger recombination rate is given by Equation 2-26 in which C_n and C_p are the electron and hole Auger coefficients respectively.

$$U_{Aug} = (C_n n + C_p p)(np - n_i^2) \quad \text{2-26}$$

Shockley-Read-Hall (SRH)

Shockley-Read-Hall (SRH) occurs due to defects in the crystal lattice which create trap states or recombination centers and is often the dominant mechanism of recombination in practical devices. SRH recombination is a two-step process. First an electron moves into a trap state; then if a hole moves to the same state, the electron and

hole recombine. The SRH recombination rate is given by Equation 2-27 and is dependent on the SRH carrier lifetimes defined by Equations 2-28 and 2-29, in which ν is the mean thermal velocity, σ is the capture cross section, and N_t is the density of trap states.

$$U_{SRH} = \frac{(np - n_i^2)}{\tau_{n,SRH}(p + p_t) + \tau_{p,SRH}(n + n_t)} \quad 2\text{-}27$$

$$\tau_{n,SRH} = \frac{1}{\nu_n \sigma_n N_t} \quad 2\text{-}28$$

$$\tau_{p,SRH} = \frac{1}{\nu_p \sigma_p N_t} \quad 2\text{-}29$$

2.1.5 Variation of Diode Current with Temperature

For low temperature device operation, the GR current is orders of magnitude greater than the diffusion current. However, as the diode temperature increases, the diffusion current becomes greater than the GR current. This is because while the GR current is proportional to the intrinsic carrier concentration, the diffusion current is proportional to the intrinsic carrier concentration *squared*. The dominant diode current mechanism therefore depends on the temperature of operation of the diode, as illustrated in Figure 2-11.

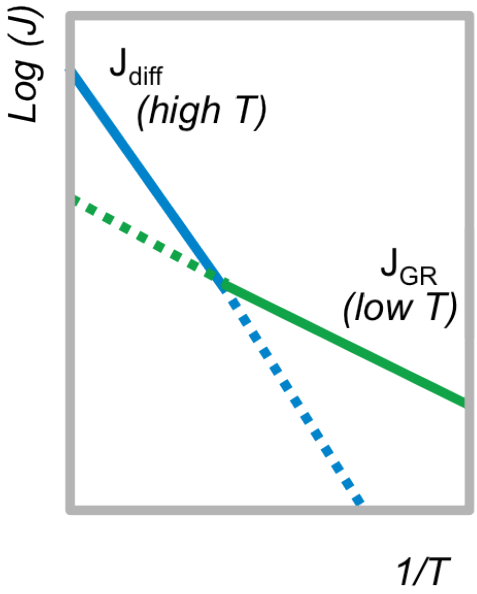

Figure 2-11: Arrhenius plot of dark current mechanisms versus temperature. Diffusion current (blue line) is the dominant current for high temperature operation while generation-recombination current (green line) is the dominant current for low temperature operation.

2.1.6 Photocurrent

Thus far, we have described the current-voltage characteristics of a diode. A photovoltaic cell is a photodiode - a diode designed specifically to allow light, consisting of packets of energy called photons, to travel through the device to the space charge region. If a photon has energy greater than the bandgap energy, upon absorption, an electron may be excited from the valence band to the conduction band, generating an electron hole pair (ehp), **Figure 2-12**. The electron and hole are then swept up by the electric field of the diode, generating a photogenerated current. For a photogeneration rate given by G_L, the current density generated due to photo-absorption is the product of

the carrier charge q, the width of the depletion region W, and the photogeneration rate G_L, Equation **2-30**.

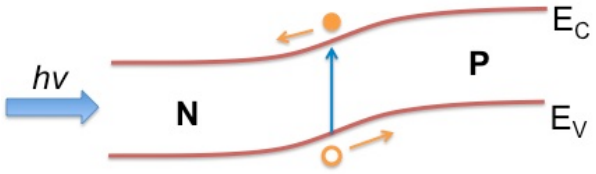

Figure 2-12: Photogenerated current in a PV diode. Light (here shown as *hv*) with energy greater than the bandgap may excite an electron to the conduction band, creating an electron-hole pair (ehp). The electric field of the diode will then sweep the electron and hole in opposite directions, generating a photocurrent.

$$J_{light} = -qWG_L \tag{2-30}$$

The total current of the photodiode is the summation of the original diode current discussed previously, hereafter referred to as the dark current, with the photogenerated current, Equation **2-31**. Since the photogenerated current is approximately constant for all voltages, the total current is a shifted version of the dark current curve, Figure 2-13.

$$J_{total} = J_{light} + J_{dark} \tag{2-31}$$

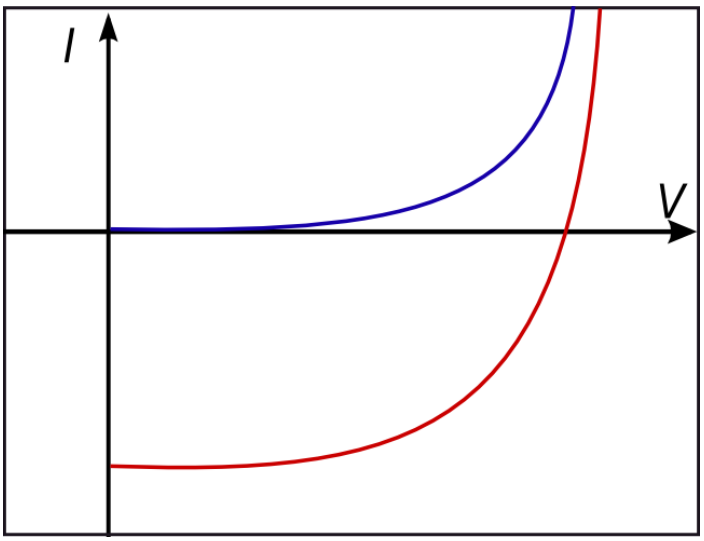

Figure 2-13: Current-voltage plot of a photodiode in the dark (blue curve) and light (red curve).

2.1.7 Power Metrics

It is convention by the PV community to flip the curve in **Figure 2-13** across the x-axis so that the power characteristics may be shown in the first quadrant, **Figure 2-14**. In this figure several important PV diode metrics are depicted. The short-circuit current (J_{SC}) is the current value when the voltage is zero. Since the dark current mechanisms are in equilibrium when the voltage is zero, the short-circuit current is equal to the photogenerated current. Substituting in J_{SC} and the dark current into Equation **2-31**, the total current can be rewritten as Equation **2-32**.

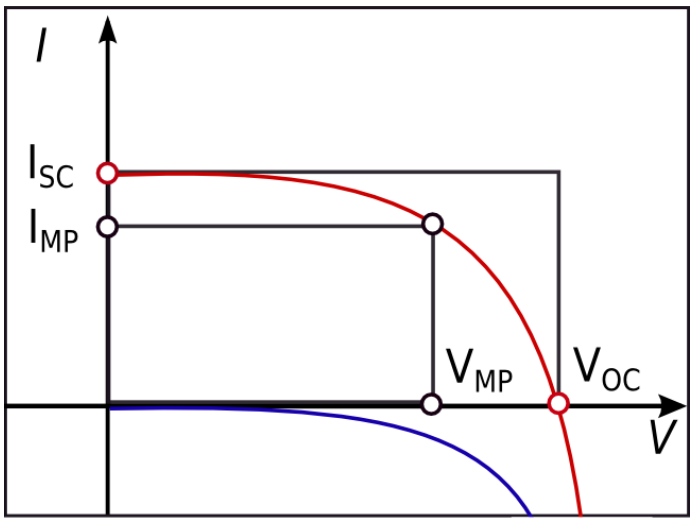

Figure 2-14: Current-voltage plot of a diode in the dark (blue curve) and light (red curve). The short-circuit current J_{SC} is the value of the current when the voltage is zero. The open circuit voltage (V_{OC}) is the voltage when the total current is zero, or when the dark current equals the photo-generated current. The maximum power point is the point (J_M, V_M), where the product of these values gives the maximum obtainable power.

$$J_{total} = J_{SC} - J_0\left(e^{\frac{qV}{kT}} - 1\right) \qquad 2\text{-}32$$

The open-circuit voltage (V_{OC}) is the voltage that occurs when the contacts are isolated and there is no current flow, **Figure 2-14**. The open-circuit voltage can be calculated by setting the total current in Equation **2-32** equal to zero and solving for V_{OC}; the V_{OC} is then given by Equation 2-33 and is proportional to the short-circuit current and inversely proportional to the dark current.

$$V_{OC} = \frac{kT}{q} ln\left(\frac{J_{SC}}{J_0} + 1\right) \qquad 2\text{-}33$$

A common metric for characterizing the performance of a PV cell is the fill-factor (FF) - the ratio of the maximum power to the product of the open-circuit voltage and the short-circuit current. The maximum power occurs at the point (J_{MP}, V_{MP}), **Figure 2-14**. Graphically, the fill factor is the ratio of the area of the small rectangle in **Figure 2-14** (from the product of J_{MP} *and* V_{MP}) to the area of the larger rectangle (from the product of J_{SC} *and* V_{OC}). The fill factor of most well performing diodes is ~70%.

$$FF = \frac{J_{MP}V_{MP}}{J_{SC}V_{OC}} \qquad 2\text{-}34$$

The efficiency of the cell is given by the ratio of the maximum power to the input power, and can be written in terms of the fill factor, Equation 2-35. We note that it is ideal to have as high of a short-circuit current, open circuit voltage, and fill factor as possible. Another efficiency metric is the voltage factor V_F, which is the ratio of the open circuit voltage to the bandgap. This metric provides a measure of how well the device exploits the PN junction potential. Similar to fill factor, the voltage factor cannot be equal to one since the open circuit voltage is always less than the bandgap value.

$$\eta = \frac{J_{MP}V_{MP}}{P_{in}} = \frac{J_{SC}V_{OC}FF}{P_{in}} \qquad 2\text{-}35$$

$$V_F \equiv \frac{V_{OC}}{E_G} \qquad 2\text{-}36$$

2.1.8 Responsivity and Quantum Efficiency

In an ideal photovoltaic diode, all above bandgap photons would be absorbed. However, in a practical device, not every impingent above-bandgap photon will contribute to the final output current due to various loss mechanisms. These loss mechanisms could be external, for example from photons being reflected at the front surface, or internal, such as due to recombination of carriers as discussed in Section 2.1.4

Two related metrics for quantifying these losses are the responsivity (R) and the quantum efficiency (QE), which both quantify the current as a function of wavelength. The responsivity is the photocurrent generated per unit optical power incident on the photodiode, Equation **2-37**, and has units of A/W.

$$R(\lambda) = \frac{I(\lambda)}{\mathrm{P}(\lambda)} \qquad \text{2-37}$$

The quantum efficiency is a similar metric, but is based on the number of electrons generated. The external quantum efficiency (EQE) is the number of electrons generated over the total number of photons incident on the cell, Equation **2-38**. The EQE can be re-written as the current per unit of electric charge over the power per unit energy of photon. The EQE can then be related to the responsivity by Equation **2-39**. The internal quantum efficiency (IQE) is the number of electrons generated over the number of photons *absorbed*, Equation **2-40**, and is related to the EQE by **2-41**.

$$EQE(\lambda) = \frac{electrons/sec}{incident\ photons/sec} \qquad \text{2-38}$$

$$EQE(\lambda) = \frac{I(\lambda)/q}{\mathrm{P}(\lambda)/hv} = R(\lambda)\frac{hv}{q} = \frac{R(\lambda)}{\lambda}\frac{hc}{q} = \frac{R(\lambda)}{\lambda} * (1240\ W\ nm/A) \quad \text{2-39}$$

$$IQE(\lambda) = \frac{electrons/sec}{absorbed\ photons/sec} \quad \text{2-40}$$

$$IQE(\lambda) = \frac{EQE}{1 - Reflection - Transmission} \quad \text{2-41}$$

2.1.9 Circuit Model

A photovoltaic (PV) cell can be modeled as a current source in parallel with a diode. The total current going to the load is approximated as the photo-generated current minus the dark current as in Equation 2-31. This equation can be modified to account for internal parasitic resistances, Equation 2-42. The modified equation includes the series (R_s) and shunt (R_{sh}) resistances, as shown in Figure 2-15. The series resistance may be caused by losses through the front surface of the cell or through the metal contacts, reducing the overall voltage. The shunt resistance occurs if current is given an alternate path, such as due to recombination or leakage currents, reducing the overall current. For an ideal cell, the series resistance would be zero, resulting in no further voltage drop before the load, and the shunt resistance would be infinite meaning that stray currents are eliminated.

$$J(V) = J_{SC} - J_0\left(e^{\frac{q(V+IR_S)}{nkT}} - 1\right) - \frac{V + J_0\,R_S}{R_{SH}} \quad \text{2-42}$$

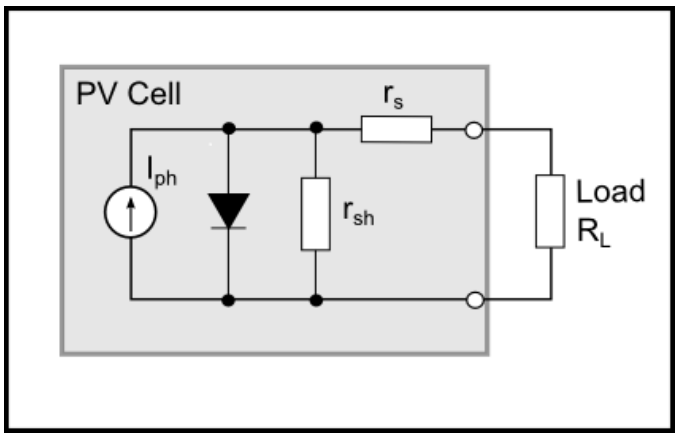

Figure 2-15: Circuit diagram for photovoltaic cell including series and shunt resistances.

2.1.10 Schottky versus Ohmic Contacts

Thus far, we have detailed the physics of semiconductor homojunctions. Another important junction in the TPV diode is the metal-semiconductor junction at the contacts. This junction must be considered in the device design, as poor pairing of the metal and semiconductor materials may create an undesirable barrier for photogenerated carriers. This can be understood by examining the band alignment at the metal-semiconductor junction. The band offset at this junction is determined by the difference in the work function of the metal and the semiconductor material. For example, consider the case of paring a metal with an n-type semiconductor material. When the n-type semiconductor is brought into contact with a metal with a higher work function, upon alignment of the Fermi levels, band bending will create a barrier (**Figure 2-16**, right) in what is known as a Schottky contact. On the other hand, if an n-type material is paired with a metal with a lower work function, no barrier will form and the current-voltage characteristics will be linear, in what is known as an ohmic contact. An ohmic contact is desirable since it does not block collection of any of the photogenerated carriers from the diode.

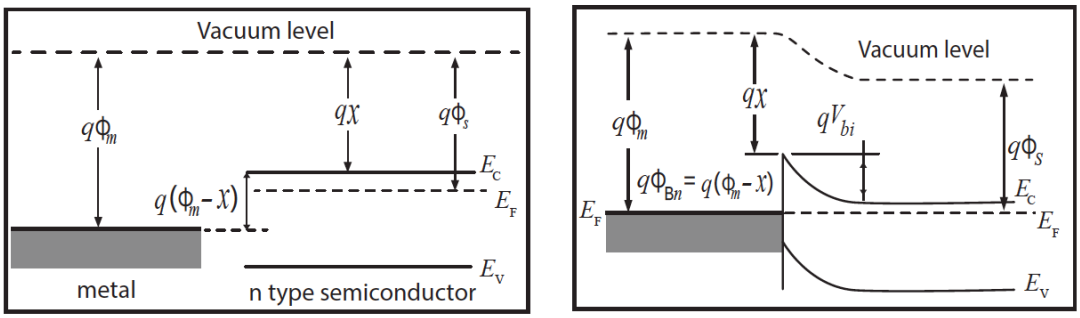

Figure 2-16: (left) Energy band diagram of an isolated metal and an isolated n-type semiconductor. Φ_M is the work function of the metal, Φ_S is the work function of the semiconductor, and **x** is the electron affinity of the semiconductor. (right) Energy band diagram of metal and semiconductor after they have been brought into contact and reached equilibrium. The Schottky barrier height, $q\Phi_B$, is equal to $q^*(\Phi_B - \mathbf{x})$.

2.2 TPV Diode Materials and Performances

2.2.1 Origins

Much of the progress in TPVs has stemmed from developments in the field of photovoltaics. The first implementation of TPV was in the mid-1950's when Henry Kolm of MIT Lincoln Laboratory held a silicon solar cell up to a lantern in an attempt to generate electricity from a flame [18], making silicon the first diode material used in TPVs. Silicon, however, has a bandgap of 1.12 eV and cutoff wavelength ~1.1 μm. This wavelength is the peak wavelength of a 6,000K blackbody, which is approximately the temperature of the Sun. Silicon is therefore ideal for solar applications, but poor for TPV applications with lower source temperatures of ~ 1,000-2,000 K. In order to employ silicon in TPV applications, silicon must be paired with selective emitters such as ytterbia, Yb_2O_3, to tailor the spectrum to the silicon diode [19], [20].

Germanium, a common bottom cell material from multi-junction solar cells, has also been investigated as a possibility for TPV diodes [21]. Germanium is a better match for TPV applications than silicon, since germanium has a lower bandgap of 0.66eV and absorbs wavelengths out to 1.88 μm [20]. However, germanium is still an indirect bandgap material and has generally poor performance.

2.2.2 III-Vs and their alloys

With the exception of the group IV materials discussed previously, the majority of TPV diodes consist of III-V materials, which contains atoms from group III and V of the periodic table, **Figure 2-17**. Materials used include binaries such as InAs and GaSb and their alloy derivatives. While binaries are easier to produce, alloys allow for more

possibilities since in theory they can be used to create any bandgap value within the range of the binary values, **Figure 2-18**. In practice, however, the alloys that can be used are often limited to the composition that is lattice-matched to the available substrates, which include: InAs, InP, and GaSb. Lattice matching is crucial because if the material and substrate are not matched, defects may occur during the growth of the material that will decrease the performance of the TPV diode.

Figure 2-17: Selection from the periodic table highlighting the group III and V elements incorporated into TPV diode materials.

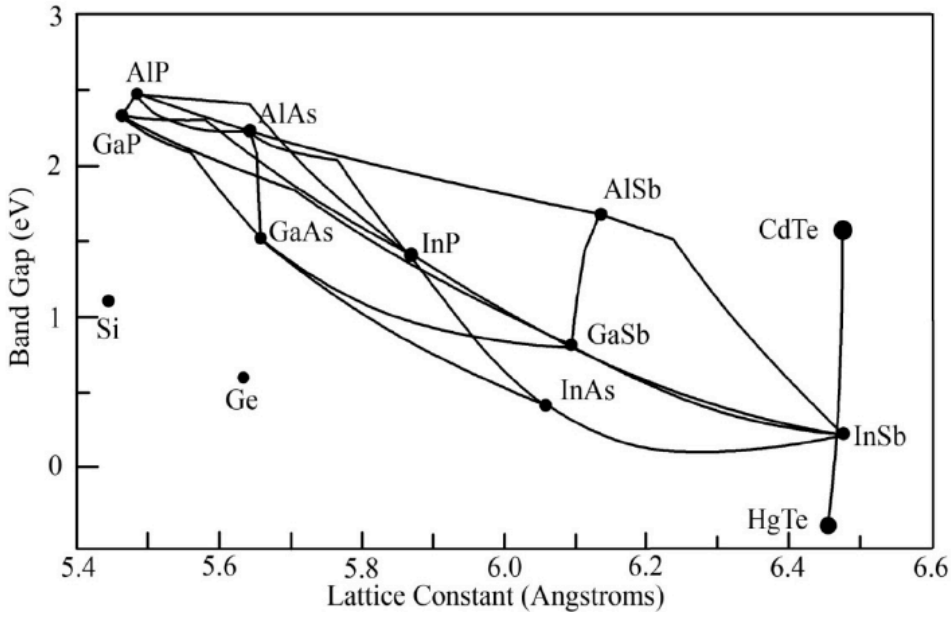

Figure 2-18: Bandgap versus lattice parameter for various materials [22]. Lines between materials show the bandgap for the alloy materials. With the present technology we are limited to alloy compositions lattice-matched to the available substrate materials, such as InP, InAs, and GaSb.

The main materials that have been researched in the past few decades have been InGaAsSb and GaSb on a GaSb substrate and InGaAs and InAsP on an InP substrate. Binary **GaSb** is the most frequently used TPV material, with a bandgap value of 0.72 eV at 300K. GaSb was originally developed for multi-junction solar cells [23]. This material has a direct bandgap and therefore a relatively high efficiency. GaSb is the only diode material to be incorporated into a commercial TPV application thus far [24]. **InGaAsSb**, also referred to as GaInAsSb, is another antimonide that has been researched over the years. Grown lattice matched to GaSb, it has a bandgap ~0.5eV. By varying the alloy composition, InGaAsSb can have a bandgap as low as 0.26 eV with a high quantum efficiency out to 4.8 μm. However, when this material was tested experimentally, the open-circuit voltage of only 3 mV [25].

InGaAs can be grown lattice matched to InP with E_g=0.74 eV, or mismatched in the range of ~0.5-0.6 eV. The lowest bandgap achieved thus far for InGaAs TPVs has been 0.52 eV [26]. **InGaAsP**/InP has also been researched as a TPV diode material. A major advantage of using this quaternary alloy over the ternary InGaAs is that the quaternary alloy has two degrees of freedom and, therefore, a wider range of bandgap values can be obtained while maintaining lattice matching to the substrate. The addition of phosphorous allows for extension to longer wavelengths, with more narrow bandgap diodes in the range of 0.3-0.55 eV. As with most narrow bandgap diodes, as will be discussed in Chapter 3, however, increased auger recombination becomes a major issue. Another phosphorous alloy, **InAsSbP**, has been grown lattice matched to InAs [27–29], and has a similar bandgap range to that of InGaAsP/InP. Lastly, **InAs** has also been recently investigated for TPVs. This is the lowest bandgap bulk material investigated for TPVs thus far; with a bandgap of 0.32eV, InAs covers wavelengths out to 3.9 μm [30].

A sampling of the performance of various TPV diode materials is tabulated in **Table 2-1**. From this table we note that the present technology covers a range from 0.74 eV down to ~0.3 eV. A direct comparison between the various materials is not fair, given that they are tested using a variety of light sources, and the short-circuit current scales with light intensity. Therefore, a perhaps better method of comparison is the quantum efficiency, which shows how well each diode absorbs at a given wavelength, irrespective of the light source. The quantum efficiency of several common diode materials is plotted in **Figure 2-19** [31]. The data shows that GaSb and InGaAsSb have demonstrated the best quantum efficiency thus far.

Material	E_G (eV)	λ_C (μm)	J_{SC} (A/cm^2)	V_{OC} (V)	FF	V_F	REF
$InGa_{0.53}As_{0.47}$	0.74	1.7	1	0.47	0.64	0.63	[32]
GaSb	0.72	1.7	3	0.41	-	0.57	[33]
$InGa_{0.69}As_{0.31}$	0.60	2.1	2.26	0.36	0.67	0.59	[34]
InGaSb	0.56	2.2	3	0.27	-	0.48	[35]
InGaAsSb	0.53	2.4	1	0.30	-	0.57	[36]
InAsSbP	0.35	3.5	3	0.12	-	0.34	[37]
GaInAsPSb	0.34	3.6	0.29	0.03	0.33	0.08	[38]
InAs	0.32	3.9	0.89	0.06	0.37	0.19	[30]

Table 2-1: Table of TPV diode performance for various materials. The bandgap (E_G), cutoff wavelength (λ_C), short circuit current (J_{SC}), open-circuit voltage (V_{OC}), fill factor (FF), and voltage factor (V_F) are tabulated

.

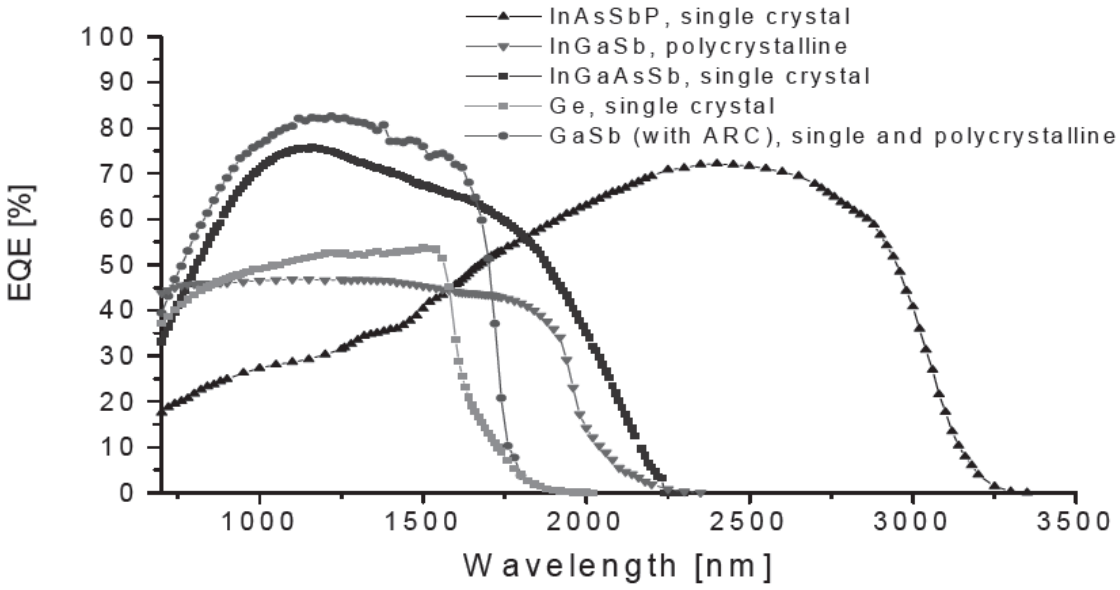

Figure 2-19: Plot of the external quantum efficiency (EQE) of various TPV diode materials [39].

2.3 Photonic Crystals

A photonic crystal (PhC) is a structure consisting of materials of varying dielectric value with some periodicity, **Figure 2-20**. These structures are of interest because they can be used to manipulate the flow of light. PhCs are used in this work, for example, to alter the absorption profile in TPV diodes. To provide context for this work, background on PhCs is presented in this section. First a review of electromagnetic waves and the polarization terminology for light incident on a PhC surface is provided. Then the main operating principles of PhCs are described as well as the applications of PhCs to optoelectronic devices. For further details on PhCs, the reader is directed to the book "Photonic Crystals, Molding the Flow of Light" by John Joannopoulos [40].

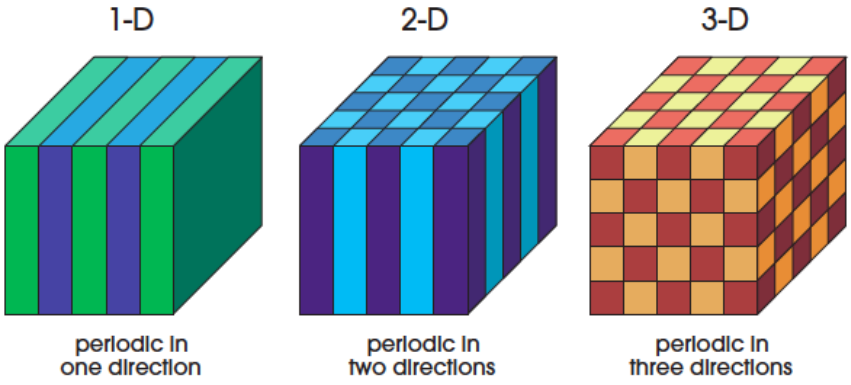

Figure 2-20: Example of one, two, and three dimensional photonic crystal structures. The colors represent materials with different dielectric values [40].

2.3.1 Electromagnetic radiation and polarization

Light is made up coupled, oscillating electric and magnetic fields, **Figure 2-21**. The propagation of light through a medium is described by the relationship between these fields by Maxwell's equations, **2-43** and **2-44**. Here E is the electric field, H is the magnetic field, ε is the permittivity, μ is the permeability, M_{source} is the equivalent

magnetic current density, J_{source} is the electric current density, σ is the electric conductivity, and σ^* is the equivalent magnetic loss.

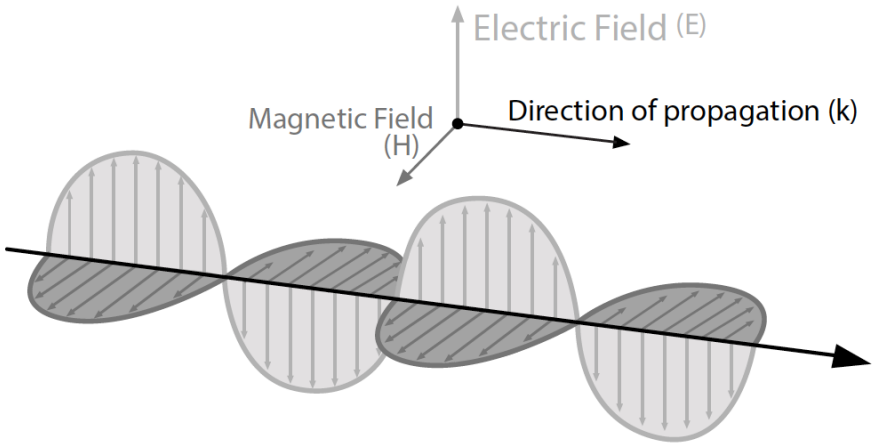

Figure 2-21: The electric and magnetic field components of light. The electric field and magnetic field are orthogonal to each other and the direction of propagation.

$$\frac{\partial H}{\partial t} = \frac{-1}{\mu}\nabla \times E - \frac{1}{\mu}(M_{source} + \sigma^* H) \quad \text{2-43}$$

$$\frac{\partial E}{\partial t} = \frac{-1}{\varepsilon}\nabla \times E - \frac{1}{\varepsilon}(J_{source} + \sigma E) \quad \text{2-44}$$

Depending on the orientation of the electric and magnetic field components of light relative to the surface the light is incident on, the light can be classified as transverse electric (TE) or transverse magnetic (TM). For 2D photonic crystals, the polarizations are defined as follows: *transverse electric* is when the electric field is confined within the plane of the PhC pattern (E_x, E_y, H_z), and *transverse magnetic* is when the magnetic field is confined within the plane of the PhC pattern (H_x, H_y, E_z), **Figure 2-22**. Notice in

Figure 2-22 that the direction of propagation (k) for the two cases is the same, but the fields are oscillating in different planes. In the left figure, the electric field is contained within the plane and the magnetic field is oscillating perpendicular to the plane. In the right figure, the magnetic field is contained within the plane and the electric field is oscillating perpendicular to the plane.

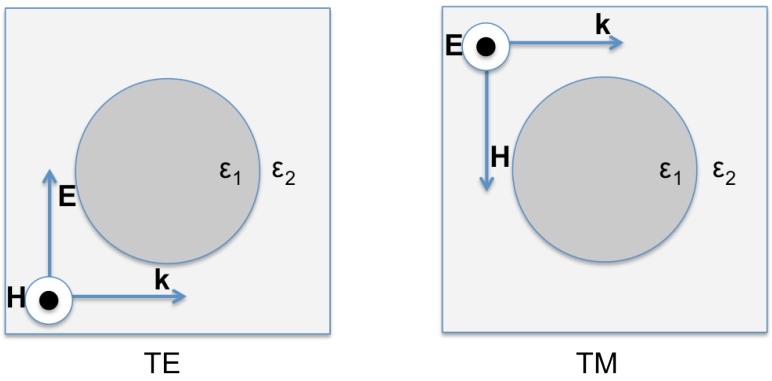

Figure 2-22: Transverse electric (TE) and magnetic (TM) polarizations with respect to a 2D PhC pattern. Here one unit cell is shown for a rod pattern consisting of two different dielectric materials. Notice that the direction of propagation (k) for the two vectors is the same, but the fields are oscillating in different planes.

2.3.2 Fundamentals of photonic crystals

For a bulk material of constant dielectric value, light of any wavelength may propagate within the material unperturbed. However, if the dielectric constant is varied with a periodicity, as is the case with PhCs, light within the material may interfere destructively causing some wavelengths of light to not pass through. When a range of wavelengths is not permitted, a *photonic bandgap* is said to exist. The photonic bandgap is analogous to the electronic bandgap discussed in Section 2.1; Just as we used plots of E(k) to understand the electronic properties of a material from a periodic variation of potential, we can use a plot of ω(k) to analyze the optical properties of a material due to a periodic variation of dielectric, where ω is the angular frequency and k

is the wave vector. Examples of photonic bandstructure plots for a bulk material and a 1D photonic crystal are shown in Figure 2-23. For bulk GaAs, which has a constant dielectric value, there is no photonic bandgap, Figure 2-23 (left). When GaAs is alternated with AlGaAs in a multilayer structure, however, a narrow bandgap forms due to the small dielectric difference of the two materials, Figure 2-23 (center). For a GaAs/air multilayer the dielectric difference is much greater and the bandgap widens Figure 2-23 (right).

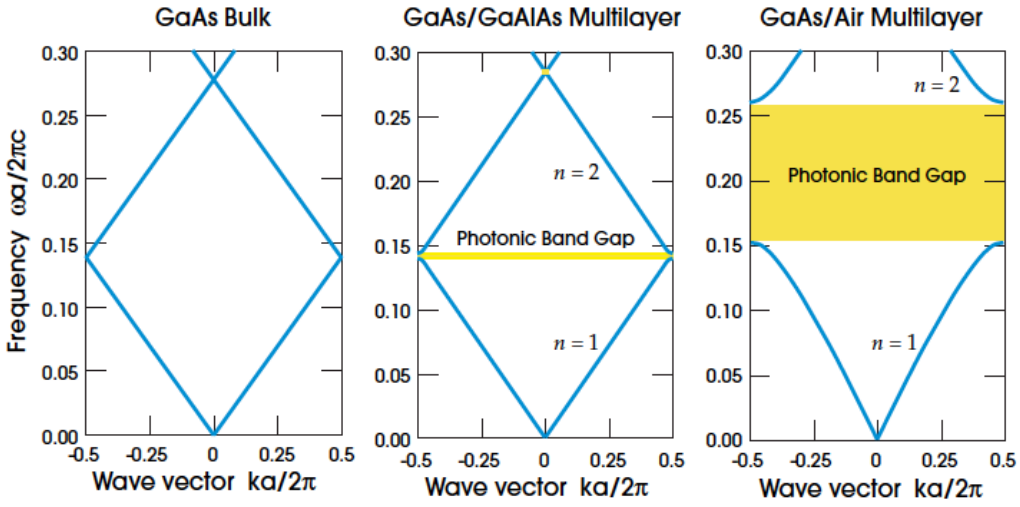

Figure 2-23: Example of photonic band structures for bulk and 1D PhCs. (left) bulk GaAs does not have a photonic bandgap due to the constant dielectric of ε=12. (middle) GaAs/GaAlAs multilayer where the dielectric varies between ε=12 and ε=13, creating a small bandgap (right) GaAs/air multilayer where the dielectric varies between ε=12 and ε=1; the bandgap is wider in this case because of the large difference in permittivity of the two materials [40].

The example above was for a 1D photonic crystal, where the dielectric varied as we moved in the z-direction. In this dissertation, we employ 2D PhC structures, where the dielectric value varies in two dimensions. A photonic bandgap will then occur only if all combinations of k=kx,ky are not permitted. Rather than plotting all possible

combinations of the k vector, we can calculate the photonic bandstructure along the points of high symmetry for the PhC pattern. Since a photonic crystal pattern repeats by the unit cell, we can form a Brillouin zone analogous to the case for the crystal lattice in Section 2.1. We can then illustrate the various modes for different locations in k-space, (which correspond to different positions in physical space. As an example, below we show the irreducible Brillouin zone for a pattern of a triangular lattice of rods. In **Figure 2-24** we show how the triangular lattice in physical space (left) maps to the reciprocal lattice in k-space (center). From this lattice we can form the Brillouin zone which is the yellow hexagon in **Figure 2-24**, right. The points of symmetry are labeled as Γ, M, and K. We can then plot the bandstructure as we move between points of high symmetry, **Figure 2-25**. In this plot of the bandstructure we see that the triangular lattice pattern allows for a complete bandgap for both TM and TE polarizations.

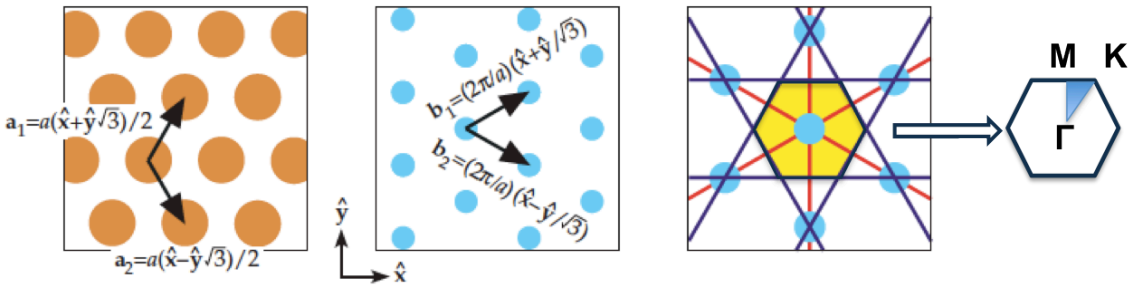

Figure 2-24: (Left) photonic crystal pattern for triangular lattice of rods in real space. (Center) reciprocal lattice in k-space. (Right) Brillouin zone construction for reciprocal lattice. We see that the first Brillouin zone is defined by a hexagon. The high symmetry points are Γ, M, and K. Figure adapted from reference [40].

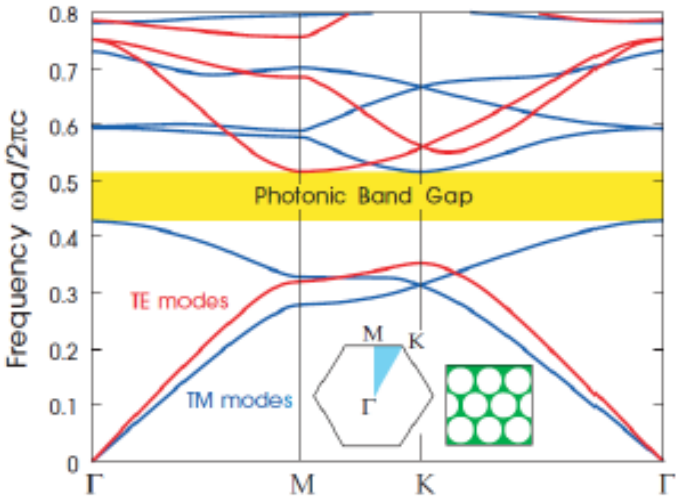

Figure 2-25: Photonic bandstructure for 2D PhC pattern of rods in a triangular lattice. The modes are plotted between the points of high symmetry. This pattern allows for a complete photonic bandgap for both TE and TM polarized light [40].

2.3.3 PhC Device Applications

Since PhCs can be used to manipulate light, they have wide-ranging applications in optoelectronic devices [41–45]. As photonic crystals prevent the transmission of certain wavelengths of light, PhCs can be used, for example, as a cladding layer for a waveguide to trap light within the waveguide, **Figure 2-26**. In addition to fiber optics, PhCs can also be used in photodetector technologies [43–45]. 2D metallic PhCs can be deposited onto the front surface of a photodetector aperture, **Figure 2-27**. These structures, also referred to as photonic resonant cavities, have a finite height and therefore do not yield the same result as a perfect 2D photonic crystal that continues infinitely in the +/- z direction. One could think of the truncated 2D PhC as a PhC pattern with defects, where the defects create allowed modes within the bandgap, improving absorption at certain wavelengths. This improvement in absorption has been demonstrated in infrared photodetectors, whereby the addition of the PhCs on the

detector aperture increased both the photocurrent and the conversion efficiency of the detector device [43].

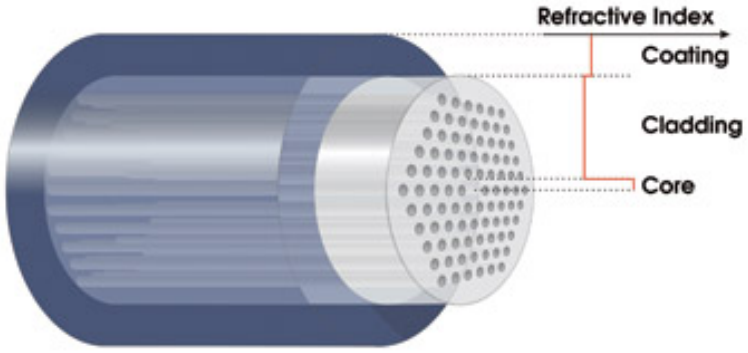

Figure 2-26: 2D photonic crystals fiber optical cable. The PhCs act as a cladding layer to trap the light in the core of the cable [46]

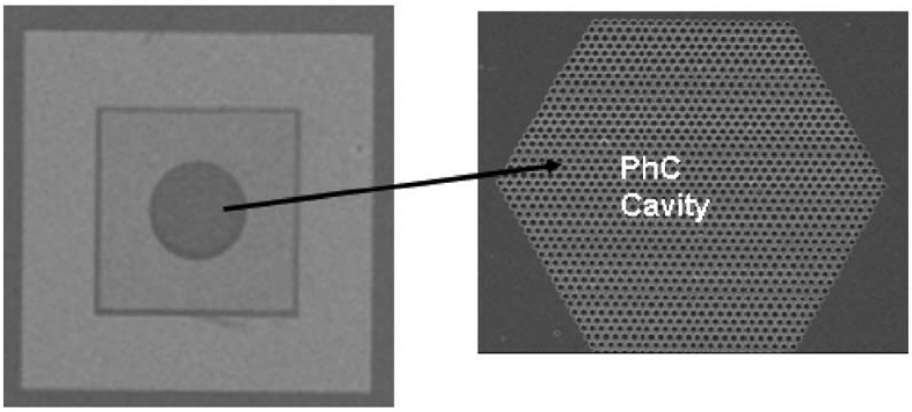

Figure 2-27: Example of 2D metallic photonic crystals used in infrared photodetector. The addition of the metallic photonic crystals increase the photocurrent and conversion efficiency in the device [43].

Owing to the improvement in conversion efficiency demonstrated for infrared photodetectors, metallic photonic crystals have been proposed for use in TPV devices [24][25]. Initial work demonstrated an improvement in the absorption of GaSb through

the incorporation of front-surface 2D metallic PhCs, **Figure 2-28**, which lead to an increase in short-circuit current for GaSb TPV diodes [48], [49]. This project is under continued development and the design of the GaSb diode structure is the subject of Chapter 7.

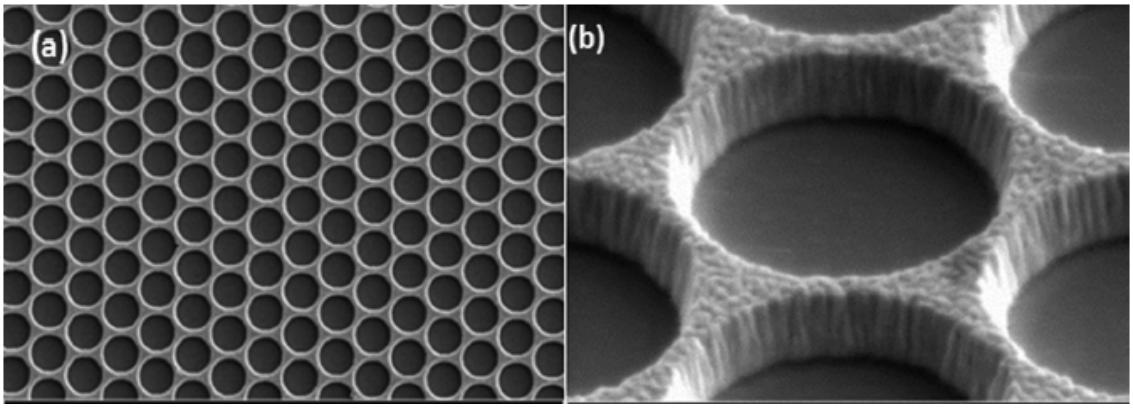

Figure 2-28: 2D metallic photonic crystal pattern deposited on the aperture of a TPV diode for improved absorption. (a) SEM of top view of PhC pattern (b) SEM image taken at 45 degrees to normal incidence [50].

3 This Work-

The work in this dissertation includes both designing new TPV diode technologies capable of converting radiation from untapped, lower temperature heat sources and working to improve upon the current state-of-the-art GaSb TPV diode. These projects are motivated in Sections 3.1 and 3.2 respectively.

3.1 Extending the Operational Wavelength of TPV Devices

TPV diodes typically have bandgaps in the energy range of 0.5–0.74 eV, which corresponds to emitter temperatures >2000°C [51][52]. Smaller bandgap thermophotovoltaic diodes are of interest because they can absorb longer wavelength radiation from lower temperature sources, extending the range of applications for TPV.

In this section, we first discuss the advantages of using smaller bandgap diodes. We show that shorter bandgap diodes (≤ 0.25eV) allow for a higher efficiency for lower temperature sources (1000°C and less). We also show that these shorter bandgap diodes can generate a higher power density.

Despite being better matched to lower temperature sources, narrow bandgap diodes have yet to be employed successfully. One main challenge is the reduced open-circuit voltage due to the large parasitic dark current in these devices. In this work, we propose using a superlattice barrier structure to both reduce the dark current and improve the open-circuit voltage. The study and results are then detailed in Chapter 7.

3.1.1 Advantages for Narrow Bandgap TPV Diodes

3.1.1.1 Improved Spectral Matching

The spectral radiance from a blackbody at temperature T can is described by Planck's Law, Equation **3-1**, where k_B is Boltzmann constant, *h* is the Planck constant, and *c* is the speed of light within the material. The peak wavelength of this spectrum is calculated by Wien's Displacement Law (Equation 3-2) where *b* is Wien's displacement constant.

$$B_\lambda(T) = \frac{2hc^2}{\lambda^5}\frac{1}{e^{hc/(\lambda k_B T)} - 1} \quad \text{3-1}$$

$$\lambda_{max} = b/T \quad \text{3-2}$$

One might assume that the bandgap of a photodiode should be matched to the energy value corresponding to the peak wavelength of a given spectrum. However, at this value, only 25% of the incident spectrum can be converted [53]. The optimal bandgap for maximum conversion efficiency was derived by Shockley and Queisser [51], and later extended to thermophotovoltaics by Cody [54]. The efficiency can be written in terms of the dimensionless bandgap parameter, u_g, which is the ratio of the bandgap energy E_G to the thermal energy kT of the emitter, Equations **3-3** and **3-4**. Shockley and Queisser showed that the conversion efficiency is optimized when u_g =2.17. Using this value, we can rewrite Equation **3-4** to solve for the bandgap that will yield a maximum efficiency for a given emitter temperature T_E, Equation **3-5** [53]. From this equation we observe that materials with a bandgap of 0.5 eV are only optimal for very high, >2000°C, emitter temperatures.

$$\eta_{max} = \frac{15}{\pi^4} u_g \int_{u_g}^{\infty} \frac{u^2}{e^u - 1} du \quad \text{3-3}$$

$$u_g = \frac{E_G}{kT_E} \quad \text{3-4}$$

$$E_{gOPTIMAL} = 1.87\times10^{-4}\, T_E \quad \text{3-5}$$

To convert the incident radiation from a lower temperature source of 1,000°C, the bandgap of the TPV diode should be closer to 0.24eV, which corresponds to a cut-off wavelength ~ 5μm. From Equation **3-3**, we calculate by the SQ limit that for a 1,000°C source, a single-junction 0.24eV diode will have an ultimate efficiency of 44%, whereas a single junction 0.5eV diode would have an ultimate efficiency of only 24%.

Emitter Temperature (°C)	$E_{gOPTIMAL}$ (eV)	Cut-off wavelength (μm)
2400	0.500	2.5
1000	0.238	5.2
500	0.145	8.6

Table 3-1: Bandgap and cutoff wavelength for optimal conversion efficiency for various emitter temperatures.

3.1.1.2 Higher Power Density

For an ideal TPV system with a perfect blackbody emitter and a zero-reflectance diode, the maximum power density of the system is calculated by Equation **3-6** [53]. The equation is a function of the temperature of the emitter and the dimensionless bandgap energy, *u*. Power density is a monotonically increasing function of emitter temperature and is determined by above-bandgap photons only. A smaller bandgap increases the

integration range, allowing more photons to be absorbed and converted to usable power. This can be seen in Figure 3-1 below, where the maximum power density is plotted versus source temperature for several bandgap values. For an emitter temperature of 1,000°C, a cell with E_g=1.1eV results in a power density of only 0.1 W/cm^2, whereas a cell with E_g=0.25eV has a power density of 6.5 W/cm^2.

$$\frac{P_{max}}{Area} = \frac{15}{\pi^4}\sigma_{sb}T^4 u_g \int_{u_g}^{\infty} \frac{u^2}{e^u - 1} du \qquad 3\text{-}6$$

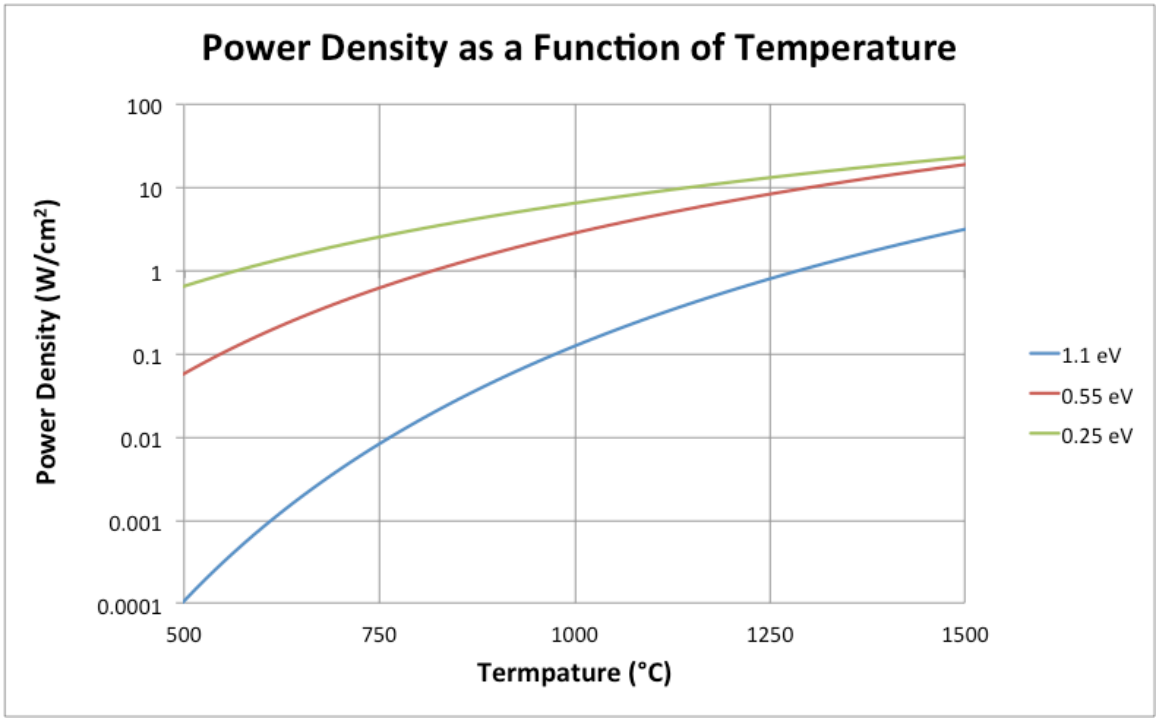

Figure 3-1: Plot of the power density as a function of temperature for various bandgaps. The power density increases for decreasing bandgap. For example, at 1,000°C, the 0.25eV diode has a power density >10x than the diode with a bandgap of 1.1eV.

3.1.2 Challenges for Narrow Bandgap TPV Diodes

As demonstrated in the previous section, a smaller bandgap diode can both more efficiently convert radiation from a lower temperature source and, for a give emitter temperature, allow for a higher power density. What then are the issues preventing these structures from realization?

A major obstacle for low bandgap diodes is the reduced open-circuit voltage. This can be seen in **Table 3-2**, where the open-circuit voltage quickly goes to zero for decreasing bandgaps. One way to look at this is the voltage factor V_F, which is given by the ratio of the open-circuit voltage to the bandgap. This metric provides a measure of how well a device exploits the potential barrier of the PN junction, as discussed in Section 2.1.7. From the radiative limit, Equation **3-7**, an upper bound for the voltage factor can be calculated [39][55]. The limit is plotted as the dotted line in **Figure 3-2** [56]. Here we see that that the voltage factor is expected to decrease slightly with decreasing bandgap. However, we also note, in comparing the theoretical limit to the experimental data points, that for narrow bandgap diodes, actual devices are far from their theoretical limit. This may be due to (1) increased recombination that arises in smaller bandgap devices, especially due to Auger or (2) the fact that the lower bandgap materials are a younger technology and have yet to be fully developed [56]. In the following section, we detail several approaches for decreasing dark current and improving open-circuit voltage in narrow bandgap TPV diodes, including using superlattice and barrier structures.

Material	E_G (eV)	V_{OC} (V)	REF
$InGa_{0.53}As_{0.47}$	0.74	0.47	[32]
GaSb	0.72	0.41	[33]
$InGa_{0.69}As_{0.31}$	0.60	0.36	[34]
InGaSb	0.56	0.27	[35]
InGaAsSb	0.53	0.30	[36]
InAsSbP	0.35	0.12	[37]
GaInAsPSb	0.34	0.03	[38]
InAs	0.32	0.06	[30]

Table 3-2: Table of the bandgap (E_G) and open-circuit voltage (V_{OC}) for various TPV diode materials.

$$V_F = 1 - \frac{T_C}{T_E} + \frac{kT_C}{E_G} ln \frac{T_E}{T_C} \qquad 3\text{-}7$$

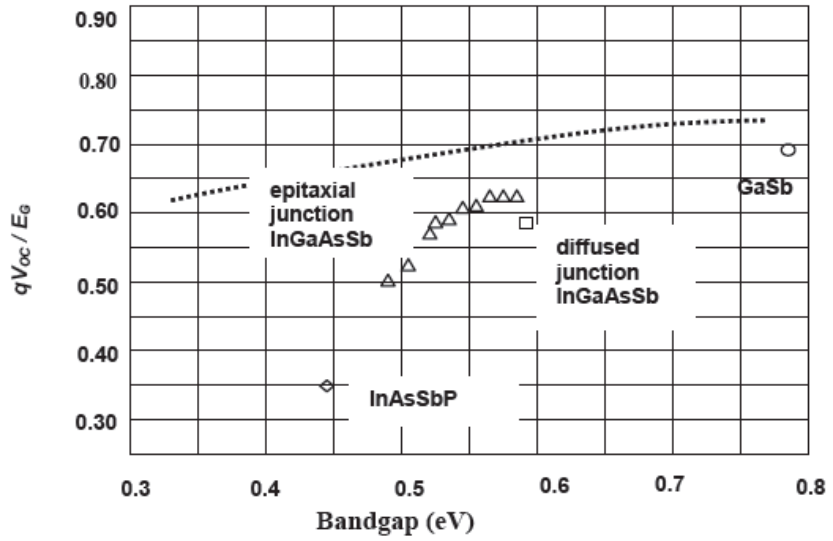

Figure 3-2: Comparison of the experimental voltage factor to the radiative-limit voltage factor for TPV diodes with a range of bandgaps. Plot from reference [56].

3.1.3 Reducing J_{dark} and improving V_{OC} for narrow bandgap TPVs

3.1.3.1 Incorporating a Barrier

One avenue to improve the open-circuit voltage in narrow bandgap diodes is through the incorporation of a wide bandgap layer within the device structure. For example, Turner et al. [57] investigated a heterostructure for TPV diodes, in which a wider bandgap p–type GaInAsSb emitter layer was paired with a 0.54eV n-AlGaAsSb absorber base. The addition of the wide bandgap layer increased the open-circuit voltage, leading to the highest V_{OC} reported thus far for TPV diodes of this bandgap.

A wide bandgap layer could also be inserted *within* the PN junction in what is known as a “unipolar barrier diode” or “bariode” device [58–61], **Figure 3-3**. These structures have been studied extensively in the last decade for MWIR and LWIR photodetectors. They were first mainly investigated in nBn photodetector devices [62],

[63] and later extended to XBn, where X could be a p-type or n-type region [64–67]. These barrier photodetector devices are of interest because they have demonstrated reduced dark currents [68] [69]. The reduction in dark current is attributed to the wider bandgap material, which effectively eliminates the generation-recombination current in the depletion region. Since these infrared detectors are operated at liquid nitrogen temperatures (77K) where the generation-recombination is the largest contributor to dark current (Section 2.1.5), the overall dark current is reduced.

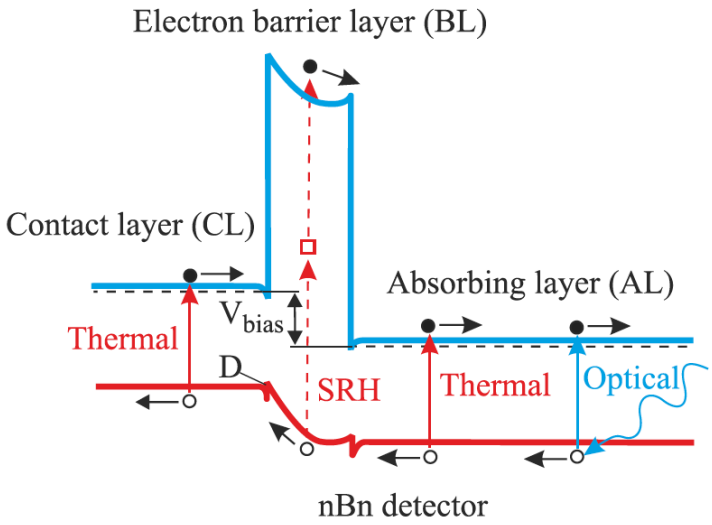

Figure 3-3: Example of a barrier diode or "bariode" structure. This is an nBn structure used in photodetector applications [58].

TPVs, however, operate at room temperature, where the *diffusion* current is the dominant dark current mechanism. This means that a reduction in the GR current will have a negligible effect on the diode performance – it is the diffusion current that must be reduced. Here we propose that a barrier structure may also decrease the diffusion current. Recall from Section 2.1 that under forward bias, majority carriers overcome the potential barrier of a PN junction to diffuse to the other side of the junction, where they become minority carriers. These carriers make up the diffusion current. At zero bias a

diode is at equilibrium and the dark current mechanisms balance such that there is no net current. As we begin to apply a forward bias to the diode, the potential of the PN junction is lowered and some carriers have enough energy to overcome the barrier. In a conventional PN diode, the majority carriers can move to the other side of the junction, where they become minority carriers and recombine, forming a concentration profile from which the diffusion current may be calculated. For a barrier diode, we effectively have a larger built-in potential. Carriers therefore need more energy for the same applied bias to overcome the junction, and the diffusion current will be reduced. We then see that the diffusion current with a barrier structure could be less than that for a conventional PN diode. This decrease in diffusion current in the forward bias region could therefore potentially shift the elbow of the IV curve, as shown in **Figure 3-4**, which would lead to a higher open-circuit voltage.

A schematic of the proposed barrier structure is shown in **Figure 3-5**. With this configuration, the barrier may block holes that would normally contribute to the dark current, but would not block photogenerated carriers. This structure is investigated in Chapter 6.

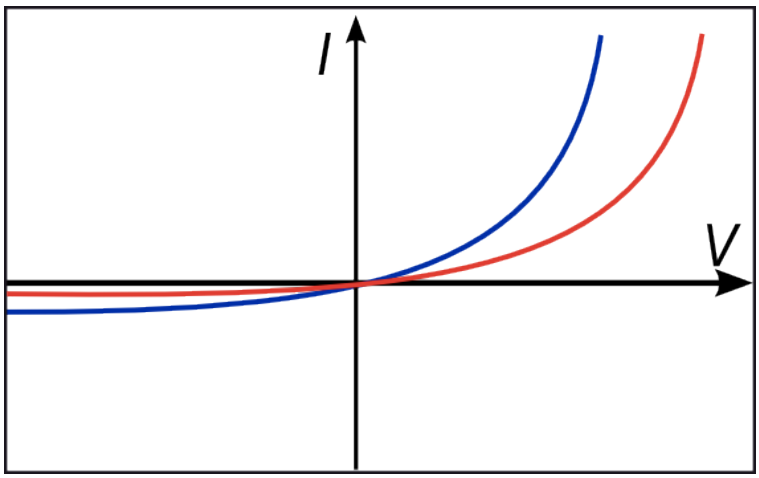

Figure 3-4: Plot comparing dark current for two different diodes. The diode with the lower saturation current is shown in red. The decreased saturation current leads to a higher turn on voltage, which will translate to a larger open-circuit voltage when the diode is illuminated.

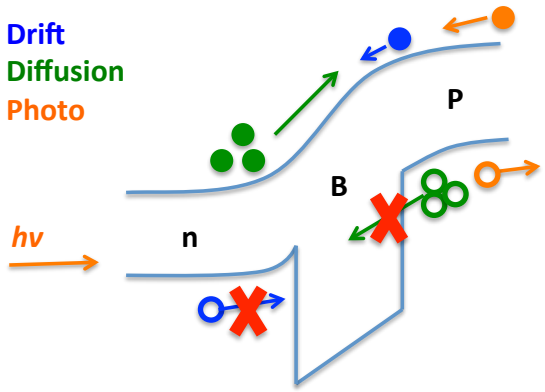

Figure 3-5: Barrier diode band structure: For a monovalent barrier, minority carrier and majority carrier holes are blocked which would normally contribute to the dark current. Photogenerated carriers absorbed in the p-type absorber (shown in orange) are not blocked.

3.1.3.2 Superlattice Structure

Engineering the barrier structure discussed above is non-trivial; it requires finding a wide bandgap material that has the same conduction band level as the desired absorber, a large offset in the valence band, and minimal lattice mismatch. This can be challenging if we limit ourselves to bulk materials with fixed bands. Instead, we employ superlattice structures, which allow us to engineer the bands in a precise manner.

A superlattice is a structure composed of alternating periodic thin (on the order of a few nm) layers of material. Unlike multiple quantum wells, which are spaced far enough apart to be considered isolated, in superlattice structures the wells are close enough such that the wave functions overlap and intermix, leading to the formation of minibands, **Figure 3-6**. The bandgap is then given by the transition from the highest hole miniband band to the lowest electron miniband. The bandgap can be tailored by changing the well thickness and height by varying the thickness and material of the constituent layers.

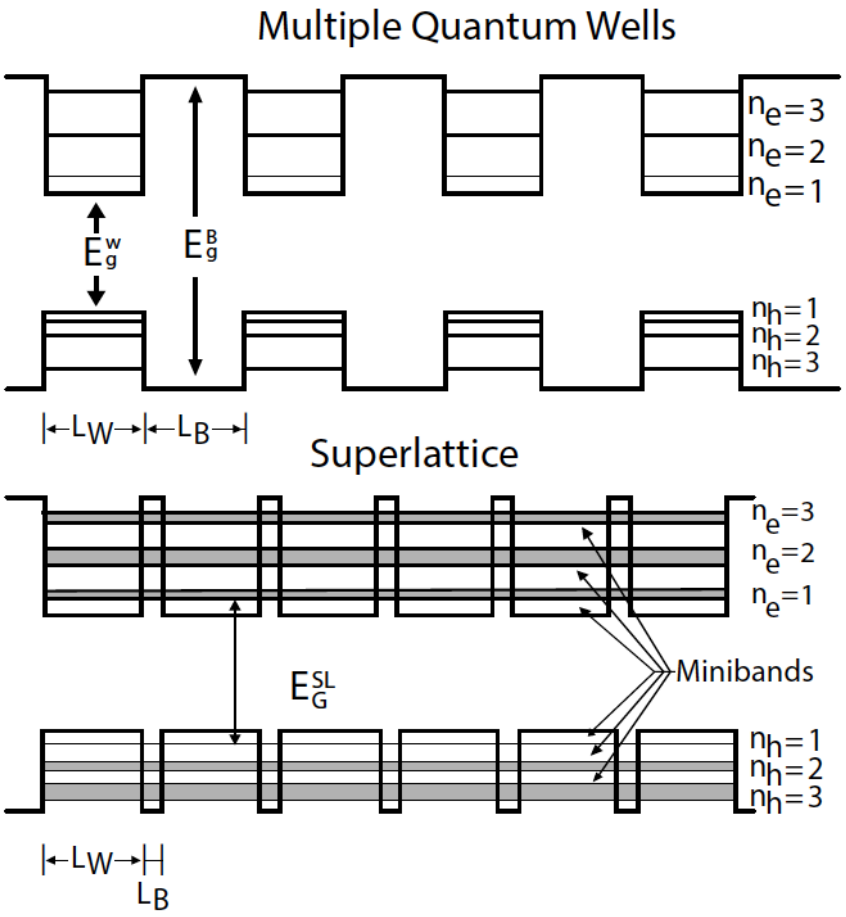

Figure 3-6: Comparison of multiple quantum wells versus superlattice structures. In a multiple quantum well structure, the quantum wells are spaced far enough apart to be isolated from each other. The bandgap in each material is determined by the transition between the conduction and valence band in each material. In a superlattice structure, the wells are close enough together such that the wave functions become coupled. This leads to the formation of minibands. The bandgap of the superlattice material is then given by the transition between the highest hole miniband and the lower electron miniband. The bandgap can be tuned by varying the thickness of the well (L_W) and barrier (L_B) layers.

Depending on the relative alignment of the conduction and valence bands of the two materials, the superlattice can be classified as a type-I or type-II superlattice. Let the superlattice be made of alternating materials A and B. In a type-I superlattice (T1SL), material A has a lower conduction band and a higher valence band than material B, creating a series of wells that confine both electron and holes within material A, **Figure 3-7**. In a type-II superlattice (T2SL), both the conduction band and valence band of material A are lower than that of material B – confining electrons and holes to separate materials. T2SL are further classified based on the relative alignment of the conduction band of material A to the valence band of material B. If the conduction band of material A is higher than the valence band of material B, than the material is “type-IIA” or staggered. If the conduction band of material A is lower than the valence band of material B, than the material is “type-IIB” or “broken-gap”. The broken-gap structure is of particular interest because it uniquely allows for a bandgap that is smaller than the bandgap of either constituent material. For example, in this work we use the InAs/GaSb superlattice material system, which can have bandgaps in theory ranging from 0.41 down to 0.04 eV [70].

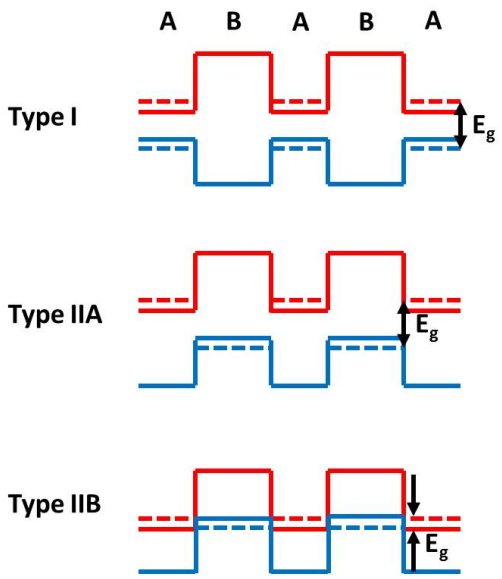

Figure 3-7: The conduction band (red) and valance band (blue) are represented by solid lines and electron and hole minibands are represented by dashed lines. The various possible band alignments are illustrated. In a T1SL, material A has a lower conduction band and higher valence band than material B. For T2SL, both the conduction band and valence band of A are lower than that of B – confining electrons and holes to separate materials. A T2SL is further classified based on the relative alignment of the conduction band of material A and the valence band of material B. If the conduction band of A is higher than the valence band of B, than the material is type-IIA. If the conduction band of A is lower than the valence band of B, then the material is classified as type-IIB.

In addition to bandgap flexibility, incorporating a superlattice for longer wavelength TPV diodes has several other advantages, including suppressed Auger recombination and a de-coupled effective mass.

Reduced Auger Recombination:

Auger recombination, as discussed in Section 2.1, is a multi-particle process. For example, an electron may recombine with a hole, transferring the energy to another hole to send it deeper into the valence band. Strain in a T2SL structure will induce a

large splitting between heavy-hole and light-hole sub-bands, pushing the lighter hole band further from the conduction band. If the separation between these hole bands is larger than the bandgap, conservation of energy and momentum causes it to be more difficult for Auger recombination to occur. Infrared photodetector research shows that separation of these hole bands indeed suppresses Auger recombination, enhancing carrier lifetimes [71] [72].

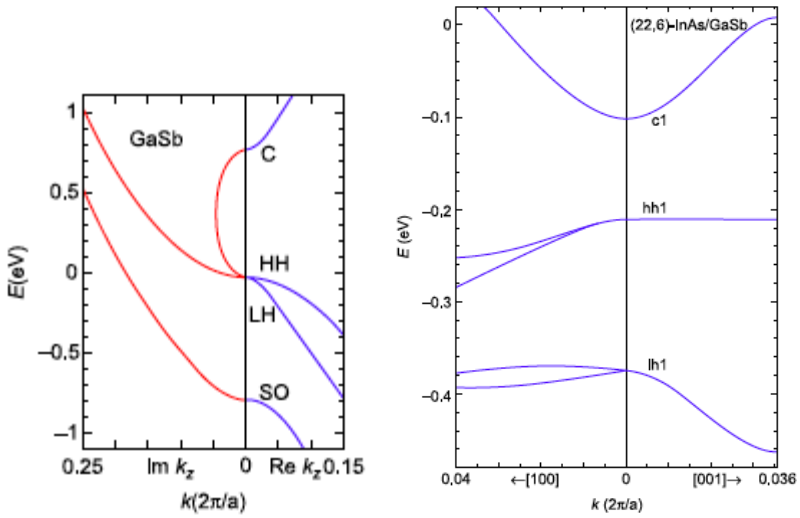

Figure 3-8: Comparison of band structure for a bulk material (left) versus a superlattice material (right). In the superlattice material, the heavy and light hole bands split, making it more difficult for Auger recombination to occur [73].

Reduced Tunneling:

In bulk materials the carrier effective mass is coupled to the bandgap. More precisely, the effective mass is related to the bandgap by Equation **3-8**, in which P is the interband squared matrix element, E_G is the bandgap, and Δ is the spin-orbit interaction energy. For $E_G >> \Delta$, and $1/m^* >> 1$, Equation **3-8** can be approximated as Equation **3-9**, and we observe that the effective mass is directly proportional to E_G. **Figure 3-9** shows the effective mass as a function of bandgap for various bulk materials. From this figure

we see that a bulk semiconductor material with a narrow bandgap will have a small effective mass.

$$\frac{1}{m^*} = 1 + \frac{P^2}{3}\left(\frac{2}{E_G} + \frac{1}{E_G + \Delta}\right) \quad 3\text{-}8$$

$$\frac{1}{m^*} \sim \frac{P^2}{E_G} \quad 3\text{-}9$$

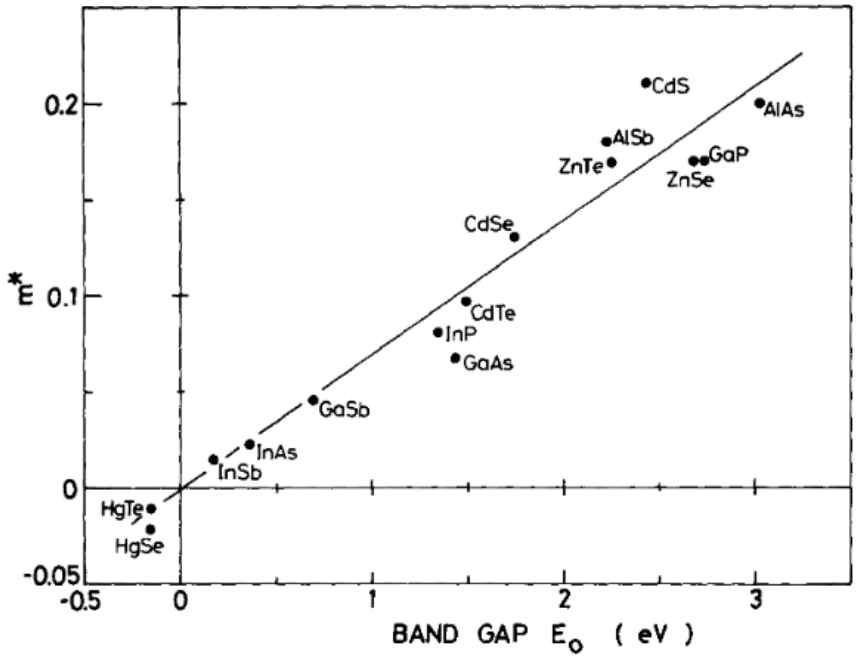

Figure 3-9: Plot of the effective mass versus bandgap of various bulk materials. We observe that the effective mass is directly proportional to the bandgap. From ref. [74].

For T2SLs, however, the effective mass is decoupled from the bandgap and does not follow this relation [73]. This can be seen, for example, in a plot of the effective mass for varying ratios of superlattice composition, **Figure 3-10**. Notice the wide range of possible values. T2SL, therefore, can be designed to have a larger effective mass for a given bandgap as compared to bulk materials. This leads to an improvement in

absorption, since absorption is proportional to the joint density of states. This may also decrease unwanted parasitic tunneling currents. A heavier effective mass is a tradeoff, however, because this may also decrease the photogenerated current.

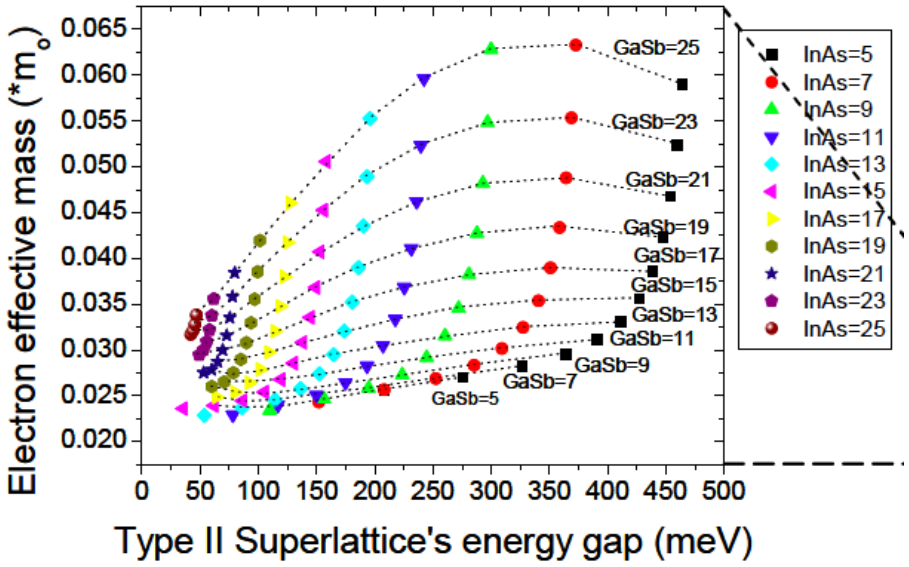

Figure 3-10: Plot of the calculated electron effective mass and bandgap for varying InAs/GaSb superlattice ratios. From reference [75].

The design flexibility of superlattice structures, along with their improved properties such as reduced Auger recombination, make these materials a subject of interest for various diode technologies, including photodetectors and lasers [72] [76] [77]. In this work, we investigate these T2SL materials for TPV barrier devices.

3.2 GaSb Diodes with Front-Surface Photonic Crystals

In addition to extending TPV diodes to longer wavelengths, a portion of this dissertation also seeks to improve upon the existing TPV diode technologies. One method researched in our group to improve the efficiency of GaSb TPV diodes is through the incorporation of front-surface two-dimensional metallic photonic crystals (MPhCs), **Figure 3-11**. MPhCs can be written onto the diode aperture, where they can be used to strategically alter the absorption in the GaSb diode. As discussed in Section 2.3, these repeating nanoscale structures will create a photonic bandgap, allowing certain wavelengths of light to pass through while blocking others. This structure can be used to block out undesirable wavelengths, allowing for transmission of only near-bandgap radiation. In addition to filtering, the MPhCs can also be used to strategically alter the photo-absorption profile within the device structure. The non-infinite height of the MPhC pattern causes the evanescent field to "leak" into the semiconductor material. This allows for improved absorption over traditional all-dielectric anti-reflective coatings.

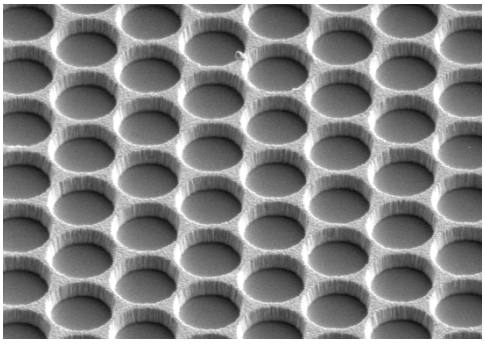

Figure 3-11: SEM image of metallic photonic crystals deposited onto GaSb

MPhCs were first proposed for spectral engineering in GaSb TPV diodes in 2012 [47]. Initial work by REAP Labs demonstrated an increase in the absorption through the incorporation of 2D MPhCs [48], [49], **Figure 3-12**. This improvement in the absorption lead to an increase in the photogenerated current [50]. However, these MPhCs were deposited onto GaSb diodes that were poor-performing, as can be seen by the low measured open-circuit voltage values, which translate to voltage factors of only ~0.2.

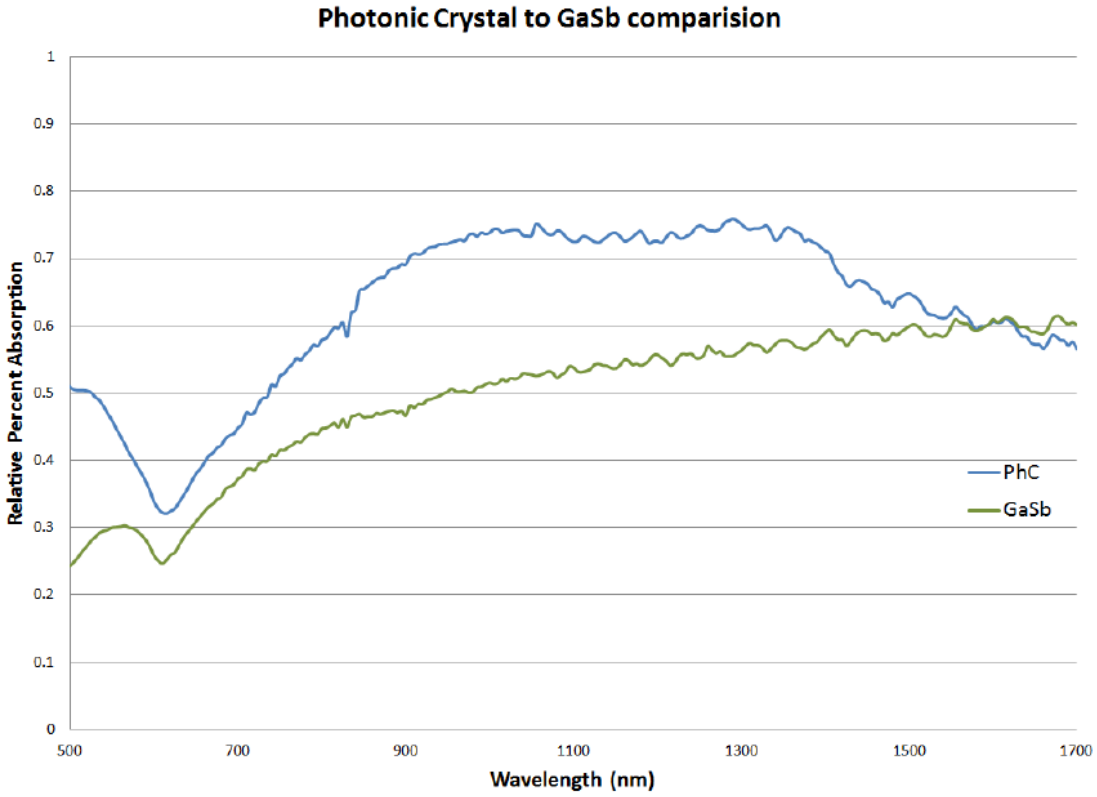

Figure 3-12: Comparison of absorption in GaSb with photonic crystals (blue) and without photonic crystals (green). From reference [49].

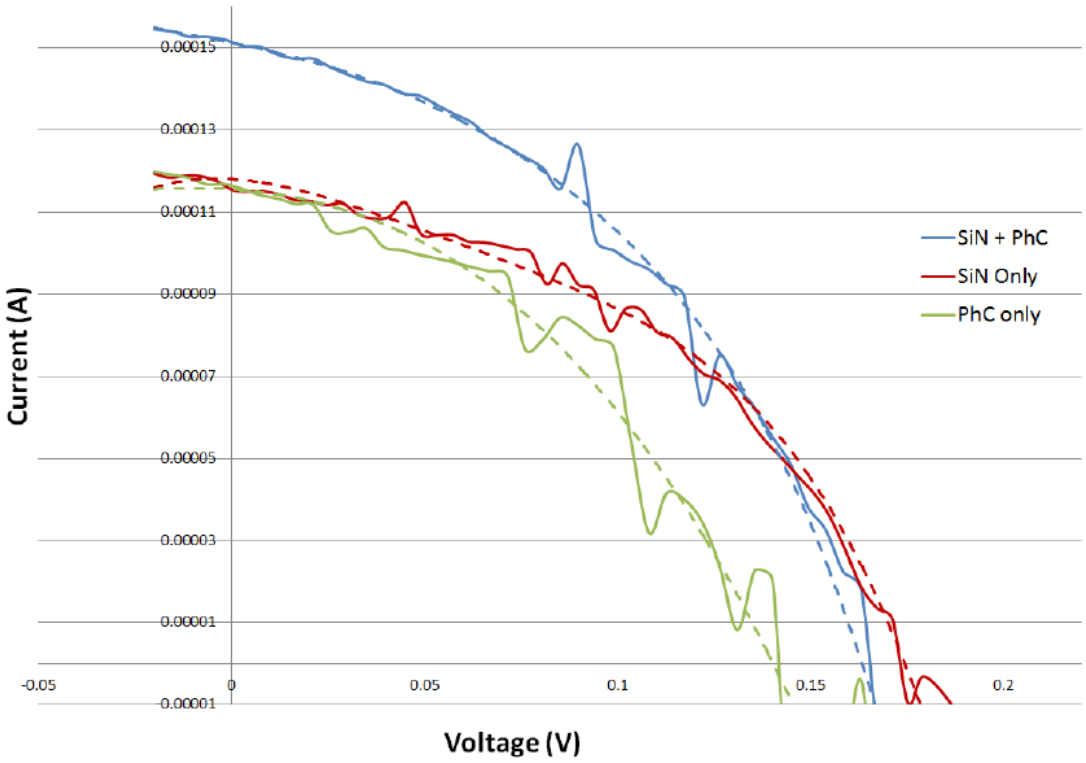

Figure 3-13: Comparison of the light IV curves for GaSb TPV diodes with MPhCs (blue), with only SiN (red), and with MPhCs but no SiN layer (green), from [49].

	V_{OC} (mV)	V_F
SiN - ARC	175	0.241
PhC – No ARC	142	0.196
PhC + ARC	165	0.227

Table 3-3: Open-circuit voltage and voltage factors for GaSb diode with and without PhCs [49]

In this work, we look to improve upon the GaSb/MPhC diode design. We investigate the addition of an intrinsic region to the diode, which would extend the electric field over the shifted photogenerated profile due to the MPhCs. We also

consider routes towards developing ohmic front contacts/MPhCs. This study is detailed in Chapter 7.

4 Device Design Methods

The work in this dissertation entails the design of both superlattice materials and barrier devices. The band structure of superlattice materials is calculated using the 8x8 k·p method with the program NextNano. These simulations allow us to study the way minibands form for varying quantum structures. Materials are designed to create an offset in the valence band between two superlattice materials, while maintaining a smooth transition in the conduction band, thus forming a monovalent barrier structure. The band structure of these materials and their properties can then be input into the TCAD program Silvaco to simulate the performance of a barrier device.

Silvaco is also used to design optimized GaSb diodes. GaSb material parameters from the literature are input into the program and the structure stack is varied to find the optimum design. The following sections detail the simulation methods employed.

4.1 Device Design

The diode structure is designed with the aid of the Atlas-Silvaco software package. Atlas is a physically-based device simulator, which calculates the electrical characteristics of semiconductor devices associated with specified structures and bias conditions. This tool allows us to understand how varying the device architecture may alter the performance of the device.

The device structure is first defined by a 2D grid or mesh. After defining the structure, the materials and their models are specified, as well as bias conditions. The Atlas module *Luminous* is used to simulate light propagation and absorption in the material. After the photogeneration profile in the structure is determined, the Atlas module *Blaze*

can be used to calculate the terminal currents. Differential equations derived from Maxwell's equations are then applied to the grid to simulate carrier transport through the device structure.

4.1.1 Modeling Light

The incident blackbody spectrum is described by Equation **3-1**. The generation rate in the material due to this spectrum is then calculated using ray tracing. The optical intensity and absorption are calculated at each grid point from the ray trace using the real component of the index of refraction (n) and the imaginary component of the index of refraction (k), respectively. The generation rate *G* is given by Equation **4-1**, where η_0 is the internal quantum efficiency, *P* is the ray intensity factor, which contains the effect of reflections, transmissions, and losses in absorption over the ray path, and α is the absorption coefficient which is calculated from Equation **4-2**, with *k* being the imaginary part of the index of refraction. The distance from the ray in question is given by *y*.

$$G = \eta_0 \frac{P\lambda}{hc} \alpha e^{-\alpha y} \qquad 4\text{-}1$$

$$\alpha = \frac{4\pi k}{\lambda} \qquad 4\text{-}2$$

4.1.2 Solving for the current

The coupled equations to be solved consist of Poisson's Equation, the continuity equations, and the transport equations. Poisson's equation relates the electrostatic potential Φ to the space charge density ρ, Equation 4-3. The reference potential in Atlas is defined as the intrinsic Fermi potential. The local space charge density is the sum

from the mobile charges (*n*, *p*), ionized donor and acceptor concentrations (N_D^+, N_A^-) and the charge density due to trap states (Q_T), Equation 4-4. In Atlas the default is full impurity ionization and Q_T=0.

$$div(\varepsilon \nabla \Phi) = -\rho \tag{4-3}$$

$$\rho = q(n - p + N_D^+ + N_A^-) - Q_T \tag{4-4}$$

The continuity equations are given by Equations **4-5** and **4-6**. Here, *J* is the current density, *G* is the generation term, and *R* is the recombination term. The generation and recombination terms are grouped together under the constant *U*.

$$\frac{\partial n}{\partial t} = \frac{1}{q} div\vec{J}_n + G_n - R_n = \frac{1}{q} div\vec{J}_n - U_n \tag{4-5}$$

$$\frac{\partial p}{\partial t} = \frac{1}{q} div\vec{J}_p + G_p - R_p = \frac{1}{q} div\vec{J}_p - U_p \tag{4-6}$$

The current densities can be approximated by the standard drift-diffusion equation Equations **4-7** and **4-8**. These equations show that the current density is the summation of the drift current and the diffusion current. The drift current is due to the electric field *E*, Equation 4-9, and is calculated as the gradient of the potential. The diffusion current is proportional to the gradient of the carrier concentration and the diffusivity *D*, given by Equation 4-10.

$$\vec{J}_n = qn\mu_n \vec{E}_n + qD_n \nabla n \tag{4-7}$$

$$\vec{J}_p = qp\mu_p \vec{E}_p - qD_p \nabla p \tag{4-8}$$

$$\vec{E}_{n,p} = -\nabla\left(\Phi \pm \frac{kT}{q}\ln n_i\right) \quad \text{4-9}$$

$$\vec{D}_{n,p} = \frac{kT}{q}\mu_{n,p} \quad \text{4-10}$$

4.1.3 Models Employed

In this work, we chose to include material models for carrier statistics, mobility, recombination, thermionic emission, and non-local tunneling.

Carrier Statistics

Electrons in equilibrium with the lattice will follow Fermi-Dirac statistics (Section 2.1). The Fermi-Dirac model specifies that the probability f(E) that an available electron state with energy E is occupied is given by Equation **4-11**, where E_F is the Fermi level and k is Boltzmann's constant. If the quantity (E - E_F) is much greater than the thermal energy kT, an approximation can be made known as the Boltzmann approximation. However, for highly doped materials that we may incorporate in our design, this approximation is not valid. As such, we specify the more general Fermi-Dirac model in our simulations.

$$f(\varepsilon) = \frac{1}{1 + \exp\left(\frac{\varepsilon - E_F}{kT}\right)} \quad \text{4-11}$$

Mobility

The default electron and hole mobilities (μ_{n0} and μ_{p0}) are modeled in Atlas by a temperature-dependent, low-field model: Equations 4-12 and 4-13. Here μ_n and μ_p are the room temperature mobilities, T is the temperature of the lattice, and TMUN and TMUP are the low-field mobility parameters. This equation shows that as the lattice temperature increases, the carrier mobility decreases. This decrease in mobility is due to increased scattering from phonons for increasing temperatures.

$$\mu_{n0} = \mu_n \left(\frac{T}{300}\right)^{-TMUN} \quad \text{4-12}$$

$$\mu_{p0} = \mu_p \left(\frac{T}{300}\right)^{-TMUP} \quad \text{4-13}$$

This default model does not account for the change in mobility of a carrier due to the doping of a material. As the doping increases, more scattering occurs, decreasing carrier mobility. Martin and Algora plotted electron and hole mobilities for GaSb samples measured at room temperature for doping levels varying from 10^{16}/cm^3 to 10^{18}/cm^3 [79]. From these values, they proposed a Caughey-Thomas-like model to describe the mobility as a function of doping. In **Table 4-1**, the electron and hole mobilities for various doping levels have been calculated using this fit. These are the values employed in this work.

Doping Level (/cm^3)	Electron Mobility μ_e (cm^2/ V s)	Hole Mobility μ_h (cm^2/ V s)
1×10^{16}	5520	840
5×10^{16}	5000	780
1×10^{17}	4490	740
5×10^{17}	2670	600
1×10^{18}	2000	520
5×10^{18}	1260	360

Table 4-1: GaSb electron and hole mobilities as a function of doping concentration.

Recombination Models

For recombination models, we specify Shockley-Read-Hall (SRH), Auger, radiative, and surface recombination mechanisms. The equations employed are described herein. Table 4-2 at the end of this section lists the parameter values used and their references.

Shockley-Read-Hall (material model=SRH) –The SRH recombination is calculated by Equation 4-14. Here τ_{SRHn} and τ_{SRHp} are the SRH electron and hole carrier lifetimes, respectively, and are user-defined. E_{trap} is the energy difference between the trap level and the intrinsic Fermi level. We assume that E_{trap} is zero such that we have only mid-gap trap states. This reduces Equation 4-14 to Equation 4-15. Note that this lifetime will decrease for both increased temperature and increased doping. However, there is

not enough data to describe the GaSb SRH lifetimes τ_{SRHn} and τ_{SRHp} as a function of temperature and doping, so these values must be approximated from the few reported values [80], [81] .

$$R_{SRH} = \frac{pn - n_i^2}{\tau_{SRHn}\left[p + n_i \exp\left(\frac{E_{trap}}{kT}\right)\right] + \tau_{SRHp}\left[n + n_i \exp\left(\frac{-E_{trap}}{kT}\right)\right]} \quad \text{4-14}$$

$$R_{SRH} = \frac{pn - n_i^2}{\tau_{SRHn}[p+n_i] + \tau_{SRH}[n + n_i]} \quad \text{4-15}$$

Radiative (material model=optr) – This model is only applied if the radiative recombination coefficient ("COPT") is specified on the material statement. In Atlas the radiative recombination is defined by Equation 4-16.

$$R_{OPT} = C_{OPT}(np - n_i^2) \quad \text{4-16}$$

Auger (material model=aug) – Auger recombination is modeled by Equation **4-17**. In Silvaco auger coefficients A_n and A_p must be specified by "augn" and "augp".

$$R_{AUGER} = A_n(pn^2 - nn_i^2) + A_p(np^2 - pn_i^2) \quad \text{4-17}$$

Surface –The surface recombination is given by Equation **4-18** which reduces to equation **4-19** for E_{trap}=0. The effective lifetime at the surface is calculated from the bulk lifetime at a user defined interface region of length *d* and area *A* with electron and hole recombination velocities S.N and S.P, Equations **4-20** and **4-21**. The default

recombination velocity for GaSb is 0 and, therefore, to include surface recombination this value must be overwritten.

$$R_{surf} = \frac{pn - n_i^2}{\tau_{n\_eff}\left[p + n_i \exp\left(\frac{E_{trap}}{kT}\right)\right] + \tau_{p\_eff}\left[n + n_i \exp\left(\frac{-E_{trap}}{kT}\right)\right]} \quad 4\text{-}18$$

$$R_{surf} = \frac{pn - n_i^2}{\tau_{n\_eff}[p+n_i] + \tau_{p\_eff}[n + n_i]} \quad 4\text{-}19$$

$$\frac{1}{\tau_{n\_eff}} = \frac{1}{\tau_n} + \frac{d}{A} S.N \quad 4\text{-}20$$

$$\frac{1}{\tau_{p\_eff}} = \frac{1}{\tau_p} + \frac{d}{A} S.P \quad 4\text{-}21$$

MODEL	PARAMETER	REF.
SRH	τ_{SRHe}=10ns τ_{SRHh}=10ns	[80] [81]
Radiative	$C_{OPT} = 8.5 \times 10^{-11}$ cm^3/s	[80]
Auger	A_n, $A_p = 5 \times 10^{-30}$ cm^6/s	[80]
Surface	S.N, S.P=10^6 cm/s	[82]

Table 4-2: GaSb recombination model parameters used in this work and their references.

Thermionic Emission and Tunneling Models

To properly simulate a barrier structure, in addition to the standard drift-diffusion equations, additional models must be included to account for thermionic emission over the barrier and tunneling through the barrier. The electron and hole current density due to thermionic emission at a heterojunction is given by Equations **4-22** and **4-23**. Here v_n and v_p are the electron and hole thermal velocities, which are given by Equations **4-24** and **4-25**, where A_n^* and A_p^* are the Richardson constants. The Richardson constants, in turn, are given by Equations **4-26** and **4-27**. When this value is different for the two constituent semiconductor layers of the heterojunction, the Richardson constant of the lesser value is used in the calculation [83]. The electron and hole effective masses can be specified by m.vthp and m.vthn on the material statement. If they are not specified, they are calculated from the valence and conduction band density of states.

$$\overrightarrow{J_n} = qv_n(1+\delta)\left(n^+ - n^-\exp\left(\frac{-\Delta E_c}{kT}\right)\right) \quad \text{4-22}$$

$$\overrightarrow{J_p} = qv_p(1+\delta)\left(p^+ - p^-\exp\left(\frac{-\Delta E_v}{kT}\right)\right) \quad \text{4-23}$$

$$v_n = \frac{A_n^* T^2}{qN_C} \quad \text{4-24}$$

$$v_p = \frac{A_p^* T^2}{qN_V} \quad \text{4-25}$$

$$A_n^* = \frac{4\pi q k^2 m_n^*}{h^3} \quad \text{4-26}$$

$$A_p^* = \frac{4\pi q k^2 m_p^*}{h^3} \quad \text{4-27}$$

In Equation **4-22**, gamma is the tunneling factor due to thermionic field emission. This value is zero by default, but if “tunnel” is specified on the interface statement, the tunneling factor is calculated by a separate equation. This model, however, only accounts for tunneling at the interface. A more accurate approach is to use a non-local model to account for tunneling across the entire quantum region. The tunneling can be calculated across the whole quantum region using Equation **4-28**, where the current is calculated for all energies at which tunneling is possible. Here the terms E_{Fr} and E_{Fl} are the quasi-Fermi levels on either side of the barrier. The tunneling probability, T(E), is calculated from the solution of the 1D Schrödinger equation. The default calculation for this method is the transfer matrix method, although other methods can be enabled.

$$J = \frac{qkT}{2\pi^2 h^3}\sqrt{m_y m_z}\int T(E)\ln\left\{\frac{1+exp[(E_{Fr}-E)/kT]}{1+exp[(E_{Fl}-E)/kT]}\right\}dE \qquad \text{4-28}$$

This model can be included to account for tunneling of electrons and holes by specifying SIS.EL and SIS.HO on the models statement. A quantum region must be defined over which the tunneling may occur by defining QTREGION which ends on either side of the barrier.

4.1.4 Contact specification

Contacts are assumed to be ohmic unless a work function is defined on the contact statement. The effect of a Schottky contact, however, can be investigated by specifying the work function of the metal on the contact statement. This effect is not included in this work, but should be investigated for future simulation studies.

4.2 Material Design

To engineer a barrier structure we must design a wide bandgap superlattice material with the proper band alignment to our absorber material, as described in Section 3.1. The band structure of a material can be calculated in general by either atomistic methods, which build up the electronic structure one atom at a time, or continuum methods, which take a more global approach. While the atomistic model may be more precise, this approach can be computationally taxing for structures that are many atoms thick. As such, we choose a continuum approach here to model our superlattice structures. We use the program NextNano [78] which employs the semi-empirical multiband k·p method combined with the envelope function approximation.

4.2.1 The k·p method

The electronic behavior of a semiconductor material arises from the contributions from all electrons and nuclei within the material. We can simplify this problem by the adiabatic approximation – namely, we can assume that the atomic cores are stationary and apply a mean-field approximation for all of the other particle interactions. The problem can then be described by the Schrödinger equation of an electron in a periodic potential, Equation **4-29**, where *p* is the momentum operator, *V* is the potential, *m* is the electron mass, *psi* is the wave function, and *E* is the energy.

$$E_n\psi_n = (\frac{p}{2m} + V)\psi_n \qquad \text{4-29}$$

The wave function obeys Bloch's theorem and can, therefore, be written by Equation **4-30**, where the wave function is the product of a plane wave and the Bloch

function u_{nk}. Here k is the wave vector, n is the band index, and u_{nk} is a function with the same periodicity as the crystal lattice.

$$\psi_{n,k}(\boldsymbol{x}) = e^{i\boldsymbol{k}\cdot\boldsymbol{x}} u_{n,\boldsymbol{k}}(\boldsymbol{x}) \quad \text{4-30}$$

We can re-write the Schrödinger equation in terms of this periodic function and an operator H known as the Hamiltonian, Equation **4-31**, where the Hamiltonian is given by Equation **4-32**. The product k·p is the dot product of the wave vector with the momentum operator, Equation **4-33**. At the gamme point when the wave vector k = 0, the Hamiltonian is H_0. We can then rewrite the equation in terms H_0 and H_k', where H_k' is the perturbation term.

$$E_n(k) u_{n,\boldsymbol{k}}(\boldsymbol{x}) = H_k u_{n,\boldsymbol{k}}(\boldsymbol{x}) \quad \text{4-31}$$

$$H_k = \frac{p^2}{2m} + \frac{\hbar \boldsymbol{k}\cdot\boldsymbol{p}}{m} + \frac{\hbar^2 k^2}{2m} + V \quad \text{4-32}$$

$$\boldsymbol{k}\cdot\boldsymbol{p} = k_x\left(-\boldsymbol{i}\hbar\frac{\partial}{\partial x}\right) + k_y\left(-\boldsymbol{i}\hbar\frac{\partial}{\partial y}\right) + k_z(-\boldsymbol{i}\hbar\frac{\partial}{\partial z}) \quad \text{4-33}$$

$$H = H_0 + H_k, H_0 = \left(\frac{p}{2m} + V\right), H_k{}' = \frac{\hbar\boldsymbol{k}\cdot\boldsymbol{p}}{m} + \frac{\hbar^2 k^2}{2m}, \quad \text{4-34}$$

For each band n, there will be a relationship between the energy E at a given state and the wave vector k. This is the band dispersion and from this information we can calculate both the bandgap and the effective mass (see Section 2.1). For non-degenerate bands, the solution is unique at k=0, and the k·p solution with no spin-orbit coupling is given as by Equations **4-35** and **4-36**. The momentum matrix can be re-written as Equation **4-37**, where the latter term is the optical matrix element.

$$u_{n,\boldsymbol{k}} = u_{n,\mathbf{0}} + \frac{\hbar}{m}\sum_{n'\neq n}\frac{\langle u_{n,\mathbf{0}}|\boldsymbol{k}\cdot\boldsymbol{p}|u_{n',\mathbf{0}}\rangle}{E_{n,\mathbf{0}} - E_{n',\mathbf{0}}}u_{n',\mathbf{0}} \quad \text{4-35}$$

$$E_{n,\boldsymbol{k}} = E_{n,\mathbf{0}} + \frac{\hbar^2k^2}{2m} + \frac{\hbar^2}{m^2}\sum_{n'\neq n}\frac{\left|\langle u_{n,\mathbf{0}}|\boldsymbol{k}\cdot\boldsymbol{p}|u_{n',\mathbf{0}}\rangle\right|^2}{E_{n,\mathbf{0}} - E_{n',\mathbf{0}}} \quad \text{4-36}$$

$$\langle u_{n,\mathbf{0}}|\boldsymbol{k}\cdot\boldsymbol{p}|u_{n',\mathbf{0}}\rangle = \boldsymbol{k}\cdot\langle u_{n,\mathbf{0}}|\boldsymbol{p}|u_{n',\mathbf{0}}\rangle \quad \text{4-37}$$

While one can solve for many bands, the optoeletronic behavior of a material can be approximated by looking at the lowest conduction band and the top valence bands - the heavy hole, light hole, and split-off bands. All other bands may be treated as perturbations. Additionally, spin and strain can be added to the Hamiltonian as a perturbation. The spin-orbit interaction is included by adding an additional term as in Equation **4-38**, where sigma is the Pauli spin matrix vector.

$$H_k = \frac{p^2}{2m} + \frac{\hbar\boldsymbol{k}\cdot\boldsymbol{p}}{m} + \frac{\hbar^2k^2}{2m} + V + \frac{\hbar}{4m^2c^2}(\nabla V\times(\boldsymbol{p}+\hbar\boldsymbol{k}))\cdot\vec{\sigma} \quad \text{4-38}$$

Including spin, the four bands lead to an 8-band model. Under the coupling of these 8 bands, the Hamiltonian becomes an 8x8 matrix. The Hamiltonian for zincblend materials can be found in reference [84].

4.2.2 The modified k·p method for heterostructures

For heterostructures, such as superlattices, the translational symmetry of the bulk crystal is broken. In this case, the envelope function approximation (EFA) can be used along with the k·p method to calculate the electronic structure of a system based on the basis of the bulk materials. The general idea is that the k·p Hamiltonian of each

constituent material is “patched up” by the envelope function. The derivation of this method is found in references [85][86].

4.2.3 Simulation input and outputs

In NextNano the bandstructure is calculated using the model described above. The relevant inputs in the program are the quantum structure and the constituent materials. We define one period of the superlattice structure and set periodic boundary conditions. The relevant outputs are the wave functions, electron and hole densities, band structure, and strain. Multiple flow-schemes can be used within the program. Here, we use a scheme that first reads in the potentials and Fermi levels and then calculates the eigenfunctions accordingly.

5 Experimental Methods

5.1 Epitaxial Growth

In this section, the various growth methods for antimonide materials are noted and the advantages of using molecular beam epitaxy are discussed. The molecular beam epitaxy technique is then described in more detail, with specific attention to antimonide growth.

5.1.1 III-V Growth Techniques

Techniques used to grow III-V materials include metal-organic chemical vapor deposition (MOCVD), liquid phase epitaxy (LPE), and molecular beam epitaxy (MBE). Of these various methods, MBE is best suited for antimonide and superlattice material growth. MOCVD has proven difficult for antimonide growth due to the lack of precurser materials for the antimonides and the higher growth rates and temperatures required. Moreover, for a bulk technique like LPE, it can be difficult to have the control necessary to grow the fine layers required for superlattice structures. With MBE, superlattice materials can be grown more readily. The thickness of each layer can be controlled with appropriate shuttering of the source materials. Moreover, the ultra-high vacuum allows for high-purity material growth.

5.1.2 Molecular Beam Epitaxy

The samples in this work are grown by molecular beam epitaxy (MBE). In this technique, materials are grown by evaporating source material onto a temperature-controlled substrate under ultra-high vacuum, ~10^{-10} Torr, **Figure 5-1**. The elements

incorporated are kept in crucibles and heated until they sublime. The evaporated materials form a beam of particles which is directed at the surface of the substrate. As the atoms adhere to the substrate, they form an epilayer. The composition of the epilayer grown on the surface is controlled by the beam flux, which is in turn controlled by the temperature of the crucible. The temperature is monitored by both a thermocouple on the substrate heater and also an optical pyrometer from across the chamber. The flux of atoms arriving to the sample surface is monitored using a beam flux monitor (BFM) – an ion gauge that is inserted into the beam path and can be used to read the "beam equivalent pressure" or BEP.

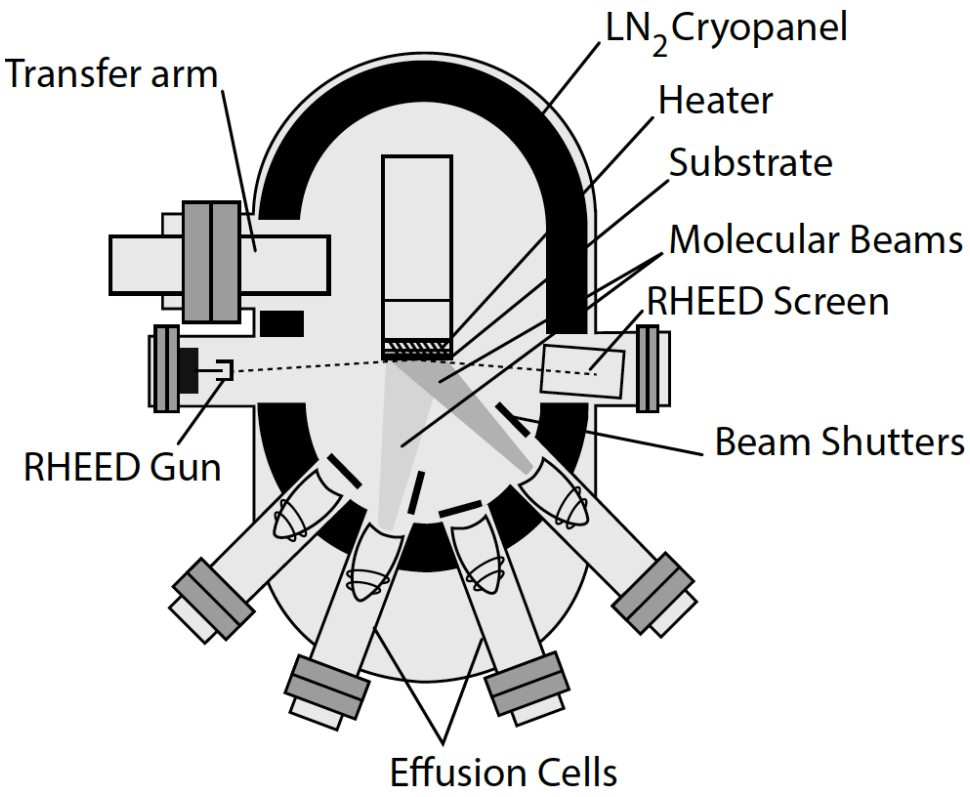

Figure 5-1: Schematic of a molecular beam epitaxy system. Crucibles in effusion cells hold the materials which are heated until they sublime. The beam of particles is directed toward the substrate which is also heated. The substrate rotates so that a uniform layer will form.

The material's growth rate can be determined using reflective high energy electron diffraction (RHEED). In this technique, an electron beam is directed toward the sample at a grazing incident angle. The beam reflects off the sample surface and the diffracted beam is directed toward a screen or camera. The intensity of the diffracted signal changes as the monolayer forms, **Figure 5-2**. The growth rate (number of monolayers/sec) can then be determined by monitoring the periodic variation in intensity from the RHEED oscillations; the growth rate is calculated by dividing the number of oscillations by the total period of time.

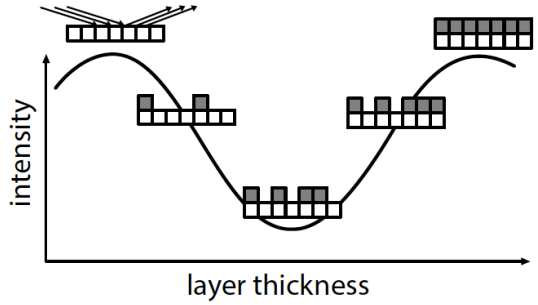

Figure 5-2: The intensity of the RHEED signal varies as a monolayer is formed. By monitoring the variation in intensity, the growth rate can be calculated.

In addition to providing the growth rate, the diffracted image can also be used to determine the structure and quality of the crystalline material, since the observed diffraction pattern is dictated by the crystal structure itself. For GaSb, for example, we observe the following patterns from orthogonal crystal axes, **Figure 5-3**. The clear streaks are evidence of smooth growth.

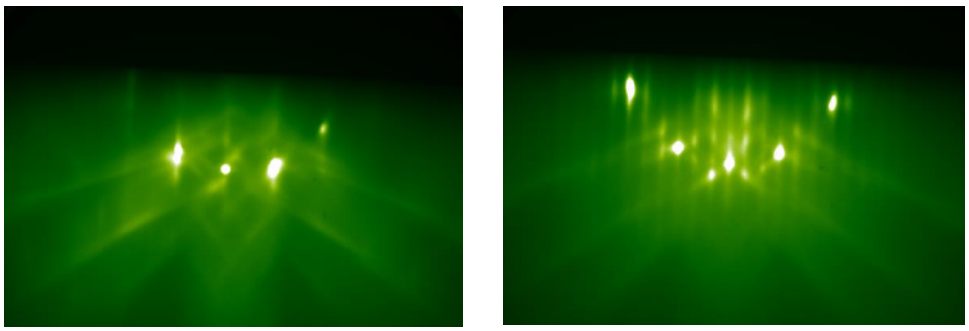

Figure 5-3: RHEED pattern during GaSb growth (left) x1 pattern, (right) x3 pattern

5.1.3 GaSb and InAs/GaSb Superlattice Growth

The growth process begins with an epi-ready wafer. Epi-ready wafers can be purchased doped or undoped. The "nominally undoped" GaSb wafers are actually p-type due to native defects; including gallium vacancies ("V_{Ga}") and gallium atoms in antimony antisites ("Ga_{Sb}"). This is discussed in more detail in Chapter 7.2

Prior to growth on these wafers, the natural oxide of the GaSb wafer must first be removed. During this process an overpressure of antimony is required, as antimony is highly volatile and will readily desorb from the GaSb surface. Desorption of antimony would leave gallium atoms to pool together forming clumps, resulting in roughening of the surface. An overpressure of antimony helps to replace the antimony that continually desorbs, allowing for a smoother surface. The oxide is entirely removed when the substrate temperature reaches around 515°C. However, it is common practice to bring the wafer temperature to 10-15°C higher to ensure that the oxide is entirely removed. The removal of the oxide layer may be monitored through RHEED. As the oxide is removed, faint spots begin to appear in the RHEED, which sharpen once the oxide is completely removed, **Figure 5-4**. After the oxide is removed, the temperature is lowered

to the growth temperature, the appropriate shutters are opened and growth of the epi-layer begins.

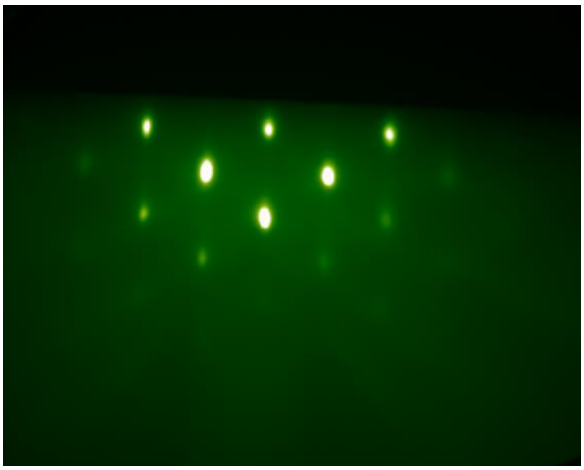

Figure 5-4: RHEED pattern observed after oxide removal on GaSb

The complete growth recipe details for GaSb and InAs/GaSb can be found in Appendix A. The superlattice structures follow the same oxide removal on GaSb substrates, but are grown at lower temperatures than GaSb. Superlattice structure growth also has the additional complication of switching between materials. The shutter sequence is shown in **Figure 5-5**. For growing superlattice structures, in between each constituent layer, a short "soak" is done to pre-condition the surface for the next layer. For example, after growing InAs, a flux of Sb is made for several seconds before growing GaSb. Likewise, after growing GaSb, a flux of As is made for several seconds before switching back to InAs.

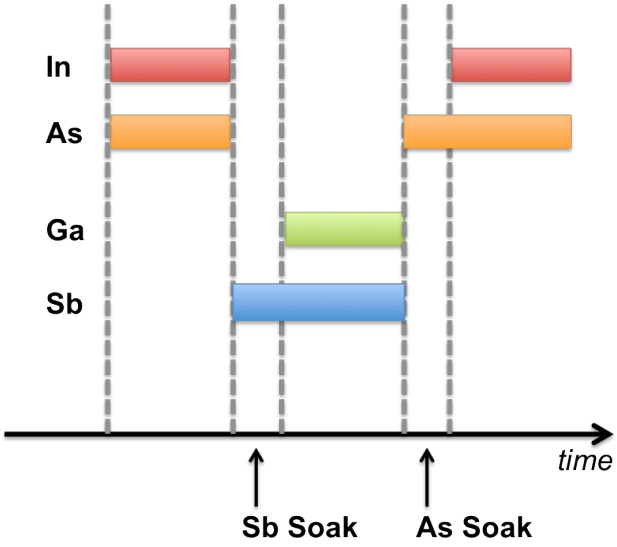

Figure 5-5: Shutter sequence during used in this work during InAs/GaSb superlattice material growth

5.2 Material Characterization

After the materials are grown, the crystal structure is examined by x-ray diffraction. The optical properties are characterized by absorption and photoluminescence measurements and the electrical properties are characterized by Hall measurements. These characterization techniques are described herein.

5.2.1 X-Ray Diffraction

X-ray diffraction (XRD) is a non-destructive process in which X-rays are used to probe the crystal lattice of a sample. Scattering of X-rays from the sample crystal lattice creates a distinct diffraction pattern due to interference of the incident rays reflecting off the crystal surface. The main principle behind this measurement is Bragg's Law, given by Equation **5-1**, where d is the crystal lattice spacing and theta is the angle of the

incident beam. This law says that constructive interference will occur when the wavelength of incident light is equal to 2dsin(θ), or is an integer multiple of this number, **Figure 5-6**.

$$n\lambda = 2d \sin\theta \qquad 5\text{-}1$$

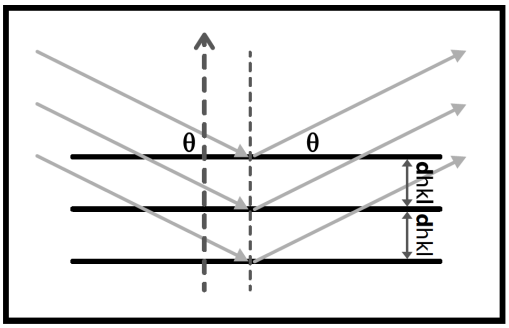

Figure 5-6: Beams incident on a sample crystal surface will interfere constructively when the wavelength is equal to an integer multiple of 2dsin(θ).

The main components for an XRD measurement are the x-ray source, the sample, and the detector, **Figure 5-7**. If the sample is rocked through an angle, the intensity of the diffracted beam from the x-ray will vary, with a peak occurring at the Bragg angle. A plot of the intensity as a function of detector angle (2theta) is called a rocking curve and can be used to characterize the sample structure. This spectrum can be used, for example, to determine the lattice mismatch of an epilayer grown on a substrate. In the spectrum, two peaks are observed: one due to diffraction from the substrate and one due to diffraction from the epilayer, **Figure 5-8**. The lattice mismatch between the epilayer and the substrate may be determined from the distance between the peaks by Equation **5-2**.

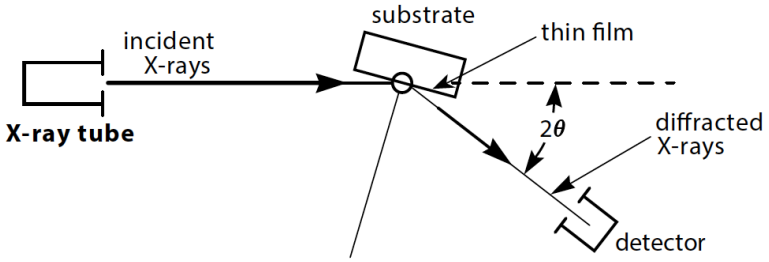

Figure 5-7: Main components in an XRD measurement – X-ray tube, sample, and detector.

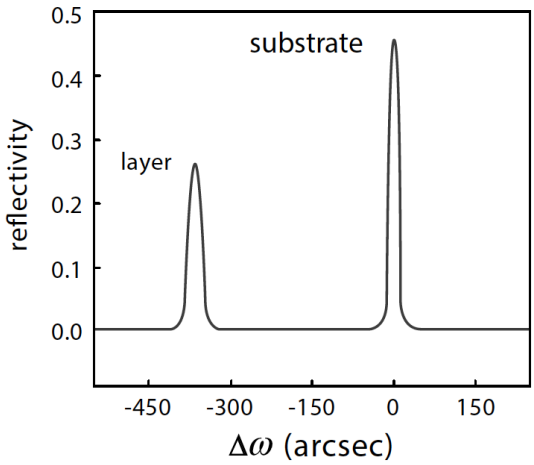

Figure 5-8: Plot of the intensity of the diffracted signal as a function of the angle omega. The difference in peak spacing between an epilayer and a substrate can be used to determine lattice mismatch.

$$\frac{\Delta a}{a} = \frac{\sin\theta_{sub} - \sin\theta_{epi}}{\sin\theta_{sub}} \qquad 5\text{-}2$$

When a superlattice structure is grown, the scan will show periodic peaks known as satellite peaks. The lattice mismatch between the superlattice and the substrate can

be determined from the spacing between the *principal* superlattice peak and the substrate peak. Bragg's equation now can used to determine the average lattice constant d, which is given by the period thickness divided by the total number of monolayers, Equations **5-4** and **5-5**.

$$\frac{1}{\bar{d}} \pm \frac{n}{\mathrm{P}} = \frac{2\sin\theta}{\lambda} \qquad 5\text{-}3$$

$$\bar{d} = \frac{N_A d_A + N_B d_B}{N_A + N_B} \qquad 5\text{-}4$$

$$P = N_A d_A + N_B d_B \qquad 5\text{-}5$$

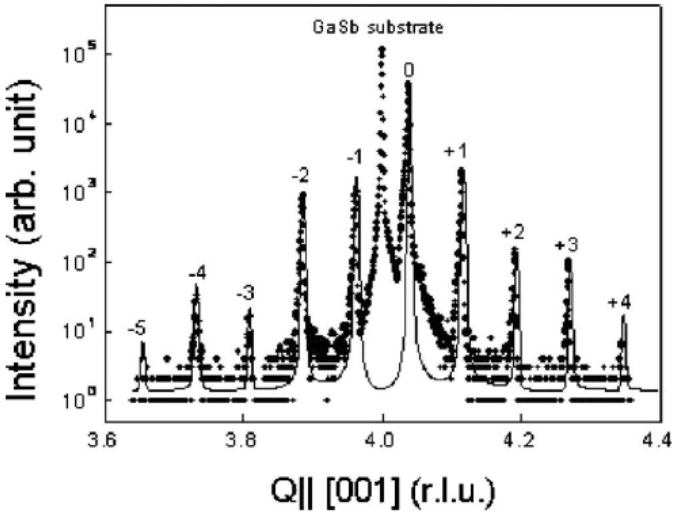

Figure 5-9: Example of an XRD measurement of an InAs/GaSb superlattice structure grown on a GaSb substrate. The lattice mismatch between the epilayer and the substrate is given by the difference between the primary superlattice peak and the GaSb substrate peak. Figure from reference [87].

5.2.2 Hall Effect Measurements

The doping can be determined using a Hall effect measurement setup. This measurement technique uses the Lorentz Force Law: when a magnetic field B is applied perpendicular to moving charges with velocity v, a force will be exhibited orthogonal to both vectors v and B. This force will cause charges to shift in the direction of the force and accumulate, building up a voltage known as the Hall voltage. A Hall effect measurement system takes advantage of this phenomenon. In a Hall measurement, four contacts are made to the sample of interest. Current is applied to two contacts, a magnetic field is applied externally, and the Hall voltage is measured across the remaining pair of contacts (**Figure 5-10**). From the current, magnetic field, and measured Hall voltage, the sheet carrier density (n_s or p_s) may be calculated, Equations **5-6** and **5-7**. Using the thickness of the sample (d), the doping can then be calculated, Equations **5-8** and **5-9**.

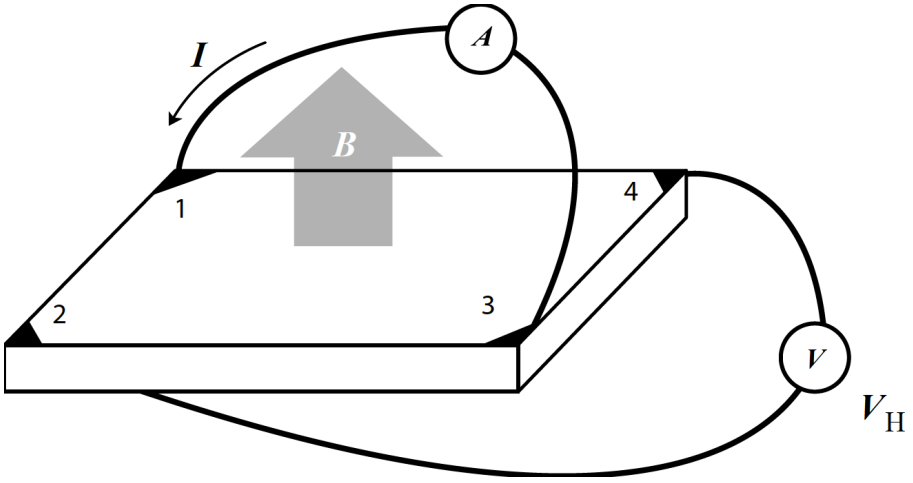

Figure 5-10: Hall effect measurement

$$n_s = IB/q|V_H| \quad 5\text{-}6$$

$$p_s = IB/q|V_H| \quad 5\text{-}7$$

$$n = n_s/d \quad 5\text{-}8$$

$$p = p_s/d \quad 5\text{-}9$$

This setup can further be used to determine carrier mobility. From the measurement of sheet carrier density and sheet resistance, the mobility can be calculated, Equation **5-10** and **5-11**.

$$\mu_n = 1/qn_sR_s \quad 5\text{-}10$$

$$\mu_h = 1/qp_sR_s \quad 5\text{-}11$$

5.2.3 Spectral Absorption

The absorbance of a material is the capacity of a material to absorb light at a given wavelength. When light is incident on a material, the light is absorbed, reflected, or transmitted. The absorbance (*A*) of the material is calculated from Equation **5-12**, where *R* is the reflectivity and *T* is the transmittance, which is the ratio of the intensity of light transmitted through the sample to the initial light intensity incident on the sample, Equation 5-13.

$$A = 1 - R - T \quad 5\text{-}12$$

$$T = \frac{I(\lambda)}{I_0(\lambda)} \quad 5\text{-}13$$

Beer's Law, Equation 5-14, states that the intensity of light will decay exponentially as it moves through a medium. Here, *x* is the depth traveled into the

medium and alpha is the attenuation or absorption coefficient, typically reported in units of cm^{-1}.

$$I(\lambda) = (1 - R)I_0(\lambda)e^{-\alpha x} \quad \text{5-14}$$

To calculate the absorption, both the transmission and reflection must be known. The transmission of light through a sample may be measured via Fourier Transform Infrared Spectroscopy (FTIR). An FTIR setup consists of a light source, a beam splitter, a Michelson interferometer, and a detector, **Figure 5-11**. The light from the source is first split into two parts by a beam splitter. The split beams are then fed to a Michelson interferometer which consists of static and moving mirrors. The moving mirror blocks different frequencies of light as it moves, allowing the spectrum coming out of the interferometer to change dynamically. A laser is used to determine the position of the moving mirror. As the split beams exit the interferometer, they interfere with each other and are directed to the sample compartment. The light that passes through the sample is then picked up by the detector. The signal from the detector is gained and digitized. The computer then transforms the data from absorbance for a given mirror position to absorbance for a given wavelength. For transmission measurements from the near to far IR we use a Nicolet 6700 FTIR with an Ever-Glo light source, KBr beam splitter, and DTGS detector, which together can characterize the range of wavelengths from 1.3 to ~25 μm. Reflectance can be measured using ellipsometry, although this is not at the normal incidence.

Shorter wavelengths (up to 1.1μm) can be characterized using the Agilent Cary 60 UV-VIS, which has a universal measurement accessory (UAM) that allows for transmission and reflectance at the same angle, which, therefore, provides a true measurement of absorbance. Though this setup can only be used to 1.1μm, this could

still be useful for characterizing the near bandgap absorption in GaSb samples with PhCs. An additional option is to deposit gold on the backside of the sample such that no transmission is allowed, and determine the absorbance from the reflection (A=1-R).

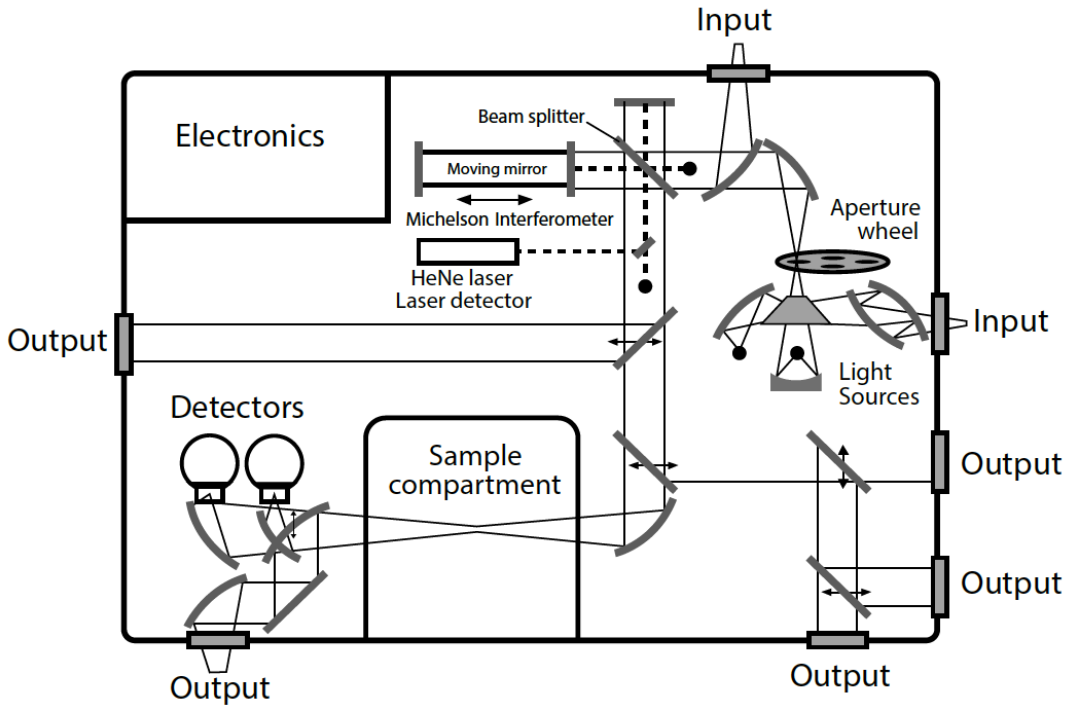

Figure 5-11: Schematic of a FTIR setup

5.2.4 Photoluminescence

Photoluminescence occurs when an electron, brought to an excited state by an external light source, recombines with a hole of a lower energy and releases a photon in the process. Since the majority of these transitions will be from the conduction band to the valence band, by measuring the wavelength of light emitted during this process, we can use a photoluminescence measurement to determine the bandgap of a material.

In a PL measurement setup, the sample is first irradiated with a laser source, **Figure 5-12**. The laser will excite carriers within the material and these carriers subsequently relax and release photons in the process. These photons must then be detected and analyzed. A monochromator is used to select out one wavelength of light at a time so that the photoluminescence may be plotted as a function of wavelength. The signal is transmitted through the monochromator to a photoreceiver. The PL signal may be small and difficult to recover against background noise. A lock-in amplifier is used to extract the signal. For MWIR and longer wavelengths, however, even with the lock-in amplifier, the signal will be difficult to recover against 300K background noise. To further reduce noise, a double-modulation technique can be used by incorporating an FTIR. Rather than using the monochromator to measure one frequency of light at a time, multiple frequencies are measured simultaneously using the FTIR. The FTIR has better sensitivity and therefore the signal to noise ratio (SNR) is improved.

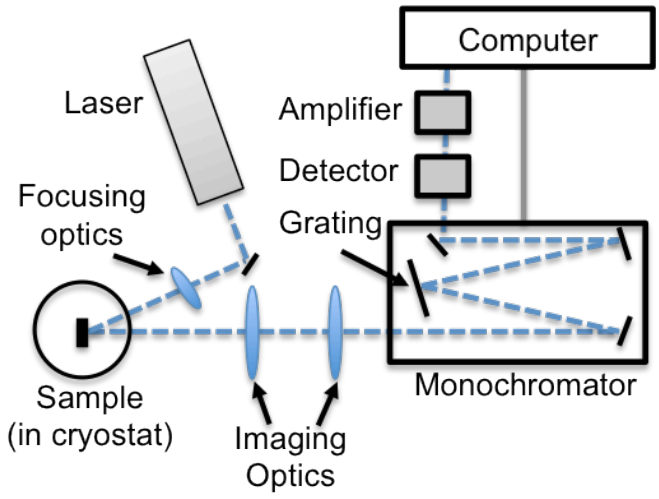

Figure 5-12: Basic PL measurement setup

5.3 Processing

After the material structures have been grown and characterized optically, they can be processed into diodes and tested. Each diode consists of a top and bottom metallic contact which are electrically isolated by a dielectric layer, **Figure 5-13**. To form the diode, the first step is to etch selective areas to the bottom of the p-type absorber, as this is where the bottom contact will be placed. This etching leaves an exposed sidewall; this sidewall must be coated with a dielectric to both reduce parasitic surface currents and prevent shunting between the contacts. The sidewall is coated with a dielectric insulator and then top and bottom metallic contacts are deposited. Lastly, to improve absorption, an anti-reflective coating (ARC) layer or photonic crystals may optionally be added to the front surface of the diode. In this section, the general processing scheme and tools employed are described. Full details of the fabrication process may be found in Appendix B.

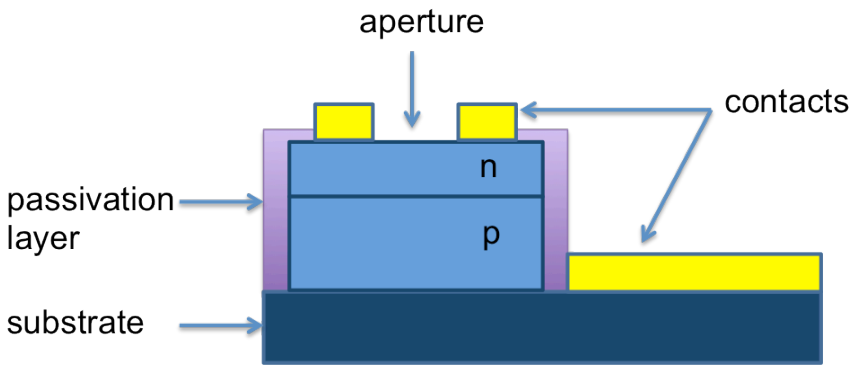

Figure 5-13: Schematic showing the profile of the diode device after fabrication. Top and bottom contacts are separated by a passivation layer. Note that the substrate for this n-on-p configuration is p-type.

Initial sample clean

The sample is first cleaned using a plasma, or ionized gas, to remove any organic contamination. The plasma is formed by exposing oxygen to a high-power radio frequency, which ionizes the oxygen molecules forming monatomic oxygen – a highly reactive species. This plasma species then reacts with the surface of the sample to break up any organic C-H and C-C bonds, forming water vapor and CO_2 which are then pumped out by the vacuum.

Etching to bottom contact

Photolithography is used to pattern the surface to prepare the sample for etching. In this process, a photo-sensitive resist is spun on to the material. The resist is exposed to UV light under a mask, **Figure 5-14**. Upon developing with a positive resist, the photoresist that was exposed to the light is removed, leaving a pattern on the substrate.

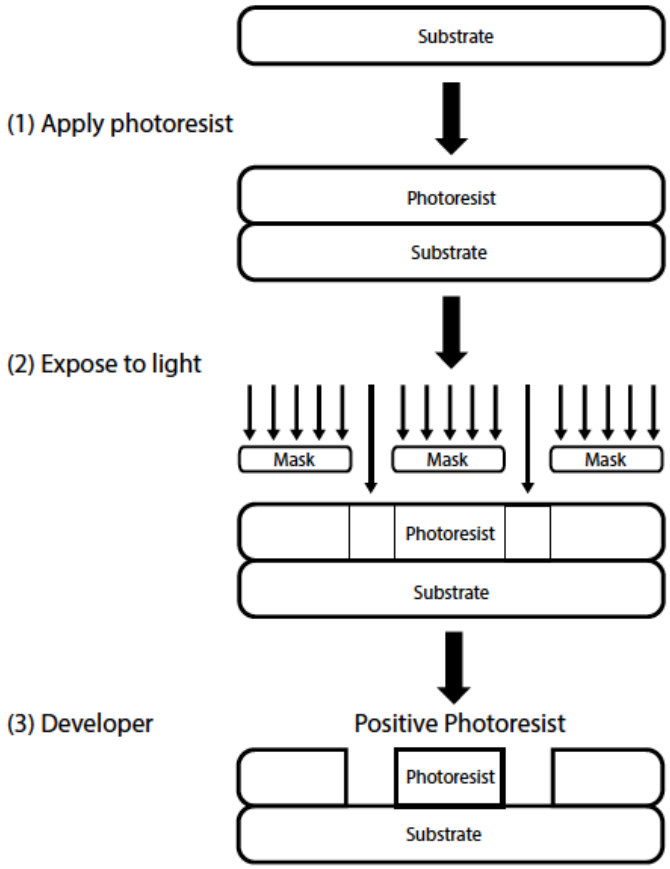

Figure 5-14: Photolithography process flow

Once the sample is patterned with the photoresist, it is ready to be etched. It is important to achieve smooth sidewalls during the etch, as rough sidewalls will result in surface leakage currents, a major issue for III-V diodes. Materials can be etched by either wet (chemical) or dry (physical) processes. While wet-etches may allow for smooth surfaces if done properly, these etches are isotropic, **Figure 5-15**, causing undercutting of the photoresist-covered area which leads to concave sidewalls.

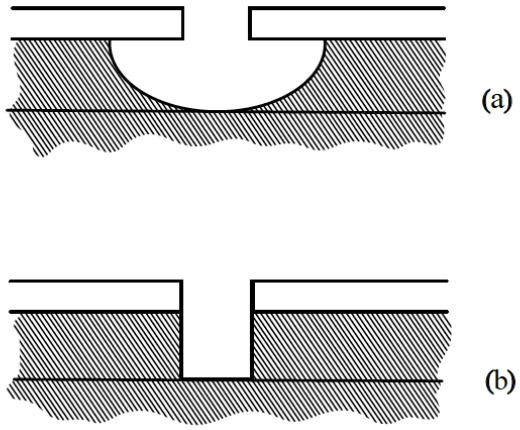

Figure 5-15: (a) Isotropic etching versus (b) anisotropic etching

An alternative method is to use dry etching techniques such as reactive-ion etching (RIE), **Figure 5-16**, which may allow for a more anisotropic etch. In reactive-ion etching, a substrate is placed on a biased electrode facing a grounded electrode. The bias is used to both generate the plasma and accelerate the ions from the plasma toward the surface, etching the sample.

In conventional RIE, the plasma density and etch rate may be limited to low densities. An alternative approach is to use a separate source to generate the plasma in addition to the source that applies the bias. In inductively coupled plasma (ICP) RIE, the RF bias still generates the electric field, but the plasma is generated independently by a separate RF-powered magnetic field, **Figure 5-16** (right). This decoupling allows for higher plasma densities, and thus a higher ion density for bombardment, which leads to a faster etch rate and improved anisotropy when operated at low pressures. In this work we use an Unaxis ICP RIE to etch the III-V material.

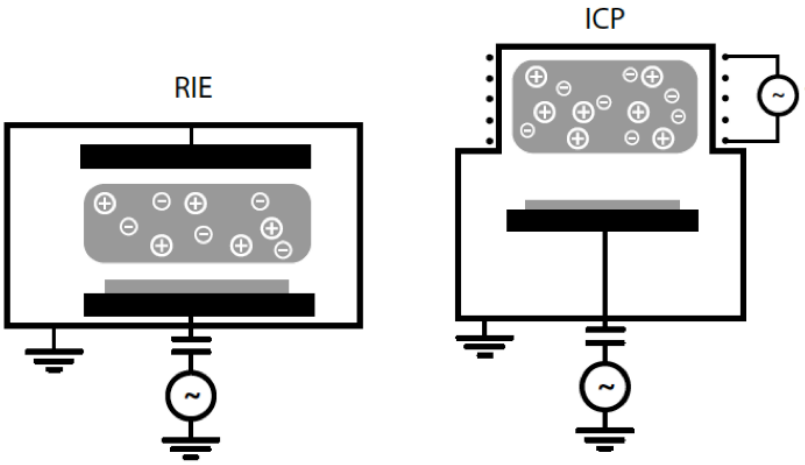

Figure 5-16: Reactive Ion Etching – capacitive RIE (left) versus inductive (right)

For III-V materials such as GaSb, chlorine gas (Cl_2) is often used as an etchant, since III-V-chlorides are highly volatile leading to fast etch rates and smooth surfaces. When etching superlattice materials, the constituent materials may etch at different rates, and the process becomes more complicated. Various studies have been carried out to find the ideal gas combination and flow rates for etching III-Sb superlattice materials [88], [89]. In addition to chlorine gas, boron trichloride (BCl_3) has proven to be an effective etchant, as it helps to remove native oxides and redeposited by-products. Compared to using just BCl_3/Ar or Cl_2/Ar alone, a mixture of BCl_3/Cl_2/Ar has proven to yield smoother surfaces [90]. Other gases, such as methane (CH_4), have also been investigated. Methane is believed to form a thin polymer layer, which can aid in passivation [91]. The recipes used in this work are listed in Appendix B.

SiN sidewall passivation layer

After the sample has been etched, the sidewalls are coated with silicon nitride (Si_3N_4), which will both passivate the sidewall and ensure front and bottom contact isolation. This is an important step, as carrier recombination at an exposed surface is a major source of dark current generation in antimonide devices. The Si_3N_4 layer is deposited by plasma-enhanced chemical vapor deposition (PECVD). In this process, films are formed by the chemical reaction of vapors (also known as precursors) with the sample surface, as depicted in **Figure 5-17**. Energy for the surface reaction is supplied thorough the plasma which is formed by capacitive coupling between two parallel plate electrodes.

In this work we use the STS PECVD, which has a dual frequency parallel electrode reactor. The top electrode can be powered with one of two generators, either high frequency at 13.56MHz (HF) or low frequency (LF) at 380 kHz. Our recipe for Si_3N_4 uses the high frequency generator, as described in Appendix B.

After running this recipe, Si_3N_4 coats the entire sample surface. To leave Si_3N_4 on only the sidewalls, we again use photolithography to pattern the surface of the Si_3N_4 layer, as depicted in **Figure 5-18**. The Si_3N_4 layer is then removed everywhere except for the sidewalls by RIE.

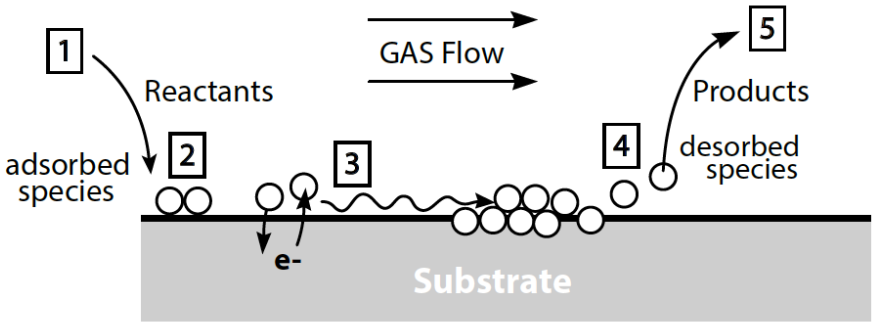

Figure 5-17: Vapor solid surface interaction in PECVD – 1. Diffusion across the layer, 2. Adsorption onto the surface, 3. Surface reaction, film formation 4. Desorption of by-products 5. Diffusion of by-products back into gas

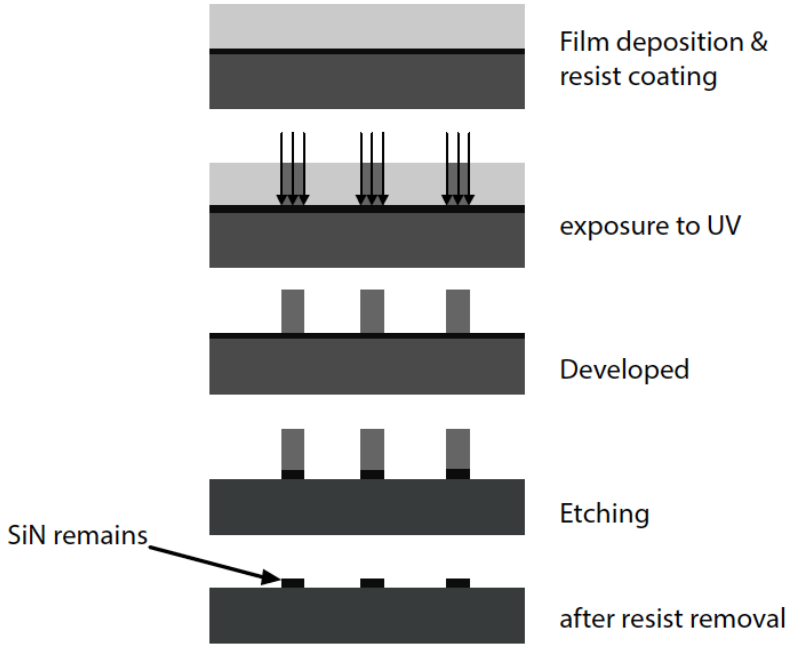

Figure 5-18: SiN patterning process flow

Contact Deposition

The metal layer is formed by a liftoff process, **Figure 5-19**. The surface is first patterned using standard photolithography methods. After developing, the photoresist remains everywhere where the metal should *not* be. The patterned surface is then cleaned thoroughly prior to the metal deposition; the surface is first cleaned with acid and then a plasma stripper. The metal is then deposited by an electron beam evaporator, which is a form of physical vapor deposition method (PVD). By this method, an electron beam is used to evaporate material from an ingot, **Figure 5-20**. The sublimated material then coats the entire surface of the substrate. To reveal the pattern, the samples are put into a solution such that the metal attached to the photoresist can be lifted off. A bi-layer photoresist is used to facilitate the removal of the metal.

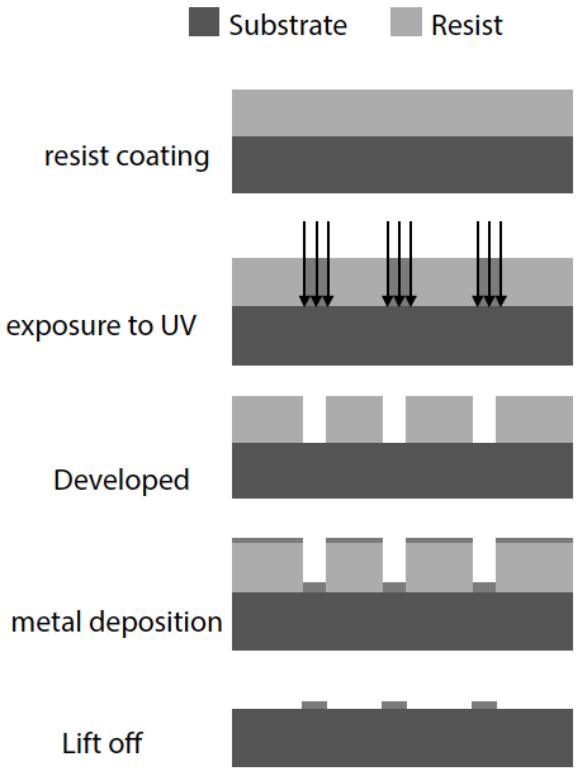

Figure 5-19: Liftoff process

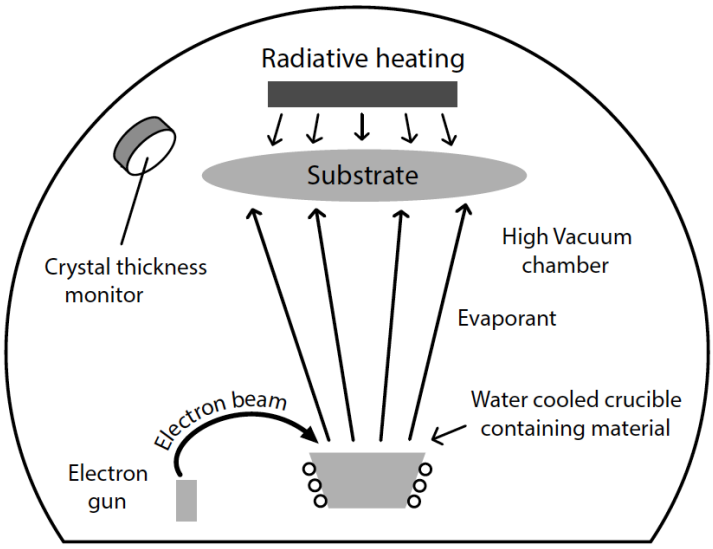

Figure 5-20: Electron beam evaporation for metal deposition

Photonic Crystal Patterning

In our work, a photonic crystal pattern is deposited onto the aperture of our GaSb diodes. The pattern is formed by electron beam lithography, also known as e-beam lithography or EBL. Rather than defining the pattern with a mask and UV light, as in photolithography, the pattern is directly written by an electron beam onto the resist. This allows for smaller feature sizes than with standard photolithography, as the pattern size is not limited by the diffraction limit of light. We use the Raith 250 EBL system at the Center for Nanoscale Systems at Harvard University to define PhC patterns on GaSb diodes.

Anti-reflective coating (ARC)

Lastly, an anti-reflective coating (ARC) may be deposited. The ARC serves several purposes. First, the ARC reduces reflection of light at the diode aperture surface, improving light absorption. Second, for the PhCs, the ARC is deposited between the metallic photonic crystals, creating an alternating index of refraction. As discussed in Chapter 2.3, it is this periodic variation in dielectric constant that gives rise to the photonic crystal effects. The ARC may also reduce front surface recombination by passivating the exposed aperture of the diode.

5.4 Device Characterization

5.4.1 Current-Voltage

The current measurements are taken using a Keithley source-meter, which steps through a range of applied voltages as probes measure the current through the device. For testing under solar conditions, a Newport Oriel Solar Simulator with a 1600W Xenon bulb is used. A neutral density filter is used to reduce the incident light to 1 Sun.

5.4.2 Quantum Efficiency

The quantum efficiency of a device can be determined from the spectrally resolved photocurrent measurement. As with other spectral measurements, such as photoluminescence, the quantum efficiency can be measured by two different means: either with a monochromator-based setup, which takes a measurement at a single wavelength at a time, or with an FTIR setup, which measures all wavelengths

simultaneously. A monochromater-based setup is often used for measurements in the visible or near-IR. However, for mid-wavelength IR, FTIR is required since it has much larger signal to noise ratio. This technique is referred to as Fourier Transform photospectroscopy.

6 Extending the wavelength of TPV diodes

In this chapter, we investigate a monovalent barrier structure for TPVs with the aim of reducing the dark current and improving the open-circuit voltage in these devices, as discussed in Section 3.2. In Section 6.1, we first detail the material modeling, where we design superlattice materials to have the desired band alignments for a barrier structure. We then study the effect that this band alignment and material system have on the performance of a TPV diode in Section 6.2. In Section 6.3, we present the experimental results. In Section 6.4, we summarize the simulation and experimental results and discuss the prospect of these structures for TPVs.

6.1 Material Design

The barrier structure is composed of a regular PN diode with a wide bandgap layer inserted in between the P and N layers. For this study, we choose an n-on-p diode architecture, because the longer diffusion length of electrons in the p-type absorber improves device performance, Section 3.1. For the n-on-p structure, the barrier is in the valence band, so as not to block the photogenerated carriers, **Figure 6-1** – left.

To achieve this structure we must choose two materials with different bandgaps but matching conduction bands, such that the band offset is entirely over the valence band. As discussed in Chapter 3, we employ superlattice materials to do so since the band alignment can be readily tuned by varying the constituent layers, **Figure 6-1** – right. We first design the absorber material to have the desired bandgap: this should be ~0.25eV for a target cutoff wavelength ~5μm, corresponding to 1000°C source

temperatures. We then design the barrier material to have the desired alignment to the absorber.

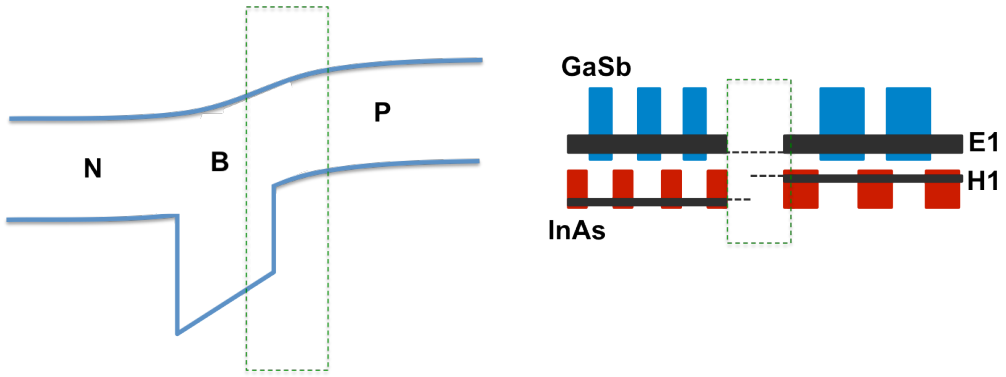

Figure 6-1: Left – band structure for a monovalent barrier diode. Right – schematic showing how varying the superlattice constituent layers varies the position of the conduction and valence bands (E_1 and H_1), allowing us to engineer the offset shown on the left.

6.1.1 Absorber

Using Nextnano and the k·p EFA method described in Section 4.2, we simulate the electronic band structure of a (10,13) InAs/GaSb superlattice – a superlattice with a single period consisting of 10 monolayers (MLs) of InAs and 13 MLs of GaSb. These simulations were done at zero Kelvin since the Varshni parameters were not known *a priori*. The bulk band structure, along with the first quantized energy levels E_1 and H_1 and their respective wave functions (Ψ_{E1}) and (Ψ_{H1}), is plotted in **Figure 6-2**. We see that the transition energy between E_1 and H_1 corresponds to a bandgap of 268 meV and, therefore, a cutoff wavelength at 4.63 μm at zero Kelvin.

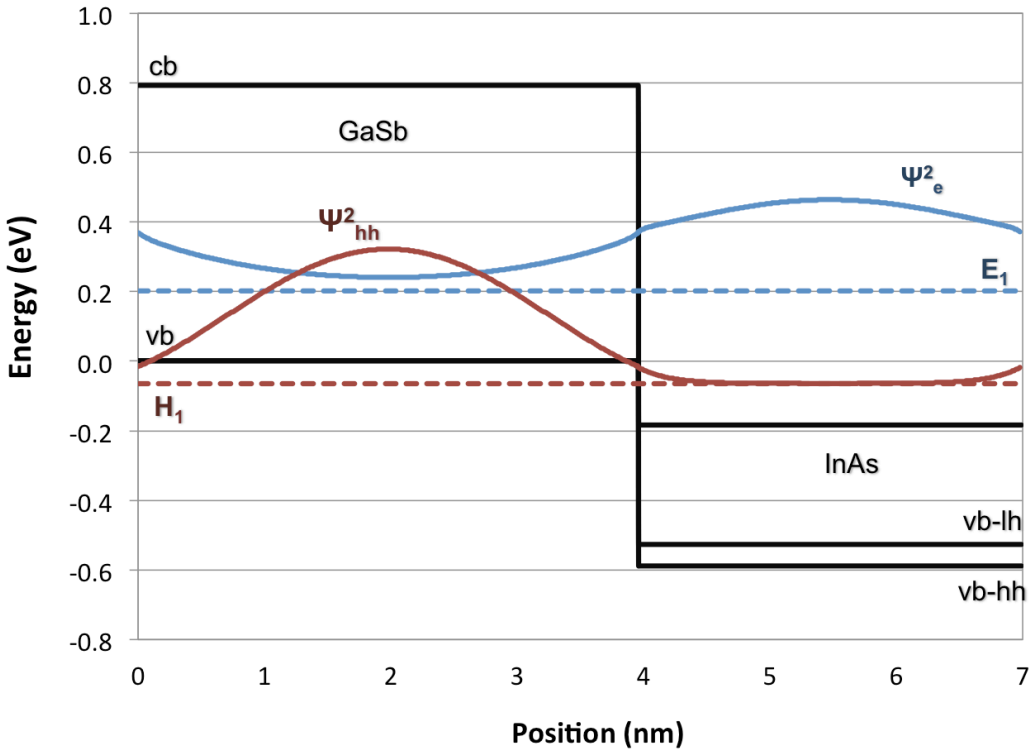

Figure 6-2: Calculated bandstructure for the (10/13) InAs/GaSb superlattice. Solid lines show the conduction (cb), heavy hole (vb-hh), and light hole (vb-lh) bands the constituent bulk materials. Wave functions (Ψ) are plotted to show the confinement of the electrons and holes in the InAs and GaSb wells, respectively. Dotted lines show the first quantized energy levels for the electrons (E1) and holes (H1) in the superlattice. The difference in energy between E1 and H1 corresponds to a bandgap of 268 meV at zero Kelvin.

The (10/13) InAs/GaSb superlattice material was grown using a Riber Compact 21 MBE system at the NanoMIR laboratory in Montpellier, France. XRD measurements were taken to verify the period thickness and to ensure lattice matching to the GaSb substrate. The 004 omega-2theta scan is shown in **Figure 6-3**. The superlattice structure is indeed lattice matched to the substrate, as evidenced by the alignment of the primary superlattice satellite peak with the GaSb substrate peak. The measured period

thickness and lattice mismatch were 6.96nm (23.2 monolayers) and 0.027%, respectively.

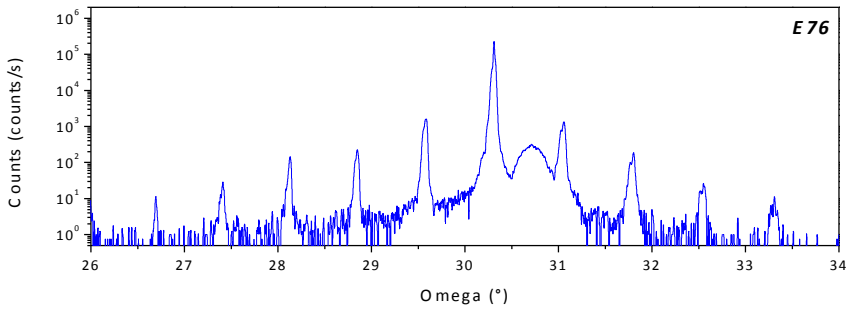

Figure 6-3: XRD measurement of the (10/13) InAs/GaSb superlattice material grown on top of a GaSb substrate. The superlattice is lattice matched to the GaSb substrate, as evidenced by the location of the primary superlattice peak which is aligned with the substrate peak. The large round peak corresponds to a 20nm thin InAs capping layer.

Photoluminescence measurements were taken to determine the bandgap of the material. Although we are ultimately interested in the bandgap at room temperature, the PL signal can be difficult to measure at this temperature due to background noise, and, therefore, we measure the bandgap at lower temperatures where the signal can be more readily resolved. By taking several measurements at lower temperatures, we can calculate Varshni's parameters and then calculate the bandgap at room temperature by Varshni's equation, Equation **6-1**. Here, E_0 is the bandgap at zero Kelvin and α and β are the Varshni parameters.

$$E(T) = E_0 - \alpha T^2/(T+\beta) \qquad 6\text{-}1$$

Measurements were taken at 10K and 80K, yielding peak wavelengths at 4.59μm and 4.63μm, respectively, which correspond to bandgaps of 0.270eV and

0.268eV, **Figure 6-4**. The low temperature measurement at 10K is in good agreement with our simulations detailed above. Using Varshni's equation with α =0.3meV [92], E_0 approximated as 0.270eV, and the bandgap measured at 80K, we calculate a β value of 876K. With these alpha and beta values we can then calculate the bandgap at room temperature to be of 0.247 eV, which corresponds to a cutoff wavelength of 5.0 μm.

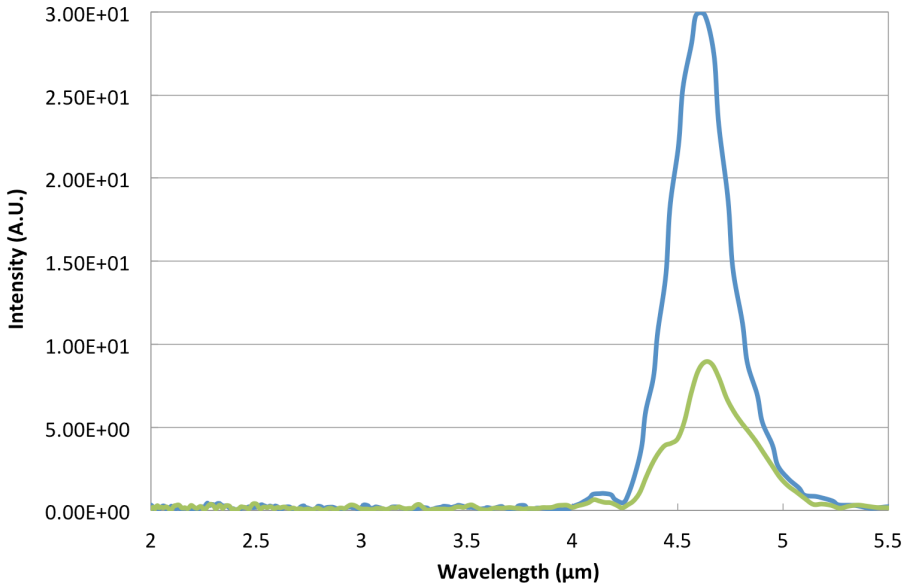

Figure 6-4: Measurement of photoluminescence from a (10/13) InAs/GaSb superlattice structure at 10K (blue) and 80K (green). The peak wavelength at 80K is at 4.63 μm which corresponds to a bandgap of 268 meV.

6.1.2 Barrier

Initially, we designed and fabricated an InAs/GaSb superlattice barrier material. However, we were not able to form a wide bandgap with this material system. In order to engineer a wide bandgap, the constituent layers had to be made very thin – only a few monolayers. This can be understood by recalling the particle in a box model from quantum mechanics. As the quantum well width decreases, the confined energy layer

gets pushed up and away. This is the case in superlattice structures as well – as the thickness of the constituent layers decreases, the electron and hole wave functions are squeezed away from each other and the bandgap increases. To achieve a wide bandgap then, the superlattice must be composed of thin layers. However, as the number of monolayers decreases, the envelope modeling methods that we employ are no longer accurate. For example, the bandgap of a (5/4) InAs/GaSb superlattice that we grew and measured was 50meV away from the simulated value. This can attributed to the fact that for a structure only a couple of monolayers thick, the material is neither digital alloy nor superlattice; this regime is difficult to model and has been a subject of research in itself [93].

To ensue a wide bandgap, another design was made in which aluminum was included in the superlattice layer. Aluminum-containing layers naturally lend wider bandgaps. For example, AlSb has a bandgap of 1.61eV at room temperature, as shown in **Figure 6-5**, along with the band offsets to InAs and GaSb.

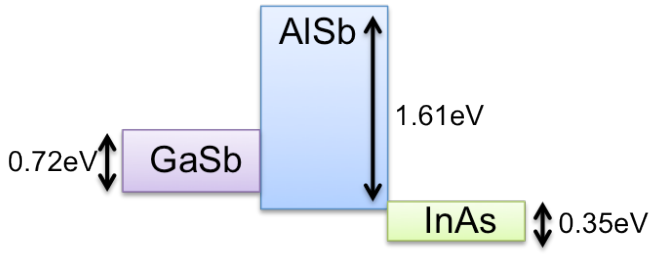

Figure 6-5: Band alignments for AlSb with InAs and GaSb. AlSb has a type-I (straddling) alignment with GaSb and a type-II (staggered) alignment with InAs.

Three main types of AlSb-containing superlattice variants have been explored for monovalent barrier structures for MWIR photodetectors: (1) InAs/AlSb [94][95], (2) InAs/AlSb/GaSb/AlSb or “M” structure [96][97][98], and (3) InAs/AlSb/GaSb/InAs or “N”

structure [99–101] (**Figure 6-6**). The M- and N-structures both use a very thin AlSb layer to push the electron and hole wave functions in InAs and GaSb toward each other, increasing the wave function overlap and therefore the absorption. While this structure could be more promising than the InAs/AlSb structure, we employ the InAs/AlSb structure in this work as it is more straightforward to model and grow.

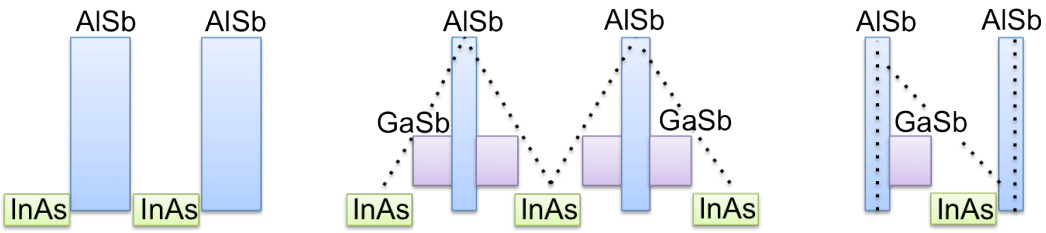

Figure 6-6: AlSb-containing superlattice materials that have been incorporated into MWIR photodetectors: (left) InAs/AlSb, (center) InAs/GaSb/AlSb/GaSb or “M-structure”, and (right) AlSb/GaSb/InAs/AlSb or “N-structure”.

We can achieve the desired bandgap and band alignment by varying the composition of the InAs/AlSb superlattice structure. In the InAs/AlSb superlattice, electrons are confined within the InAs layers to make up the electron minibands and holes are confined within the AlSb layers to make up the hole minibands. As such, if we fix the AlSb thickness and vary the InAs well thickness, we can shift the electron miniband or conduction band level, adjusting the thickness of the InAs well to correspond to a conduction band level in accordance with that of our absorber material. Rather than designing only one barrier material to have a conduction band perfectly matched to the absorber, we chose to design several materials with varying offsets, such that even if the simulation is off by +/-50meV, experimentally we would still arrive at a matched structure. Three structures with different conduction band offsets are shown in **Table 6-1**, along with their lattice mismatch (LMM) to the GaSb substrate. The

structures are designed so that the LMM is < 3000 ppm (< 0.3%), because beyond this value, growth defects and dislocations result, leading to a rough surface and poor optical and electrical performances.

InAs/AlSb ML ratio	ΔE_C (meV)	ΔE_V (meV)	LMM (PPM)
10/7	49	437	1000
12/7	-21	439	1500
14/7	-76	441	2000

Table 6-1: Simulated values for the conduction band offset (ΔE_C) and barrier height (ΔE_V) for various InAs/AlSb superlattices to the (10/13) InAs/GaSb absorber material. Lattice mistmatch (LMM) to the GaSb substrate is also listed in parts per million (PPM).

6.2 Device Design and Simulations

In the previous section, we designed superlattice materials to yield the desired band alignments for our barrier structures. In this section we will incorporate these materials into a barrier structure and study the affect that a monovalent barrier has on TPV device performance.

6.2.1 Current pathways in a barrier structure

In Section 2.1.3 we discussed the dark current pathways for a PN diode. For a monovalent barrier device, the path for hole carriers will be interrupted. Holes may only contribute to the dark current by tunneling through the barrier or gaining enough thermal energy to be excited over the barrier via thermionic emission. The probability of transmission for a carrier to tunnel through the barrier is given by Equations **6-2** and **6-3**, where x is the width of the barrier. Using this equation, for our valence band offset and a

barrier thickness of 100nm, we calculate the transmission probability to be extremely low – on the order of 10^{-31}. Any dark current from hole carriers in this structure will then be entirely due to thermionic emission over the barrier.

$$T(E) = e^{-2kx} \quad 6\text{-}2$$

$$k = \sqrt{\frac{2m}{h^2}(V_0 - E)} \quad 6\text{-}3$$

6.2.2 Doping

What levels of doping should we use in this device? Having a high doping is beneficial as it improves the open-circuit voltage, which is necessary for our narrow bandgap diodes that suffer from parasitic dark currents, Section 3.2. In practice, however, important parameters such as mobility and carrier lifetime rapidly decrease with increased doping. In designing a structure we must therefore balance these mechanisms. An additional factor to consider is that in order for the doping to be effective, it must be greater than the intrinsic carrier population. This issue does not affect wide bandgap materials, as the intrinsic carrier population goes as e^{-Eg}, Equation **6-4**. For narrow bandgap diodes, however, the intrinsic carrier population is much larger – rivaling that of the doping level. This effect is compounded for our devices because they must be able to operate at room temperature as opposed to the LN_2 temperatures of narrow bandgap photodetectors. As such, we must verify – will our materials still be extrinsic at room temperature?

We can calculate the intrinsic carrier concentration by Equation **6-4**. Here N_c and N_v are the effective conduction and valence band density of states, respectively, which

are given by Equations **6-5** and **6-6** for a bulk material. These equations assume a parabolic energy dispersion about k_0 in k_X, k_Y, and k_Z, as is often the approximation made for bulk materials. For a superlattice material, however, the additional periodicity from the superlattice in the growth direction means that the dispersion will vary independently in k_{SL}, leading to a different density of states than the in-plane vectors k_X and k_Y. A proposed method for the full calculation of the density of states from the dispersion is detailed in Appendix C. Here, for simplicity, we calculate the effective density of states using the effective mass, Equations **6-7** and **6-8**. We estimate the intrinsic carrier concentration for our superlattice absorber at room temperature to be ~ $1\times10^{16}/cm^3$. From this value, we see that for a doping level of $\geq10^{17}/cm^3$, our diode will still be extrinsic for room temperature operation.

$$n_i = \sqrt{N_c N_v} e^{-\frac{E_g}{2kT}} \tag{6-4}$$

$$N_C = \frac{1}{\sqrt{2}}\left(\frac{m_e^* k_B T}{\pi\hbar^2}\right)^{3/2} \tag{6-5}$$

$$N_V = \frac{1}{\sqrt{2}}\left(\frac{m_h^* k_B T}{\pi\hbar^2}\right)^{3/2} \tag{6-6}$$

$$m_e^* = \left(\left(m_{e\_InAs}^*\right)^2 m_{e\_SL}^*\right)^{1/3} \tag{6-7}$$

$$m_h^* = \left(\left(m_{h\_GaSb}^*\right)^2 m_{h\_SL}^*\right)^{1/3} \tag{6-8}$$

6.2.3 Effect of a monovalent barrier on TPV diode performance

The pin and barrier device stacks are shown below in **Figure 6-7**. We note there that the point of the study is not to optimize the stack, but rather to investigate the effect of the barrier. As such auxiliary features that would normally boost efficiency, such as anti-reflective coatings or back surface reflectors, are not included in this study.

To start, we first simulate a pin diode with n-type emitter and p-type absorber doping levels of $n=1\times10^{17}/cm^3$ and $p=5\times10^{17}/cm^3$. For the pin structure, the intrinsic region is composed of the (10/13) InAs/GaSb superlattice material, which is not intentionally doped and, therefore, will have an intrinsic carrier concentration of $\sim1\times10^{16}/cm^3$ as calculated previously. In the barrier structure, the intrinsic region has been replaced by an InAs/AlSb superlattice material, which is also unintentionally doped. Due to the wider bandgap of this material, the intrinsic carrier population will be much lower, on the order of $\sim10^{12}/cm^3$. The band structures for the pin and barrier TPV diodes are plotted in **Figure 6-8**.

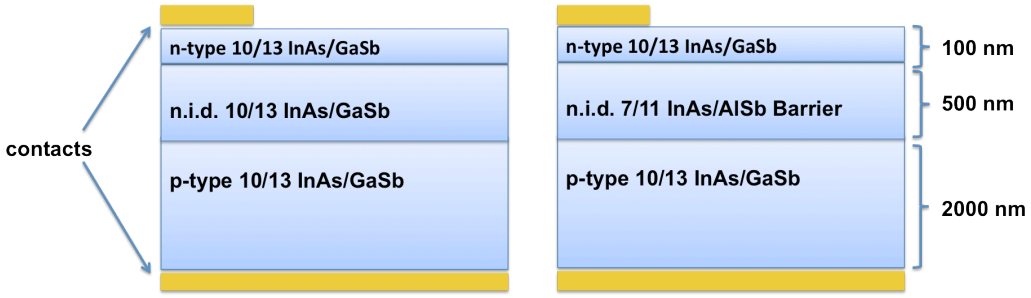

Figure 6-7: Device stack for the pin (left) and barrier (right) diodes.

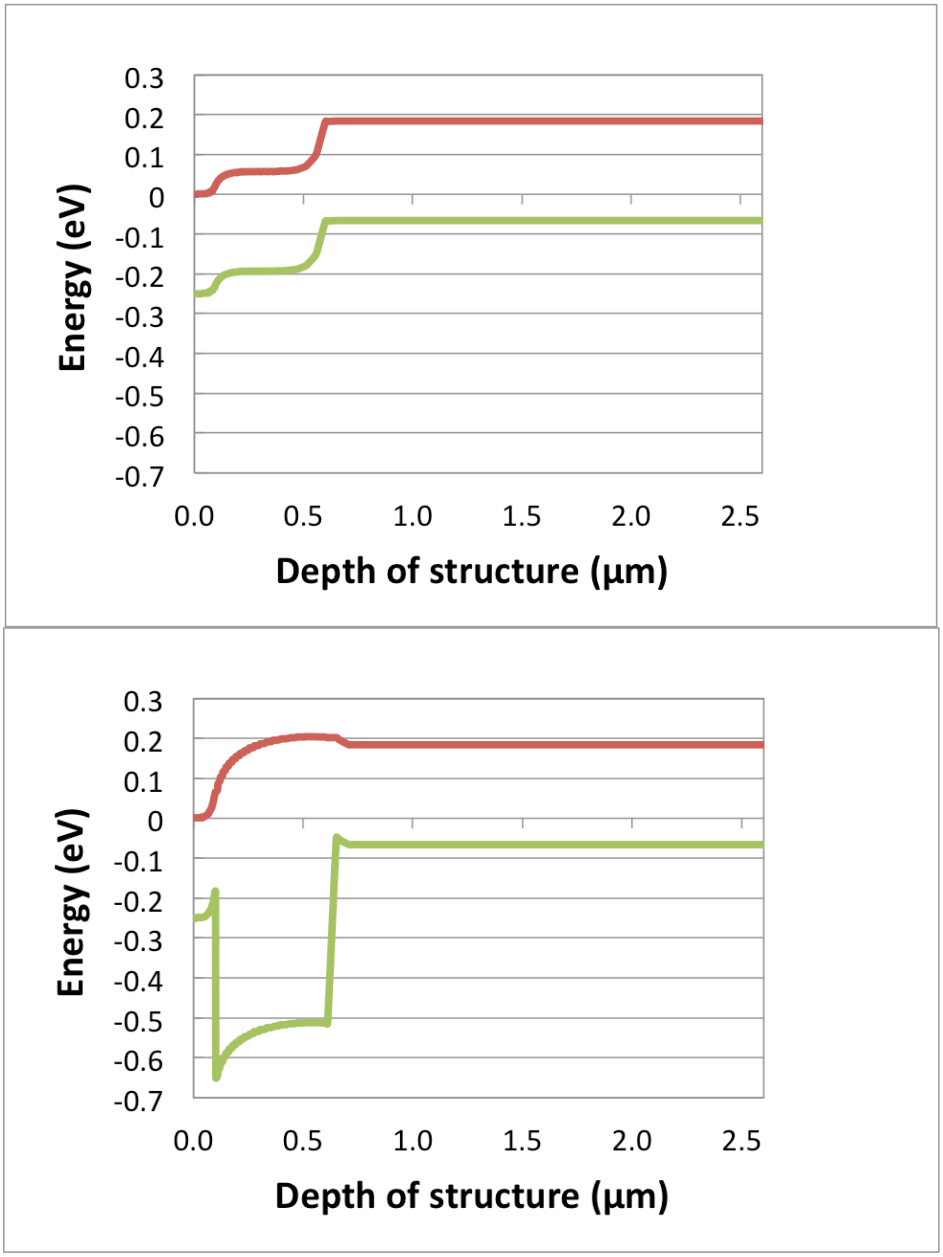

Figure 6-8: Band alignment for the pin (top) and barrier (bottom) diodes at zero bias. The conduction band is shown in red and the valence band is shown in green.

In **Figure 6-9**, we plot the simulated dark current density from these devices. We see that the barrier structure maintains a lower dark current for all voltages. Under illumination, the decrease in the dark current at forward bias will translate to an improvement in the open-circuit voltage. The IV characteristics for the pin and barrier

diodes under illumination are presented in **Table 6-2**. We note that the open-circuit voltage of the barrier diode has increased to more than twice that of the pin diode.

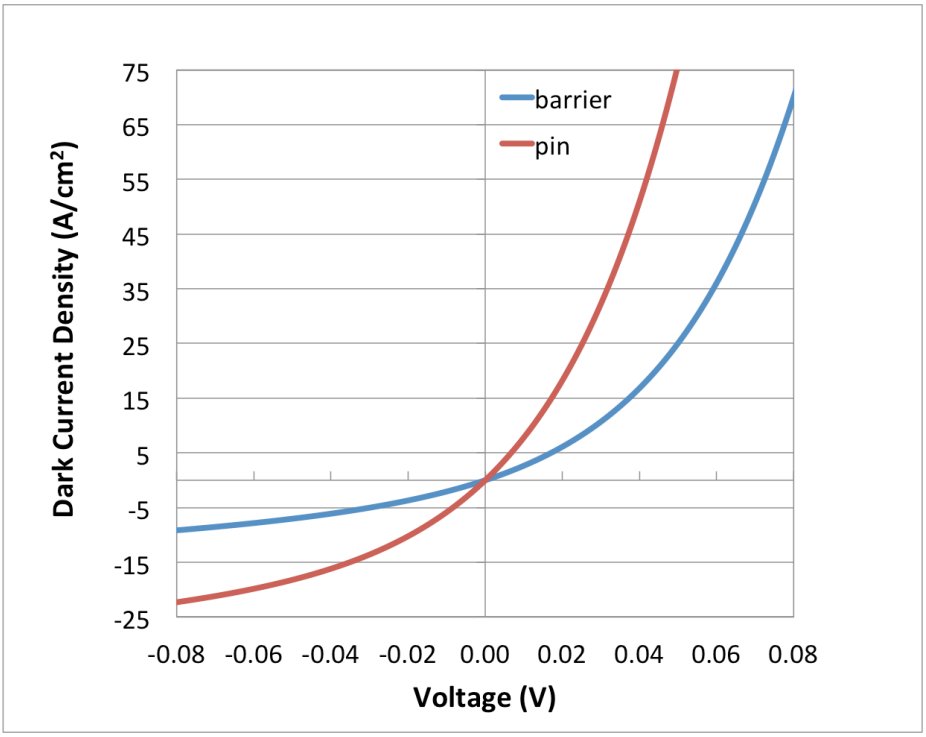

Figure 6-9: Simulated dark current density of the pin (red) and barrier (blue) structures at zero Kelvin.

	J_{SC} (A/cm^2)	V_{OC} (V)	P_{MAX} (W /cm^2)	FF	Efficiency (%)
PIN	4.093	0.006	0.6	25.87	0.038
BARRIER	4.164	0.014	1.6	27.17	0.104

Table 6-2: IV characteristics for the pin and barrier diodes under illumination by a 1000°C blackbody source. The short-circuit current (J_{SC}), open-circuit voltage (V_{OC}), maximum power density (P_{MAX}), fill factor (FF), and efficiency are reported.

While the barrier structure does yield a higher efficiency than the pin structure, the improvement is not as drastic as for photodetectors operating at lower temperatures. In considering why this may be the case, we return to the schematic of dark current as a function of temperature, Figure 6-10. In Section 2.1.5, we discussed how a diode will be GR-limited for low temperature operation and diffusion-limited for high temperature operation. Photodetector barrier structures operating at low temperatures have demonstrated reduced dark currents of several orders of magnitude, as the barrier *completely* eliminates SRH recombination which makes up the GR current, causing the diode to go from GR-limited to diffusion-limited (Chapter 2.1.5).

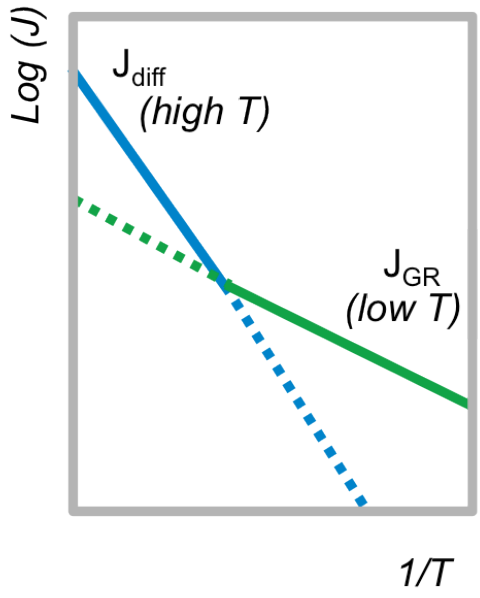

Figure 6-10: Arrhenius plot of the dark current mechanisms (diffusion and generation-recombination) versus temperature. Diffusion current is the dominant current for high temperature operation and generation-recombination current is the dominant current for low operation.

In the monovalent barrier example explored, only one of the carriers contributing to the diffusion current is blocked. Since the diffusion current is not completely eliminated, the decrease in dark current is not determined by the difference between the GR and diffusion currents, but by the ratio of the hole diffusion current to that of the electron diffusion current. This ratio is, in turn, dictated by the relative levels of doping in the n and p-type layers.

The product of the majority carriers (N_D for electrons in n-type and N_A for holes in p-type) and the minority carriers (p_n for holes in n-type and n_p for electrons in p-type) in each region will be equal to the intrinsic carrier concentration squared, Equations **6-9** and **6-10**. If the two doped regions consist of the same material, the intrinsic carrier concentrations will be equivalent, and we can equate the majority/minority carrier products, Equation **6-11**. We can then see that if the doping is higher in one layer, the minority carrier concentration in the other layer will be larger by the same factor. This means that for a device with a more highly doped p-layer than n-layer, there will be more minority carrier holes in the n-layer than minority carrier electrons in the p-layer, and it is the minority carrier holes that contribute the most to the dark current. We conclude that for the hole-blocking barrier to have the largest effect, the p-layer would have to be more highly doped than the n-layer. This can be seen in **Table 6-3** where the change in open-circuit voltage is given for various doping scenarios. Note that the barrier is most effective when the p-doping is greater than the n-doping. On the contrary, when the n-doping is higher, blocking the minority carrier holes does not have an effect. In fact, the overall efficiency is lower here, since the barrier has a lower short-circuit current than the pin, as the wider bandgap layer in the barrier absorbs less photons than the narrow bandgap layer in the pin.

$$p_n N_D = n_i^2 \quad \text{6-9}$$

$$n_p N_A = n_i^2 \quad \text{6-10}$$

$$p_n N_D = n_p N_A \quad \text{6-11}$$

Doping Relation	Absolute Δ V_{OC} (mV)	$V_{OC\ Barrier}/V_{OC\ pin}$	Relative Δ in Efficiency
$N_D > N_A$	+0	0x	-20%
$N_A = N_D$	+3	1.2x	+2%
$N_A > N_D$	+14	2.5x	173%

Table 6-3: Comparison of the effect of various doping ratios on the open-circuit voltage and efficiency. N_D is the doping in the n layer and N_A is the doping in the p layer.

From this study we determined that the success of the monovalent barrier structure over the pin structure is coupled to and limited by the doping levels, since the doping determines the balance of carriers within the device. A more effective approach would be to design a structure in which both holes and electrons that contribute to the diffusion-based dark current would be blocked. To accomplish this goal we propose the double-barrier structure, as shown in Figure 6-11. Here, a second barrier in the conduction band after the absorption region blocks electron carriers that would normally contribute to the dark current. By blocking both carriers that contribute to dark current, the dark current may be reduced from the diffusion current to that of the GR current. This could lead to a more substantial reduction in the overall dark current, which would enable operation of longer wavelength, narrow bandgap TPVs.

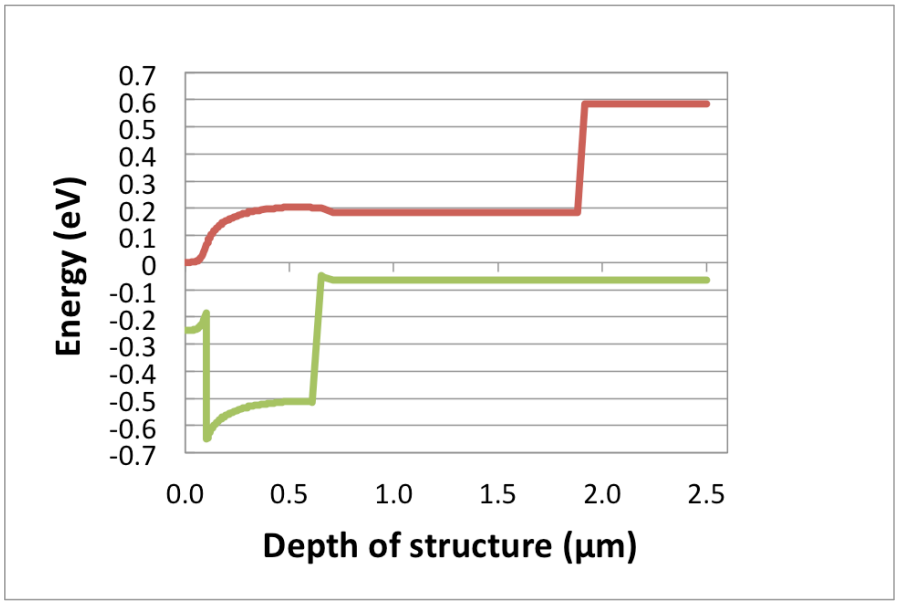

Figure 6-11: A double barrier structure – dark current electrons are blocked in addition to dark current holes. Note that the photo-generated carriers are not blocked by either of the barriers.

6.3 Device Performance

The superlattice pin and barrier structures were grown by MBE and processed into diodes by the fabrication methods outlined in Chapter 5, **Figure 6-12**. Dark current measurements were taken at room temperature and are plotted in **Figure 6-13**. From the pin to the barrier structure we see a decrease in dark current by 10 A/cm^2 at a bias of –200mV.

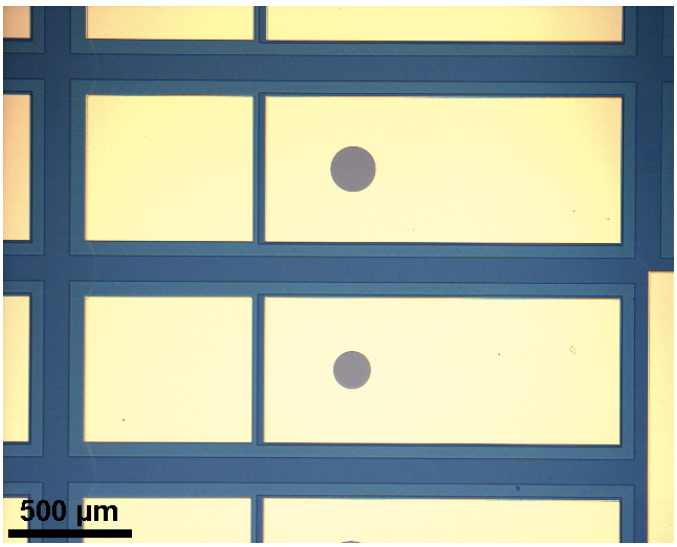

Figure 6-12: Microscope image of the InAs/GaSb diodes after contact deposition

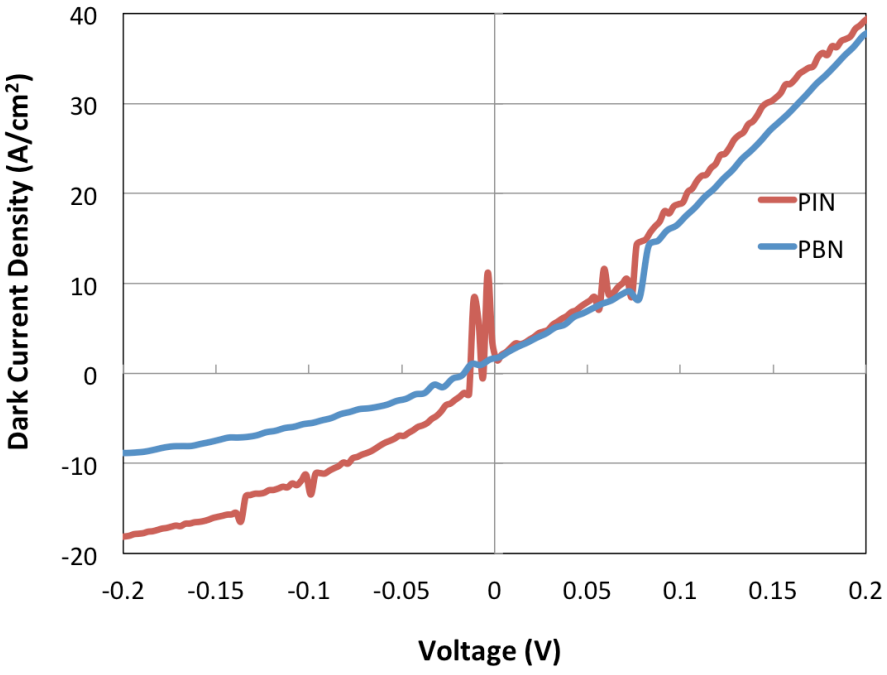

Figure 6-13: Dark current density of the pin (red) and barrier (blue) devices as measured at room temperature.

The diodes were then measured under AM0 illumination using the solar simulator. However, no measureable photocurrent under this illumination was achieved. This is to be expected for the given device architecture. Recall that the open-circuit voltage occurs when the photocurrent equals the dark current. Under illumination from the solar spectrum, the expected photogenerated current density will be on the order of milliamps per centimeter squared. Since dark current at room temperature is on the order of amps per centimeter squared, there will not be an observed difference in dark and light IV curves and the open circuit voltage will occur at zero volts. Testing under the intended blackbody conditions would yield higher current densities, lending a photocurrent of ~2.8 A/cm^2. However, since this value this is still close to that of the dark current value, the V_{OC} will still be extremely low – barely a few mVs. The expected short circuit current densities and open-circuit voltages are reported in Table 6-4.

	J_{SC} (A/cm^2)	V_{OC} (V)
PIN	2.785	0.003
BARRIER	2.829	0.004

Table 6-4:. The simulated short-circuit current (J_{SC}) and open-circuit voltage (V_{OC}) values under illumination by a 1000°C blackbody source for the structures that were grown and fabricated. Even with the higher current density from the blackbody spectrum, the dark current is still too high to yield any appreciable open-circuit voltage for room temperature operation.

The dark current will need to be reduced much more before the TPV diode can achieve any appreciable power at room temperature. One possible route is to use higher doping. Simulations with $N=1\times10^{18}/cm^3$ show an increase in V_{OC} up to 24mV when using the barrier structure. This voltage increase is estimated even when

including reduced mobilities that would result from these higher doping levels. These higher doped materials will need to be grown and characterized, however, to verify the expected dark current values.

6.4 Chapter Summary

TPV diodes typically have bandgaps in the energy range of 0.5–0.74 eV. For some time now it has been recognized that narrow bandgap diodes with longer cutoff wavelengths would both allow TPVs to absorb the present emitter source temperature more efficiently, and also allow recuperation of energy from lower temperature sources. However, getting narrow bandgap diodes to operate at elevated temperatures is non-trivial. As the bandgap of a device shrinks, the intrinsic carrier concentration and dark current increase. At room temperature, the dark current overwhelms the photogenerated current. As a result the open-circuit voltage goes to zero and there is no appreciable power generation. In order to establish narrow bandgap TPVs, alternative materials and device structures that can reduce the dark current are required.

In this chapter we investigated using a monovalent barrier to reduce the dark current in TPV devices. This method has proven effective in infrared photodetectors, which operate at low temperatures where the dominant dark current mechanism is generation-recombination. Here, we considered how a barrier structure would affect the performance of a TPV diode, which operates at higher temperatures where the diffusion current is the dominant mechanism.

We engineered the desired band alignment for a barrier structure using superlattice materials. We designed an InAs/GaSb superlattice absorber material with a

cutoff wavelength at 5 μm at room temperature. Growth of this material and subsequent characterization by photoluminescence measurements confirmed this cutoff wavelength. A barrier material was also designed from InAs/GaSb superlattice, but did not effectively form a wide bandgap material. We therefore re-designed the barrier material to include aluminum, which forms a wide bandgap material more readily.

We incorporated these materials into barrier and pin diode structures. To establish a fair comparison between the barrier and pin structures, we made the thickness of the barrier equal to the thickness of the intrinsic layer in the pin diode. We determined that tunneling through a barrier of this thickness would be negligible, and therefore all of the dark current from the hole carriers would be due to thermionic emission over the barrier.

We simulated the IV performance of the pin and barrier structures. We found that the monovalent barrier was effective at reducing the dark current and improving the open-circuit voltage, but only for certain doping ratios. Specifically, when the p-doping is greater than the n-doping, the dark current is dominated by hole carriers, and blocking the hole carriers leads to a reduction in the overall dark current. On the other hand, when the n-region is more heavily doped than the p-region, blocking the hole carriers has a negligible reduction of the overall dark current. From this study we concluded that the effect of a monovalent barrier is coupled to and limited by the doping levels. If a barrier could be used in both the conduction and valence bands, both carriers that contribute to the diffusion current could be blocked and and the dark current would be reduced to that of the GR current. The next step in this investigation is to calculate the possible reduction for a double-barrier device. If substantial, this could be a promising route for developing longer wavelength TPV diodes.

7 GaSb TPVs with Front Surface Photonic Crystals

In previous work, simulations and experiment showed that front-surface photonic crystals could be used to improve the absorption in GaSb [84][85]. However, GaSb diodes made for this study were poor-performing, with low open-circuit voltage and short-circuit current, Section 3.2 [49]. As such, the focus of research shifted to the GaSb diode. Here, we re-consider the diode design; we explore the possibility of adding an intrinsic region to take advantage of the altered absorption due to the photonic crystal pattern. We also consider routes toward ohmic contacts, which are critical to device operation.

7.1 GaSb pin diode

Doping in GaSb TPV diode structures is often achieved via diffusion methods. This method limits the design since the doping profile is fixed to the gradient formed by the diffusion method. An alternative method is to define the diode structure epitaxially. This method allows for a sharply defined junction and the formation of more advanced device architectures such as those that include back surface fields and front surface windows. The epitaxial method also uniquely allows for the introduction of an intrinsic region between the P and N regions. Adding an intrinsic region is a technique employed in various PV technologies to extend the electric field within the device, increasing collection of photogenerated carriers. This method could improve carrier collection in GaSb diodes with PhCs, where the shifted absorption profile due to the PhCs extends

well into the device. Here we explore the feasibility and effect of including an intrinsic region in GaSb TPV diodes.

The intrinsic carrier concentration for GaSb at room temperature is calculated to be $1.5\times10^{12}/cm^3$ [80], [103–105]. In practice, however, the carrier concentration is much higher - 10^{16} - $10^{17}/cm^3$ - due to native defects [103]. These defects arise from the low vapor pressure and surface mobility of antimony, which causes antimony atoms to cluster together, leaving anti-sites where antimony atoms would normally incorporate into the lattice [106]. The anti-site is unstable and the nearest gallium atom will fill the site, creating both a gallium-in-antimony site defect ("Ga_{Sb}") and a gallium vacancy defect ("V_{Ga}"). These defects limit the intrinsic carrier concentration in practice to a value much higher than the theoretical value.

With these limitations in mind, we study the effect of incorporating an intrinsic region into a GaSb TPV diode with a practical intrinsic level of $3\times10^{16}/cm^3$, which is what we have grown and measured experimentally; Note – a list of the dopant calibrations can be found in Appendix D. The N region is simulated with $n=2\times10^{18}/cm^3$; this value is the upper limit achieved in the literature, as it is challenging to form a high n-doping due to the p-type defects in GaSb. On the contrary, the P region is much easier to dope highly. Here we simulate the p-region to be $5\times10^{18}/cm^3$. While higher p-doping levels are possible, the carrier lifetime rapidly decrease with increasing doping, so the doping should not be made too high.

For the device structure, we use an n-on-p architecture because the minority carrier electrons in a p-type absorber have a much great mobility than the minority carrier holes in an n-type absorber. The top emitter n-layer is kept thin, 100 nm. The p-type absorber is simulated as several micrometers thick. The device stacks simulated

are shown in **Figure 7-1**. The thickness of the absorber in the PN diode is equal to the thickness of the intrinsic region plus the absorber in the pin structure.

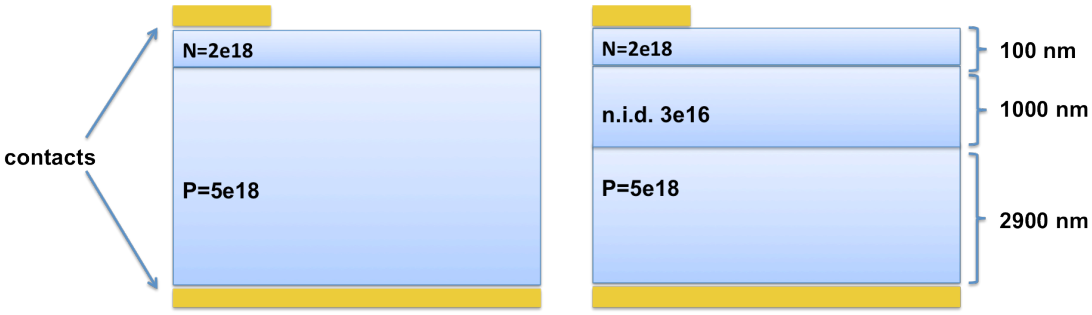

Figure 7-1: Device Stacks – (left) PN, (right) pin, simulated with an intrinsic doping level of $n=3\times10^{16}/cm^3$

In **Figure 7-2**, the electric field is plotted for the PN and pin structures. We see that the addition of the intrinsic region in the pin structure extends the electric field further into the device. This extension of the electric field will lead to an improvement in carrier collection and quantum efficiency of longer wavelength radiation, which is absorbed deeper in the device. This can be seen in a comparison of the quantum efficiencies of the different devices, **Figure 7-3**. For the pin device, there is a large increase in the QE at longer wavelengths, as much as 17% at 1.5 μm. We note that there is a decrease in QE at shorter wavelengths, since the magnitude of the electric field has decreased at the front of the diode. Overall, however, there are more net carriers absorbed, leading to an improvement in the current density from 0.7 to 0.9 A/cm^2 and an increase in power of 50 mW/cm^2, **Table 7-1**.

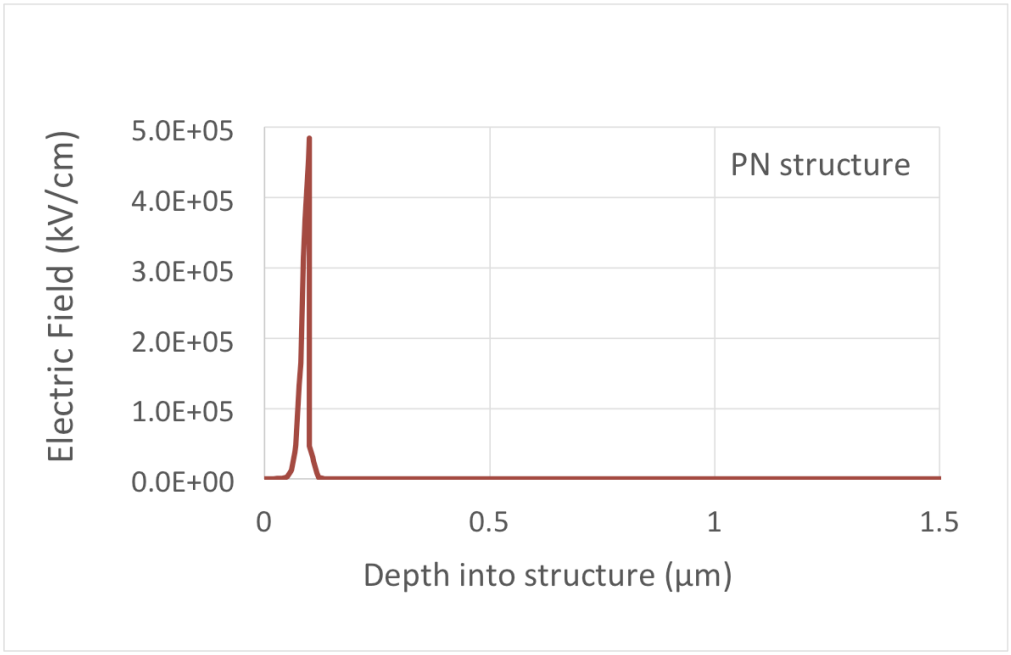

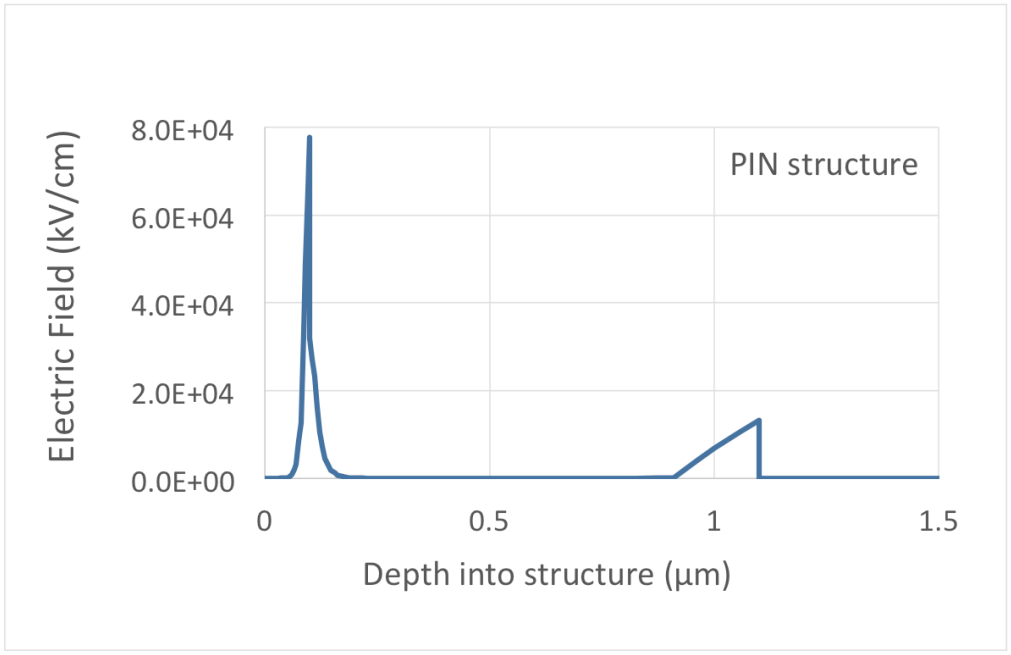

Figure 7-2: Electric field in the GaSb PN (top) and pin (bottom) diodes

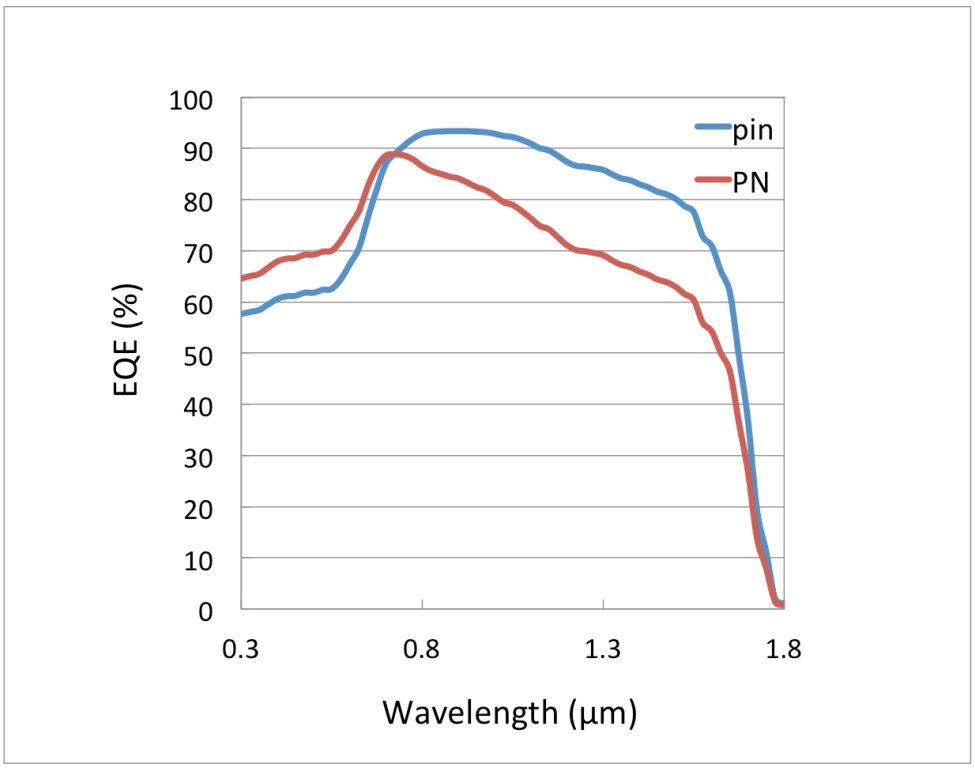

Figure 7-3: External quantum efficiency (EQE) of the GaSb pn and pin devices

	J_{SC} (A/cm^2)	V_{OC} (V)	P_{MAX} (mW /cm^2)	Efficiency (%)
PN	0.711	0.605	350	0.26
PIN	0.866	0.583	400	0.30

Table 7-1: Simulation of the power metrics for the PN and PIN didoes. The short-circuit (J_{SC}) current, open-circuit voltage (V_{OC}), maximum power (P_{MAX}), and efficiency are tabulated.

Considering these results, avenues to further decrease the background concentration in GaSb are worthy of investigation. Several methods have already been

explored [106], [107]. In one technique, the GaSb epilayer is grown on tilted substrates to encourage Sb-incorporation; this method has demonstrated background carrier concentrations on the order of $10^{15}/cm^3$ [106]. In another technique, Polyakov et al. achieved a low doping on the order of $10^{13}/cm^3$ by growing GaSb at higher temperatures than normal - 600-630°C as opposed to 500°C [107]. Given these promising results, the lower predicted background doping concentrations of ~ $10^{12}/cm^3$ could be attainable.

7.2 Ohmic contact/PhC layer

In our research, photonic crystals are incorporated on the front surface of the GaSb TPV diode not only to improve the absorption in the device, but also to act as a front contact. In our previous design, the contacts consisted of a material composition of titanium, platinum, and gold to both p-GaSb and n-GaSb [108]. However, this material composition does not readily form an ohmic contact to n-GaSb. Here, we discuss why this is the case and consider the options moving forward.

Recall from Section 2.1 that when a semiconductor and metal are brought into contact under equilibrium, the Fermi levels will align. For some semiconductor materials, including GaSb, the Fermi level is fixed at the surface independent of the metal it mates too and is therefore “pinned” [109]. In GaSb, the Fermi level is pinned near the valence band at the surface ([103], [109–111]). While pinning near the valence band facilitates contact to p-GaSb, it makes contact to n-GaSb extremely difficult. Upon alignment of the Fermi levels for a metal and n-GaSb, a large barrier will form, blocking carrier transport from the semiconductor to the metal. One method to overcome this unintentional barrier is to highly dope the material; high doping thins the depletion region at the metal-semiconductor interface so that carriers can tunnel through the barrier. As

mentioned previously, however, highly doped n-GaSb is difficult to achieve due to the intrinsic p-type defects in GaSb.

Because of the technological importance of antimonides, a significant amount of research has focused on developing ohmic contacts to n-GaSb [112–123]. Originally gold-based contact recipes were researched [114–118]. Gold-based contacts are not recommended for GaSb as the gold diffuses deep into the device [123]. Palladium-based contact recipes have been quite successful, with resistivity as low as ~10^{-6} Ω-cm^2 with annealing [119–122]. These Pd-based contacts are usually combined with another material like germanium to create a heavily doped layer beneath the contact. The contact recipes are then composed of several layers. For example one successful recipe consisted of Pd/Ge/Au/Pt/Au [120], where the first gold layer is to encourage diffusion of germanium into semiconductor. One concern with this method, however, is that the deposited contacts must be annealed in order to form an ohmic contact. Heating the device at high temperatures required for annealing can be detrimental as it may lead to further out-diffusion of antimony and degradation of the device structure. Another concern unique to our design is that the n-type contact material must also serve as the material for the PhC pattern. The effect of using these multi-layer stacks for PhCs would have to be studied via finite-difference time-domain simulations.

Rather than incorporating multi-layer metal compositions for the PhCs, an alternative solution is to introduce a contact layer (CL). The CL would be a thin layer of a material for which the Fermi level is pinned in a more ideal location. When inserted just beneath the contact, the CL facilitates formation of an ohmic contact to the top layer of the diode. This technique has been employed with other III-V materials; for example, InAs is frequently used as a CL with III-V materials because the surface Fermi level of

InAs is pinned above the conduction band, allowing for a low contact resistance. InAs cannot be used as a contact layer for GaSb diodes because of the band discontinuity between InAs and GaSb. This band alignment issue can be circumvented, however, if InAs is alloyed with Sb [124–126]. The alloy InAsSb is a good candidate for a CL for n-type GaSb as the Fermi level is pinned in the conduction band and the alloy can be highly doped. InAsSb lattice matched to GaSb has been explored as a CL, achieving specific resistivity as low as 5.1 x 10^{-6} Ω-cm^2 without annealing [125]. The quaternary alloy GaInAsSb has also been researched as a CL for GaSb: Huang et al. achieved a contact resistivity of 2 x 10^{-6} Ω-cm^2 by using GaInAsSb as a contact layer [126].

Looking forward, it appears the best solution to create an ohmic contact/PhC to n-GaSb for our n-on-p GaSb diode might be to incorporate a contact layer. A major advantage of using a CL is that it does not require annealing to achieve a low resistivity. Also, by using a CL, we can incorporate less complicated contact/PhC recipes. We could then investigate the performance of the GaSb diode using the original intended contact recipe of Ti/Pt/Au. This approach could be the best option continuing onward with our design.

7.3 Chapter Summary

In this chapter, we reconsidered the GaSb TPV diode design for our PhC project. We explored the feasibility and effect of adding an intrinsic region to the GaSb PN diode to take advantage of the altered absorption profile due to the PhC pattern. Experimentally we achieved an intrinsic carrier concentration of n=3×10^{16}/cm^3 for GaSb. We studied the effect of adding this intrinsic region to the device via simulations with the program Silvaco. The addition of this lower-doped region between the n and p regions

extended the electric field further into the device, allowing more photogenerated carriers to be collected. While the magnitude of the electric field at the front surface decreased, the overall absorption was higher, leading to an improvement in the current density from 0.7 to 0.9 A/cm^2 and an increase in the power generated of 50 mW/cm^2. These simulated results are for a pin device with a practical intrinsic carrier concentration of 3×10^{16}/cm^3. If the background doping can be further reduced to ~10^{12}/cm^3, the power characteristics could potentially be improved further.

In addition to studying the GaSb pin diode structure, we also considered the various methods for achieving an ohmic contact to n-GaSb. For GaSb, an ohmic n-type contact is notoriously difficult to form because of Fermi level pinning near the valence band. This pinning creates an unintended potential barrier when the n-GaSb material is mated to the metal contact, blocking current from the semiconductor. As such, there has been a significant research effort to develop an improved ohmic contact to n-type GaSb. Annealed palladium-based contacts have produced some of the lowest resistivities thus far. However, these multi-layer structures which must be annealed may not be the best solution for our specific design, where the front-surface contact also serves as the PhC. A better solution may be to use a highly doped contact layer such as InAsSb or GaInAsSb between the metal contacts and the n-GaSb semiconductor. The use of a contact layer would allow for more flexibility in metal choice for the PhC/front contact design.

Moving forward with the project, we have grown and characterized several doping calibrations for GaSb and the measured doping levels are reported in Appendix E. Further work is required to investigate exactly what the achievable limits are for doping of GaSb with our MBE system. For example, what is the highest n-doping possible while

maintaining a smooth surface morphology? Can we achieve a lower intrinsic carrier concentration than the present value? The answers to these questions will dictate what diode structures are possible. In addition to further GaSb doping calibrations, contact layer alloys should be grown and subsequently tested with contact recipes to develop an ohmic contact to n-GaSb. Once the contact layer has been determined, the PhCs can be deposited for full device integration. We have been developing the PhC recipe in parallel with the GaSb growths and the PhC recipe is detailed in Appendix F.

Appendix A – Growth Details

GaSb grown on the GenXplor @ TECF

- *Substrates:*
  - Doping calibrations made of ¼ wafer of SI GaAs
  - Full pin devicea grown on GaSb p-type wafers
- *Source ramping:*
  - Gallium bulk/tip = 400/550 → 890/990 at 15C/min
  - Antimony bulk/cond/cracker =200/790/900, bulk ramped to 525C at 5C/min
  - GaTe ramped from 200C at 10C/min
- *GaSb Deox:*
  - Substrate ramped to 560C at 30C/min
  - At Tsub=350C, Sb shutter opened
  - Ramp to tsub=590C at 10C/min
  - Tsub=592C, tpyro=557 spots observed indicating deox
  - 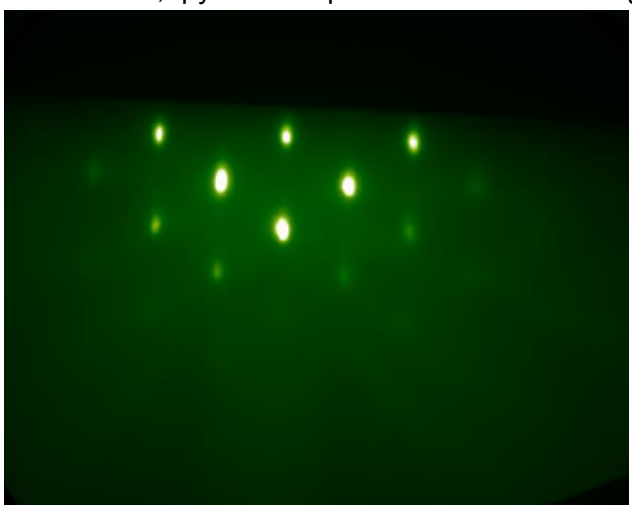
  - Temperature brought up 10 degrees and held for 15 minutes
  - Tsub=600C, tpyro=557
- *Growth:*
  - Drop to tpyro = 510 C (tsub = 547C)
  - Gallium opened, growth commences

- 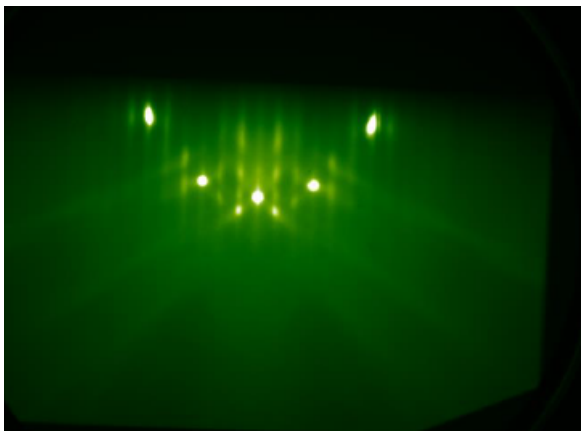
- 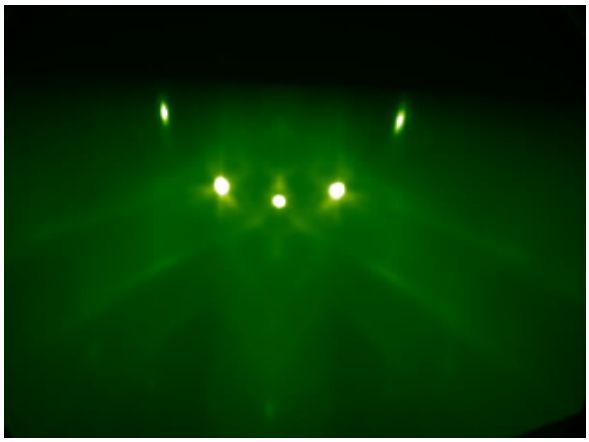
- *Cooling down of cells:*
  - Substrate cooled to 200C at 50C/min
  - Te cooled to 200C at 10C/min
  - Be cooled to 200C at 10C/min
  - Ga cooling: tip/base cooled to 650/400C at 10C and 20C/min to keep tip hotter than bulk, cool to 500/400C after
  - Sb bulk cooling after sample is bellow 400C, bulk cooled to 200C at 5C/min, when substrate reaches 375C, close Sb valve and shutter

InAs/GaSb superlattice growth on the Compact 21 @ NanoMIR

- Cell temperatures:
    - p-type InAs/GaSb: Be @800
    - N-type InAs/GaSb: Te@240
    - In: 777/827
    - Ga:820/920
    - Sb:535/900
    - As:380/925
- Heat sample from 200C to 500C, first at 15deg/min, then at 8deg/min
- Rest here 20 minutes to remove the oxide
- Decrease to 470C for the buffer growth
- Set whole time to 9 minutes, set “duration” to 7, will rest at 2 minutes after
- Grow buffer for 15 min
- Superlattice period:
    - As (2sec)
    - InAs (21sec)
    - Sb (4sec)
    - GaSb (8sec)
- End loop with close Ga
- Cap with InAs

Appendix B – Diode Processing Procedure

0) **O_2 Plasma clean**
   - RIE-5 O_2 Plasma (10 min., ~20sccm, 75W, 254mTorr)

1) **Etch to bottom of diode** – (include extra sample to sacrifice to get etch rate) Here we are etching down to the p-contact layer, so the amount etched away should be equal to the device thickness (for most recent devices, 1900nm gets you to p-type buffer)

Spin Coating:
- Setup:
  i. PPE: gloves + Face shield
  ii. Line spinner head with foil
  iii. Clean chuck w/ acetone + IPA. Chuck goes on with flat side aligned
- Load spin settings recipe 2 (**3,000 RPM** for **45s**) (will leave ~2.5-3um thick resist layer for S1822)
  i. To check recipe: select recipe #, step #, "Step terminate" = time
  ii. First step in program should be an initial 5 second spin at 500 rpm
  iii. Ramp at a rate of 1000 rpm/sec to final speed
  iv. Final speed maintained for **45** seconds
  v. Spinner ramps down at 1000 rpm/sec
- Loading and cleaning
  i. blow off particles w/ N_2 → load → spin w/ Acetone then IPA during first 5sec
- Spin positive-photoresist **S1822**
  i. photoresist **S1822** (< 20mL in a cup at a time)
  ii. Use pipet to dispense enough photoresist to cover 2/3 of the surface
  iii. Start spinner with footswitch. Press switch again immediately to skip the 5 second initial spin.
  iv. Examine resist film for defects: if too many defects, dynamic clean to remove resist and re-spin
- Bake @ 115 °C for 75 seconds
- Let sample cool
- Clean up:
  i. Unused resist goes down resist-drain
  ii. Used foil + cups go in trash
  iii. Clean spinner head w/ acetone
  iv. Clean mask with IPA and N2 to prep for MJB4

MJB4:

- Log in to tool
- Setup:
    i. Standard mask holder 4" (if doing 5, must switch out)
    ii. Mask goes in chrome (darker side) face down
    iii. Hold down "mask vacuum off" to turn vacuum on
    iv. Put vacuum ring on chuck and load chuck
- Determine the h-line (405nm) dose:
    i. Select an exposure time to give an H-line dose between ~170 mJ/cm^2
- Set Parameters:
    i. Align + Expose
    ii. Soft contact
    iii. Set exposure time
- Set x and y stage knobs to 10 to give full range
- Load and sample and do WEC to calibrate stage for thickness of sample
    i. Pre-WEC turn down → Settings → WEC → Contact level up → CCW until msg
- Contact lever back up
- To move the mask on the sample, pull out of immediate contact
- Align sample with mask
    i. Note: can switch optics to do left/right/split field for alignment
- After aligning, bring back into close contact
- Exposure → yes
    i. Expose resist with **Mask 1**
- Demounting:
    i. Open contact lever and unload substrate
    ii. Take out mask with vacuum off
- Clean mask

Develop:

- Correct PPE: Two pairs of chemical gloves (use special gloves) & white apron (found with stock items in acid bay), face shield
- Develop in MFCD26 (60s) *without moving sample* (make sure no cloudy areas left)
- Rinse with DI (30s)
- Rinse tweezers
- Dry with N_2
- Unused developer goes down sink in developer hood

Etch III-V with **RIE-7** to get to bottom contact:

- Log in
- First etch dummy to get etch rate:
    i. Glue + Load sample (via heating and oil paste), pump down

1. Use oil provided to glue sample to Si wafer. Only one drop necessary

ii. Run Vandervelde_O2PlasmaClean (10min) recipe (cleans reactor)
- Check that parameters are correct
- Give a random job ID #
- Start recipe, adjust Helium know so that >10mTorr (CW increases)
- Note: we ran this recipe "process in empty chamber" last time
- O2 plasma clean recipe:
  - 45 sccm O2, 20mT Pressure, 800W ICPRF DC bias ~50V, 20W

iii. Run Vandervelde Etch recipe (5m) without samples to pre-condition chamber
1. Vandervelde "GaAs" Etch Recipe:
   - BCl3/Ar/N2: 20/10/5sccm
   - RF: Bias: 100W, DC bias, 262V
   - ICP: Set 500W
   - Pressure setpoint: 2.5mT

iv. Run Vandervelde recipe to etch dummy sample
v. Watch and record reflected power
vi. Unload sample + unglue (via re-heating)
vii. Rinse with IPA and dry with N_2
viii. Remove resist with Acetone/IPA/N_2
ix. Optical microscope to check that all resist is removed
x. Measure etched depth with Dektak (log-in) + calculate etch rate

- Etch real samples (can etch several simultaneously)
- Measure in Dektak (must log-in) – if short, go back and re-spin resist…etc.
  - We ran this for 5 minutes, etched 3,675 nm of GaSb → 735 nm/ min, 12.25nm/ second

2) **Si_3N_4 layer deposition -** isolation layer to protect the etched sidewalls and isolate contacts (note: pattern will be ~20um wide) In this first step we are covering the entire sample with Si_3N_4

Deposit Si_3N_4 with **CVD-3** (note: CVD only available 6am-10pm M-F)
- Vent, load sample, pump, select recipe, check recipe time + gases, apply
- Run HFSiN recipe on one sample for 10 minutes (should yield ~110nm)
  i. Auto → start → next → start
- Monitor and record reflected power
- After running samples, do an etch-back recipe on chamber (5mim for every um deposited, minimum time of 5 minutes)

HFSiN Recipe:

- SiH4 = 35 sccm
- NH3 = 55 sccm
- N2 = 1960 sccm
- Pressure = 900 mTorr
- Power = 20 W HF
- T lower electrode = 300C
- Tupper electrode = 250C
- Nominally deposits 12.3nm/minute

3) **Pattern Si_3N_4 to prepare for etch**

Spin Coating:

- Setup:
    i. PPE: gloves + Face shield
    ii. Line spinner head with foil
    iii. Clean chuck w/ acetone + IPA. Chuck goes on with flat side aligned
- Load spin settings recipe 2 (**3,000 RPM** for **45s**) (will leave ~2.5-3um thick resist layer for S1822)
    i. To check recipe: select recipe #, step #, "Step terminate" = time
    ii. First step in program should be an initial 5 second spin at 500 rpm
    iii. Ramp at a rate of 1000 rpm/sec to final speed
    iv. Final speed maintained for **45** seconds
    v. Spinner ramps down at 1000 rpm/sec
- Loading and cleaning
    i. blow off particles w/ N_2 → load → spin w/ Acetone then IPA during first 5sec
- Spin positive-photoresist **S1822**
    i. photoresist **S1822** (< 20mL in a cup at a time)
    ii. Use pipet to dispense enough photoresist to cover 2/3 of the surface
    iii. Start spinner with footswitch. Press switch again immediately to skip the 5 second initial spin.
    iv. Examine resist film for defects: if too many defects, dynamic clean to remove resist and re-spin
- Bake @ 115 °C for 75 seconds
- Let sample cool
- Clean up:
    i. Unused resist goes down resist-drain
    ii. Used foil + cups go in trash
    iii. Clean spinner head w/ acetone
    iv. Clean mask with IPA and N2 to prep for MJB4

3) Pattern Si_3N_4 to prepare for etch (cont.)

MJB4:

- Log in to tool
- Setup:
    i. Standard mask holder 4" (if doing 5, must switch out)
    ii. Mask goes in chrome (darker side) face down
    iii. Hold down "mask vacuum off" to turn vacuum on
    iv. Put vacuum ring on chuck and load chuck
- Determine the h-line (405nm) dose:
    i. Select an exposure time to give an H-line dose between ~175 mJ/cm^2
- Set Parameters:
    i. Align + Expose
    ii. Soft contact
    iii. Set exposure time
- Set x and y stage knobs to 10 to give full range
- Load and sample and do WEC to calibrate stage for thickness of sample
    i. Pre-WEC turn down → Settings → WEC → Contact level up → CCW until msg
- Contact lever back up
- To move the mask on the sample, pull out of immediate contact
- Align sample with mask
    i. Note: can switch optics to do left/right/split field for alignment
- After aligning, bring back into close contact
- Exposure → yes
    i. Expose resist with **Mask 2**
- Demounting:
    i. Open contact lever and unload substrate
    ii. Take out mask with vacuum off
- Clean mask

Develop:

- Correct PPE: Two pairs of chemical gloves (use special gloves) & white apron (found with stock items in acid bay), face shield
- Develop in MFCD26 (60s) *without moving sample* (make sure no cloudy areas left)
- Rinse with DI (30s)
- Rinse tweezers
- Dry with N_2
- Unused developer goes down sink in developer hood

4) Si_3N_4 RIE-8 ETCH

- Can glue samples to 6" quartz (clear) wafer holder
- Run o2plasma clean for 20 minutes first, then run personal recipe for 5 minutes to pre-condition the chamber
- Automatic → choose recipe → check recipe → start
- Can use manual to check conditions
- "standard mat process" is the place to change the recipe
- Automatic to go back
- Run with our sample:
  - glue on with a drip of oil
  - Vandervelde_SiN_Etch = SF_6 (12 sccm), O_2 (6 sccm), 1 min for ~110nm
  - Other recommendation: 10sccm C_4F_8, 10sccm SF_6.
- Measure under dektak to see etched depth of SiN
- Acetone and IPA rinse to remove resist

5) Pattern for Metallic Contact Deposition – need to use LOR here to do a bi layer

Spin Coating:

- Setup:
  i. PPE: gloves + Face shield
  ii. Line spinner head with foil
  iii. Clean chuck w/ acetone + IPA. Chuck goes on with flat side aligned
  iv. To check recipe: select recipe #, step #, "Step terminate" = time
- Dehydration bake: 2min @180C
- Loading and cleaning
  i. blow off particles w/ N_2 → load → spin w/ Acetone then IPA during first 5sec
- Dehydration bake: immediately before applying resist, removed water by baking at >150C for at least one minute
- Note: the LOR thickness needs to be greater than the thickness of the metal to be lifted off: good rule of thumb is the LOR layer should be 1.5X thicker than intended metal thickness. So far 50/50/350 ti/pt/au, =450 contact. This means lor should be at least 675nm thick. LOR3A only gets to 600nm max **Lor 20B gives 2,000nm @4k**
- Spin resist
  i. **LOR 20B** @ 4kRPM for 45s, bake @180°C for 4 minutes;
    1. **Examine for defects: if unacceptable: resist can be removed by soaking in Remover-PG for 15 minutes at 80C. Acetone will *not* remove LOR resist.**
  ii. **S1805 @4kRPM recipe 45s,** bake @115C for 60s
    1. Again, if defects, musk soak in R-PG!

- Clean up:
    i. Unused resist goes down resist-drain
    ii. Used foil + cups go in trash
    iii. Clean spinner head w/ acetone
    iv. Clean mask with IPA and N2 to prep for MJB4

MJB4:

- Log in to tool
- Setup:
    i. Standard mask holder 4" (if doing 5, must switch out)
    ii. Mask goes in chrome (darker side) face down
    iii. Hold down "mask vacuum off" to turn vacuum on
    iv. Put vacuum ring on chuck and load chuck
- Determine the h-line (405nm) dose:
    i. Select an exposure time to give an H-line dose between ~50 mJ/cm^2
- Set Parameters:
    i. Align + Expose
    ii. Soft contact
    iii. Set exposure time
- Set x and y stage knobs to 10 to give full range
- Load and sample and do WEC to calibrate stage for thickness of sample
    i. Pre-WEC turn down → Settings → WEC → Contact level up → CCW until msg
- Contact lever back up
- To move the mask on the sample, pull out of immediate contact
- Align sample with mask
    i. Note: can switch optics to do left/right/split field for alignment
- After aligning, bring back into close contact
- Exposure → yes
    i. Expose resist with **Mask 4**
- Demounting:
    i. Open contact lever and unload substrate
    ii. Take out mask with vacuum off
- Clean mask

Develop:

- Correct PPE: Two pairs of chemical gloves (use special gloves) & white apron (found with stock items in acid bay), face shield
- Develop in MFCD26 (60s) *without moving sample* (make sure no cloudy areas left)
- Rinse with DI (75s)
- Rinse tweezers
- Dry with N_2
- Unused developer goes down sink in developer hood

EXTRA CLEAN REQUIRED PRE-METAL DEP**

- O2 plasma de-scum(75W, 20s, 40sccm O_2)
- Pre-deposition acid clean
    i. HCl:DI water (1:1) for 1min
    ii. → DI water (~30s)

6) Contact Deposition

CONTACT DEP

- Deposit ohmic contact (use base pressure of 2-5e-6 Torr or better)
- Ti (20 nm)/Au (200 nm)

LIFTOFF RESIST

- Soak in Remover-PG @80°C for 10s of minutes to a few hours
- To speed up liftoff, sonicate after sitting in remover PG for several minutes
- Remove the substrate from the Remover-PG, and rinse with isopropanol, then blow dry with nitrogen

7) ARC COATING

Steps 2-4, but with Mask 5

Appendix C – Density of States Calculation for a Superlattice Structure

The density of electronic states, as described in Chapter 2.1, is the number of states at a particular energy level that electrons are allowed to occupy, or *the number of state per unit volume per unit energy.* The density of states (DOS) is of interest because it influences several key material properties, including absorption and intrinsic carrier concentration. For many bulk semiconductor materials, the DOS is well approximated by Equations **2-3** and **2-4**. For a superlattice material, however, the DOS cannot be calculated by these equations, which assume the same dispersion along each primary axis. Here we detail a method for calculating the DOS that could be used for superlattice materials.

We start with the number of states per unit volume. The number of states can be calculated by diving a given volume by the smallest volume that can hold a single state, which when accounting for spin is $2 / (2\pi)^3$.

$$N(E) = \frac{V_{k_{space}}(E)}{4\pi^3} \qquad \text{C-1}$$

/unit energy gives the DOS:

$$\rho_{DOS}(E) = \frac{N(E)}{dE} = \frac{V_{k_{space}}(E)}{4\pi^3\, dE} \qquad \text{C-2}$$

Then we solve for the volume of k-space allowed for a given energy interval dE, or the volume of space enclosed between two energy contours corresponding to E and E= E+dE. That volume is given by the following surface integral:

$$V_{k_{space}}(E) = dE \int_{Surface} \frac{ds}{\nabla_k E(k)} \qquad \text{C-3}$$

Where

$$\nabla_k E(k) = \left(\frac{\partial E}{\partial k_x}, \frac{\partial E}{\partial k_y}, \frac{\partial E}{\partial k_z}\right) \quad \text{C-4}$$

Making this substitution:

$$\rho_{DOS}(E) = \frac{1}{4\pi^3}\int_{Surface} \frac{ds}{\nabla_k E(k)} \quad \text{C-5}$$

The direction of k is the same as the surface-normal vector ds over the surface we are integrating over. Then, the integration over the surface equals:

$$\int_{Surface} \frac{ds}{\nabla_k E(k)} = \frac{1}{|\nabla_k E(k)|} SA \quad \text{C-6}$$

Making this substitution, the DOS now equals:

$$\rho_{DOS}(E) = \frac{1}{4\pi^3}\frac{1}{|\nabla_k E(k)|} SA \quad \text{C-7}$$

The gradient can be re-written in terms of steps in energy:

$$\frac{1}{|\nabla_k E(k)|} = \frac{1}{\left(\frac{\partial E}{\partial k_x}, \frac{\partial E}{\partial k_y}, \frac{\partial E}{\partial k_z}\right)} = \left(\frac{\partial k}{\partial E_x}, \frac{\partial k}{\partial E_y}, \frac{\partial k}{\partial E_z}\right) = \nabla_E k(E) \quad \text{C-8}$$

Moreover,

$$|\nabla_E k(E)| = \sqrt{\frac{\partial k^2}{\partial E_x} + \frac{\partial k^2}{\partial E_y} + \frac{\partial k^2}{\partial E_z}} \quad \text{C-9}$$

Then the density of states can be written as follows:

$$\rho_{DOS}(E) = \frac{1}{4\pi^3}\sqrt{\frac{\partial k^2}{\partial E_x} + \frac{\partial k^2}{\partial E_y} + \frac{\partial k^2}{\partial E_z}}SA \qquad \text{C-10}$$

For a superlattice material, the dispersion will be the same in the plane, but differ in the growth direction. The density of states can then be written as:

$$\rho_{DOS}(E) = \frac{1}{4\pi^3}\sqrt{\frac{\partial {k_{SL}}^2}{\partial E_x} + 2\frac{\partial {k_{XY}}^2}{\partial E_y}}SA \qquad \text{C-11}$$

The energy contour is described by an oblate spheroid, **Figure C-0-1**. Substituting in this geometry for SA, the final equation is then given by Equations **C-12** and **C-13**.

$$\rho_{DOS}(E) = \frac{1}{4\pi^3}\sqrt{\frac{\partial {k_{SL}}^2}{\partial E_x} + 2\frac{\partial {k_{XY}}^2}{\partial E_y}}\left(2\pi {k_{XY}}^2 + \pi\frac{{k_{SL}}^2}{e}ln\left(\frac{1+e}{1-e}\right)\right) \qquad \text{C-12}$$

$$e \equiv \sqrt{\left(1 - \frac{{k_{SL}}^2}{{k_{XY}}^2}\right)} \qquad \text{C-13}$$

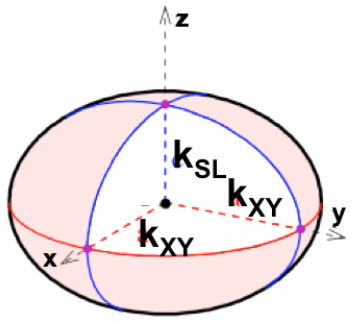

Figure C-0-1: Energy contour for the density of states calculation for a superlattice material.

Appendix D – GaSb Hall Data

The doping levels for n-type and p-type GaSb doping calibrations as measured via Hall are tabulated in **Table D-1**. Here GaSb samples were grown on semi-insulated (SI) GaAs substrates due to the issue of lack of SI GaSb substrates. While the 7% lattice mismatch between GaSb and GaAs leads to surface roughening and defects, the doping level measurements from these samples are still accurate, as demonstrated by Noh *et al.* [127].

Dopant	Dopant Cell Temperature (°C)	Doping Level (/cm^3)
Beryllium	950	P = 9.5e20
	850	P = 5.1e18
n.i.d.	-	P = 3.1e16
Tellurium	550	N = 2.2e16
	575	N = 1.9e17
	600	N = 9.0e17

Table D-1: Hall Data for GaSb Doping Calibrations

Appendix F – Photonic Crystal Processing Recipe

E-Beam lithography

- Clean
  - Minimum dynamic clean: – Acetone, IPA, spin dry
  - Preferred is 5min acetone sonication, IPA rinse, blow dry
- Spin PMMA C6 – 2000 RPM – 45 sec – 10 min bake at 180C
- Exposure dose – With contact pad 440 μC/cm2 @30kV, 30μm aperture
  - 200 μC/cm^2 @ 10kV, 30μm aperture
  - 100 μC/cm^2 @ 5kV, 30μm aperture
- PhC recipe should be ~100-200um larger then aperture to be covered

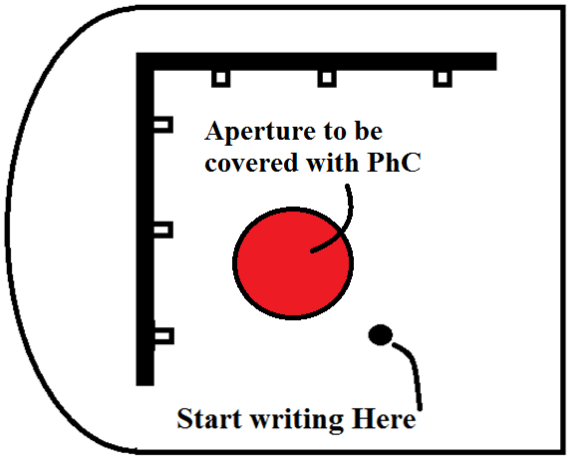

- Paint corner of chip with conductive paste, and perform align write field to the shapes on the paste
- Development – MIBK (3:1) Developer – 65 sec
  –IPA – 30 sec
  –N_2 Air gun dry

Contact Deposition
(Denton or Sharon E-Beam-want base pressure of at least 2e-6)

- Paint S1813 resist on chip prior to deposition – do not cover pattern!
- Ti/Pt/Au 50/50/250
  - The taller the better, but liftoff difficulty increases with height
- Immediate lift-off recommended in Acetone
- Sonication will be needed.

REFERENCES

[1] L. M. Fraas and J. Strauch, “DESIGN AND THERMAL MODELING OF A PORTABLE FUEL FIRED CYLINDRICAL TPV,” in *TPV-9*, 2010, pp. 2–7.

[2] B. Bernd, D. Wilhelm, and H. Reto, “Thermophotovoltaics on the move to applications,” *Applied Energy*, vol. 105, pp. 430–438, 2013.

[3] W. M. Yang, S. K. Chou, and J. Li, “Microthermophotovoltaic power generator with high power density,” *Applied Thermal Engineering*, vol. 29, no. 14–15, pp. 3144–3148, Oct. 2009.

[4] S. K. Chou, W. M. Yang, K. J. Chua, J. Li, and K. L. Zhang, “Development of micro power generators – A review,” vol. 88, pp. 1–16, 2011.

[5] W. M. Yang, S. K. Chou, C. Shu, Z. W. Li, and H. Xue, “A prototype microthermophotovoltaic power generator,” *Applied Physics Letters*, vol. 84, no. 19, p. 3864, 2004.

[6] W. E. Horne, M. D. Morgan, V. S. Sundaram, and T. Butcher, “500 Watt Diesel Fueled TPV Portable Power Supply,” *AIP Conference Proceedings*, vol. 653, no. 1, pp. 91–100, 2003.

[7] O. M. Nielsen, L. R. Arana, C. D. Baertsch, K. F. Jensen, and M. a. Schmidt, “A thermophotovoltaic micro-generator for portable power applications,” *TRANSDUCERS ’03. 12th International Conference on Solid-State Sensors, Actuators and Microsystems. Digest of Technical Papers (Cat. No.03TH8664)*, vol. 1, pp. 714–717, 2003.

[8] A. Schock, M. Mukunda, C. Or, and G. Summers, “Design, analysis, and optimization of a radioisotope thermophotovoltaic (RTPV) generator, and its applicability to an illustrative space mission,” *Acta Astronautica*, vol. 37, pp. 21–57, Oct. 1995.

[9] V. L. Teofilo, P. Choong, J. Chang, Y.-L. Tseng, and S. Ermer, “Thermophotovoltaic Energy Conversion for Space,” *Journal of Physical Chemistry C*, vol. 112, no. 21, pp. 7841–7845, May 2008.

[10] A. C. Thekdi, “Industrial Waste Heat Recovery : Potential Applications , Available Technologies and Crosscutting R & D Opportunities,” 2014.

[11] B. Wernsman, R. R. Siergiej, S. D. Link, R. G. Mahorter, M. N. Palmisiano, R. J. Wehrer, R. W. Schultz, G. P. Schmuck, R. L. Messham, S. Murray, C. S. Murray, F. Newman, D. Taylor, D. M. DePoy, and T. Rahmlow, *Greater than 20% radiant heat conversion efficiency of a thermophotovoltaic radiator/module system using reflective spectral control*, vol. 51, no. 3. 2004, pp. 512–515.

[12] E. Kittl, “Unique correlations between blackbody radiation and optimum energy gap for a photovoltaic conversion device,” in *10th IEEE Photovoltaic Specialist Conference*, 1974, pp. 103–106.

[13] A. Datas, “Optimum semiconducotr bandgaps in single junction and multijunction thermophotvoltaic converters,” *Solar Energy Materials and Solar Cells*, vol. 134, pp. 275–290, 2015.

[14] “http://www.sun.org/encyclopedia/black-body-radiation.” .

[15] “J. Y. Wah, PhD Thesis, University of Essex (2003).”

[16] M. W. Dashiell, J. F. Beausang, H. Ehsani, G. J. Nichols, D. M. Depoy, L. R. Danielson, P. Talamo, K. D. Rahner, E. J. Brown, S. R. Burger, P. M. Fourspring, W. F. TopperJr., P. F. Baldasaro, C. a. Wang, R. K. Huang, M. K. Connors, G. W. Turner, Z. a. Shellenbarger, G. Taylor, J. Li, R. Martinelli, D. Donetski, S. Anikeev, G. L. Belenky, and S. Luryi, “Quaternary InGaAsSb Thermophotovoltaic Diodes,” *IEEE Transactions on Electron Devices*, vol. 53, no. 12, pp. 2879–2891, Dec. 2006.

[17] H. Mohseni, V. Litvinov, and M. Razeghi, “Interface-induced suppression of the Auger recombination in type-II InAs/GaSb superlattices,” *Physical Review B*, vol. 58, no. 23, pp. 15378–15380, Dec. 1998.

[18] H. Kolm, “Solar-battery power source Quarterly Progress Report Solid State Research, Group 35,” Lexington, MA: MIT Lincoln Laboratory, 1956.

[19] B. Bitnar, “Silicon, germanium and silicon/germanium photocells for thermophotovoltaics applications,” *Semicond Sci Technol*, vol. 18, pp. 221–227, 2003.

[20] T. Bauer, *Thermophotovoltaics: Basic Principles and Critical Aspects of System Design*. Springer, 2011.

[21] M. A. Green, K. Emery, Y. Hishikawa, W. Warta, and E. D. Dunlop, “Solar cell efficiency tables (version 39),” *Progress in Photovoltaics: Research and Applications*, vol. 20, no. 1, pp. 12–20, Jan. 2012.

[22] C. Downs and T. E. Vandervelde, *Progress in infrared photodetectors since 2000.*, vol. 13, no. 4. 2013, pp. 5054–98.

[23] Lewis Fraas, J. Avery, J. Gee, and K. Emery, “Over 35% Efficient GaAs/GaSb Stacked Concentrator Cell Assemblies for Terrestrial Applications,” in *IEEE PV Specialist Conference*, 1990, p. 190.

[24] L. M. Fraas, H. X. Huang, S. Z. Ye, S. Hui, A. J, and B. R, “No Title,” in *3rd REL Conf. on the the Thermophotovoltaic Generation of Electricity*, 1997, pp. 33–40.

[25] a. P. Astakhova, B. E. Zhurtanov, a. N. Imenkov, M. P. Mikhailova, M. a. Sipovskaya, N. D. Stoyanov, and Y. P. Yakovlev, “Long-wavelength photodiodes based on n-GaSb/n-GaInAsSb/p-AlGaAsSb heterostructures,” *Technical Physics Letters*, vol. 33, no. 1, pp. 11–13, Jan. 2007.

[26] R. J. Wehrer, M. W. Wanlass, D. Taylor, B. Wernsman, J. J. Carapella, R. W. Schultz, S. P. Ahrenkiel, D. M. Wilt, M. W. Dashiell, R. R. Siergiej, S. D. Link, and R. L. Messham, “0.52 eV InGaAs/InPAs Thermophotovoltaic cells,” in *AIP CONFERENCE PROCEEDINGS*, 2004, pp. 445–452.

[27] E. V. Kunitsyna, I. a. Andreev, V. V. Sherstnev, T. V. L’vova, M. P. Mikhailova, Y. P. Yakovlev, M. Ahmetoglu (Afrailov), G. Kaynak, and O. Gurler, “Narrow gap III–V materials for infrared photodiodes and thermophotovoltaic cells,” *Optical Materials*, vol. 32, no. 12, pp. 1573–1577, Oct. 2010.

[28] V. A. Gevorkyan, V. M. Aroutiounian, K. M. Gambaryan, A. H. Arakelyan, I. a. Andreev, L. V. Golubev, Y. P. Yakovlev, and M. W. Wanlass, “The Growth of Low Band-Gap InAsSbP Based Diode Heterostructures for Thermo-Photovoltaic Application,” *AIP Conference Proceedings*, vol. 890, no. 2007, pp. 165–173, 2007.

[29] M. V Andreev, O. A. Khvostikov, V P Khvostikova, and E. V Oliva, “Low band gap Ge and InAsSbP/InAs-based TPV cells,” in *Thermophotovoltaic Generation of Electricity: 5th Conf. on Thermophotovoltaic Generation of Electricity (AIP Conf. Proc. 653)*, 2003, p. pp 383–91.

[30] A. Krier, M. Yin, M. R. J., and S. E. Krier, “Low bandgap InAs-based thermophotovoltiac cells for heat-electricity onversion,” *Journal of Electronic Materials*, vol. 45, pp. 2726–2830, 2016.

[31] M. G. Mauk, “Survey of Thermophotovoltaic (TPV) Devices,” in *Mid-infrared Semiconductor Optoelectronics, Springer Series in Optical Sciences*, 2006, pp. 673–738.

[32] L. B. Karlina, A. S. Vlasov, M. M. Kulagina, and N. K. Timoshina, “Thermophotovoltaic Cells Based on In 0 . 53 Ga 0 . 47 As / InP Heterostructures,” vol. 40, no. 3, pp. 346–350, 2005.

[33] A. W. Bett and O. V. Sulima, “GaSb photovoltaic cells for applications in TPV generators,” *Semiconductor Science and Technology*, vol. 18, pp. S184–S190, 2003.

[34] M. K. Hudait, M. Brenner, and S. a. Ringel, “Metamorphic In0.7Al0.3As/In0.69Ga0.31As thermophotovoltaic devices grown on graded InAsyP1−y buffers by molecular beam epitaxy,” *Solid-State Electronics*, vol. 53, no. 1, pp. 102–106, Jan. 2009.

[35] P. S. Dutta, J. M. Borrego, H. Ehsani, G. Rajagopalan, I. B. Bhat, R. J. Gutmann, G. Nichols, and P. F. Baldasaro, “GaSb and Ga[1 - x]In[x]Sb Thermophotovoltaic Cells using Diffused Junction Technology in Bulk Substrates,” *AIP Conference Proceedings*, vol. 653, no. 1, pp. 392–401, 2003.

[36] H. K. Choi, C. A. Wang, G. W. Turner, M. J. Manfra, D. L. Spears, G. W. Charache, L. R. Danielson, H. K. Choi, C. A. Wang, G. W. Turner, M. J. Manfra, and D. L. Spears, “High-performance GaInAsSb thermophotovoltaic devices with an AlGaAsSb window High-performance GaInAsSb thermophotovoltaic devices with an AlGaAsSb window,” vol. 3758, no. 1997, pp. 1–4, 2003.

[37] M. G. Mauk, O. V Sulima, J. A. Cox, and R. L. Mueller, “LOW-BANDGAP (0.3 to 0.5 eV) InAsSbP THERMOPHOTOVOLTAICS: ASSESSMENT FOR OPEN-CIRCUIT VOLTAGE IMPROVEMENTS,” in *3rd World Conference on Photovolloic Energy Conversion*, 2003, pp. 224–227.

[38] K. J. Cheetham, P. J. Carrington, N. B. Cook, and A. Krier, “Solar Energy Materials & Solar Cells Low bandgap GaInAsSbP pentanary thermophotovoltaic diodes,” *Solar Energy Materials and Solar Cells*, vol. 95, no. 2, pp. 534–537, 2011.

[39] M. Mauk, “Survey of thermophotovoltaic (TPV) devices,” *Mid-infrared Semiconductor Optoelectronics*, vol. 118, pp. 673–738, 2006.

[40] J. Joannapolous, S. Johnson, J. Winn, and R. Meade, *Photonic Crystals Modeling the Flow of Light Second Edition*. Princeton University Press, 2008.

[41] P. Russell, “Photonic Crystal Fibers,” vol. 299, no. JANUARY, pp. 358–363, 2003.

[42] O. Fraz, “Optical sensing with photonic crystal fibers,” vol. 459, no. 6, pp. 449–459, 2008.

[43] K. T. Posani, V. Tripathi, S. Annamalai, S. Krishna, R. Perahia, O. Crisafulli, K. T. Posani, V. Tripathi, S. Annamalai, and S. Krishna, “Nanoscale quantum dot infrared sensors with photonic crystal cavity,” *Applied Physics Letters*, vol. 88, 2006.

[44] J. Yang, M. Seo, I. Hwang, S. Kim, Y. Lee, J. Yang, M. Seo, I. Hwang, S. Kim, and Y. Lee, “Polarization-selective resonant photonic crystal photodetector,” *Applied Physics Letters*, vol. 93, 2008.

[45] S. Schartner, S. Golka, C. Pflugl, W. Schrenk, A. M. Andrews, T. Roch, and G. Strasser, “Band structure mapping of photonic crystal intersubband detectors,” *Applied Physics Letters*, vol. 89, 2006.

[46] “2D Photonic Crystals in Fiber Optics.” [Online]. Available: https://www.photonics.com/a25277/High-Power_Photonic_Crystal_Fiber_Lasers.

[47] C. M. Shemelya and T. E. Vandervelde, “Comparison of Photonic-Crystal-Enhanced Thermophotovoltaic Devices With and Without a Resonant Cavity,” *Journal of Electronic Materials*, vol. 41, no. 5, pp. 928–934, 2012.

[48] C. Shemelya, D. F. DeMeo, and T. E. Vandervelde, “Two dimensional metallic photonic crystals for light trapping and anti-reflective coatings in thermophotovoltaic applications,” *Applied Physics Letters*, vol. 104, no. 2, p. 021115, Jan. 2014.

[49] Corey M. Shemelya, “Photonics: Photodiodes and Metamaterials for Thermophotovoltaics and Photodetection Applications,” Tufts University, 2013.

[50] C. Shemelya, D. F. Demeo, T. E. Vandervelde, C. Shemelya, D. F. Demeo, and T. E. Vandervelde, “Two dimensional metallic photonic crystals for light trapping and anti-reflection coatings in thermophotovoltaic applications,” vol. 104, 2014.

[51] W. Shockley and H. Queisser, “Detailed Balance Limi of Efficiency of p-n Junction Solar Cells,” *Jounrla of APplied Physics*, vol. 32, pp. 510–519, 1961.

[52] G. D. Cody, “Theoretical maximum efficiencies for thermophotovoltaic devices,” vol. 58, no. 1, pp. 58–67, 1999.

[53] D. L. Chubb, *Fundamentals of Thermophotovoltaic Energy Conversion*. Amsterdam, Netherlands: Elsevier, 2007, p. 515.

[54] G. D. Cody, “Theoretical maximum efficiencies for thermophotovoltaic devices,” vol. 58, no. 1, pp. 58–67, 1999.

[55] P. F. Baldasaro, J. E. Raynolds, G. W. Charache, D. M. Depoy, C. T. Ballinger, T. D. M. Borrego, P. F. Baldasaro, J. E. Raynolds, G. W. Charache, D. M. Depoy, and C. T. Ballinger, “Thermodynamic analysis of thermophotovoltaic efficiency and power density tradeoffs Thermodynamic analysis of thermophotovoltaic efficiency and power density tradeoffs,” *Jounral of Applied Physics*, vol. 89, no. 2001, pp. 3319–3327, 2001.

[56] C. A. Wang, “Antimony Based III-V Thermophotovoltaic Devices,” *Contract*, 2004.

[57] R. K. Huangrajeev, J. R. J. Manfra, M. K. Connors, L. J. Missaggia, G. W. Turner, R. J. Ram, M. J. Manfra, M. K. Connors, L. J. Missaggia, and G. W. Turner, “Heterojunction thermophotovoltaic devices with high voltage factor Heterojunction thermophotovoltaic devices with high voltage factor,” vol. 046102, pp. 1–4, 2007.

[58] P. Martyniuk, M. Kopytko, and A. Rogalski, “Barrier infrared detectors,” *Opto-Electronics Review*, vol. 22, no. 2, pp. 127–146, 2014.

[59] D. Z. Ting, C. J. Hill, A. Soibel, J. Nguyen, S. A. Keo, M. C. Lee, J. M. Mumolo, J. K. Liu, and S. D. Gunapala, “Antimonide-based barrier infrared detectors,” in *Infrared Technology and Applications XXXVI, Proc. of SPIE Vol. 7660*, 2010, vol. 7660, pp. 1–14.

[60] P. Klipstein, “Depletionless photodiode with suppressed dark current and method for producing the same,” U.S. Patent 77956402003.

[61] P. Klipstein, O. Kin, S. Grossman, N. Snapi, I. Lukomsky, D. Aronov, M. Yassen, A. Glozman, T. Fishman, E. Berkowicz, O. Magen, I. Shtrichman, and E. Weiss, “XBn barrier photodetectors based on InAsSb with high operating temperatures,” *Optical Engineering*, vol. 50, no. 6, 2011.

[62] J. B. Rodriguez, E. Plis, G. Bishop, Y. D. Sharma, H. Kim, L. R. Dawson, S. Krishna, J. B. Rodriguez, E. Plis, G. Bishop, Y. D. Sharma, H. Kim, L. R. Dawson, and S. Krishna, “nBn structure based on InAs/GaSb type-II strained layer superlattices,” *Applied Physics Letters*, vol. 91, 2007.

[63] S. Maimon and G. W. Wicks, “nBn detector , an infrared detector with reduced dark current and higher operating temperature,” *Applied Physics Le*, vol. 89, 2006.

[64] P. Klipstein, O. Kin, S. Grossman, N. Snapi, I. Lukomsky, D. Aronov, M. Yassen, A. Glozman, T. Fishman, E. Berkowicz, O. Magen, I. Shtrichman, and E. Weiss, “XBn barrier photodetectors based on InAsSb with high operating temperatures,” *Optical Engineering*, vol. 50, no. 6, 2011.

[65] P. Klipstein, "'XBn' barrier photodetectors for high sensitivity and high operating temperature infrared sensors," in *Proceedings of SPIE*, 2008, vol. 6940, p. The International Society for Optical Engineering.

[66] G. R. Savich, J. R. Pedrazzani, D. E. Sidor, and G. W. Wicks, "Benefits and limitations of unipolar barriers in infrared photodetectors," *Infrared Physics and Technology*, vol. 59, pp. 152–155, 2013.

[67] G. R. Savich, J. R. Pedrazzani, D. E. Sidor, S. Maimon, and G. W. Wicks, "Use of unipolar barriers to block dark currents in infrared detectors," in *Infrared Technology and Applications XXXVII*, 2011.

[68] S. Maimon and G. W. Wicks, "nBn detector, an infrared detector with reduced dark current and higher operating temperature," *Applied Physics Letters*, vol. 89, no. 15, p. 151109, 2006.

[69] P. Klipstein, O. Klin, S. Grossman, N. Snapi, I. Lukomsky, D. Aronov, M. Yassen, A. Glozman, T. Fishman, E. Berkowicz, O. Magen, I. Shtrichman, and E. Weiss, "XBn barrier photodetectors based on InAsSb with high operating temperatures," *Optical Engineering*, vol. 50, no. 6, 2011.

[70] M. Razeghi, *Technology of Quantum Devices*. Springer Science and Business Media, 2010.

[71] C. M. Ciesla, B. N. Murdin, R. A. Pidgeon, R. A. Stradling, C. C. Phillips, M. Livingstone, I. Galbraith, D. A. Jaroszynski, C. J. G. M. Langerak, P. J. P. Tang, and M. J. Pullin, "Suppression of auger recombination in arsenic-rich InAs1-xSbx strained layer superlattices," *Journal of Applied Physics*, vol. 80, 1996.

[72] E. R. Youngdale, J. R. Meyer, C. a. Hoffman, F. J. Bartoli, C. H. Grein, P. M. Young, H. Ehrenreich, R. H. Miles, and D. H. Chow, "Auger lifetime enhancement in InAs–Ga1−xInxSb superlattices," *Applied Physics Letters*, vol. 64, no. 23, p. 3160, 1994.

[73] D. Z.-Y. Ting, A. Soibel, L. Hoglund, J. Nguyen, C. J. Hill, A. Khoshakhlagh, and S. D. Gunapala, "Type-II superlattice infrared detectors," in *Semiconductors and Semimetals*, vol. 84, 2011, pp. 1–57.

[74] S. Adachi, "Material parameters of In1-xGaxAsyP1-y and related binaries," *Journal of Applied Physics*, vol. 53, no. 8775, 1982.

[75] B. Nguyen, D. Hoffman, E. K. Huang, and M. Razeghi, "Very high performance LWIR and VLWIR Type-II InAs/GaSb superlattice photodiodes with M-structure barrier," in *Proceeding of SPIE*, 2008.

[76] C. H. Grein, P. M. Young, and H. Ehrenreich, “Theoretical performance of InAs/ InxGa1−xSb superlattice-based midwave infrared lasers,” *Journal of applied physics*, vol. 76, 1994.

[77] M. E. Flatte, C. H. Grein, J. T. Olesberg, T. C. Hasenberg, and T. F. Boggess, “Temperature dependence of Auger recombination in a multilayer narrow-band-gap superlattice,” vol. 58, no. 19, pp. 47–54, 1998.

[78] “NextNano.” [Online]. Available: http://www.nextnano.com/.

[79] D. Martin, C. Algora, D. Martín, and C. Algora, “Temperature-dependent GaSb material parameters for reliable thermophotovoltaic cell modelling,” *Semiconductor Science and Technology*, vol. 19, no. 8, pp. 1040–1052, 2004.

[80] G. Stollwerck, O. V Sulima, and A. W. Bett, “Characterization and Simulation of GaSb Device-Related Properties,” vol. 47, no. 2, pp. 448–457, 2000.

[81] D. Martin and C. Algora, “Key Issues for an Accurate Modelling of GaSb TPV Converters,” *AIP Conference Proceedings*, vol. 653, no. 1, pp. 442–451, 2003.

[82] L. Tang, L. M. Fraas, Z. Liu, C. Xu, and X. Chen, “Performance Improvement of the GaSb Thermophotovoltaic Cells With n-Type Emitters,” vol. 62, no. 9, pp. 2809–2815, 2015.

[83] K. Yang., J. East, and G. Haddad, “Numerical Modeling of Abrupt Heterojunctions Using a Thermionic-Field Emission Boundary Condition,” *Solid-State Electronics*, vol. 36, no. 3, pp. 321–330, 1993.

[84] S. Birner, “The Multi-Band k·p Hamiltonian for Heterostructures: Parameters and Applications,” in *Multi-Band Effective Mass Approximations*, K. T. Ehrhardt M., Ed. Springer, Cham, 2014.

[85] T. Zibold, “Semiconductor based quantum information devices : Theory and simulations,” 2007.

[86] T. Andlauer and P. Vogl, “Full-band envelope-function approach for type-II broken-gap superlattices,” no. May, pp. 1–7, 2009.

[87] J. H. Li, D. W. Stokes, J. C. Wickett, O. Caha, K. E. Bassler, S. C. Moss, J. H. Li, D. W. Stokes, J. C. Wickett, O. Caha, and K. E. Bassler, “Effect of strain on the growth of InAs / GaSb superlattices : An x-ray diffraction study Effect of strain on the growth of InAs / GaSb superlattices : An x-ray,” *Journal of Applied Physics*, vol. 107, no. 123504, 2010.

[88] J. Nguyen, A. Soibel, D. Z. Ting, C. J. Hill, M. C. Lee, S. D. Gunapala, J. Nguyen, A. Soibel, D. Z. Ting, C. J. Hill, M. C. Lee, and S. D. Gunapala, “Low dark current long-wave infrared InAs / GaSb superlattice detectors Low dark current long-wave infrared InAs / GaSb superlattice detectors,” vol. 051108, 2010.

[89] E. K. Huang, B. Nguyen, D. Hoffman, P. Delaunay, and M. Razeghi, “Inductively coupled plasma etching and processing techniques for type-II InAs / GaSb superlattices infrared detectors toward high fill factor focal plane arrays,” vol. 7222, pp. 1–8, 2009.

[90] L. Zhang, L. F. Lester, R. J. Shul, C. G. Willison, R. P. Leavitt, and L. Zhang, “Inductively coupled plasma etching of III – V antimonides in Inductively coupled plasma etching of III – V antimonides in BCl 3 / Ar and Cl 2 / Ar,” vol. 965, no. 1999, pp. 1–6, 2016.

[91] A. Hood, P. Delaunay, D. Hoffman, B. Nguyen, Y. Wei, M. Razeghi, A. Hood, P. Delaunay, D. Hoffman, and B. Nguyen, “Near bulk-limited R 0 A of long-wavelength infrared type-II InAs / GaSb superlattice photodiodes with polyimide surface passivation,” *Applied Physics Letters*, vol. 233513, no. 90, 2007.

[92] B. Klein, E. Plis, M. N. Kutty, N. Gautam, A. Albrecht, S. Myers, and S. Krishna, “Varshni parameters for InAs / GaSb strained layer superlattice infrared photodetectors,” *Journal of Physics D: Applied Physics*, vol. 44, 2011.

[93] J.-M. Masur, R. Rehm, J. Schmitz, L. Kirste, and M. Walther, “Four-component superlattice empirical pseudopotential method for InAs/GaSb superlattices,” *Infrared Physics & Technology*, vol. 61, pp. 129–133, Nov. 2013.

[94] N. Gautam, S. Myers, A. V Barve, S. Member, B. Klein, E. P. Smith, D. R. Rhiger, H. S. Kim, Z. Tian, S. Krishna, and S. Member, “Barrier Engineered Infrared Photodetectors Based on Type-II InAs / GaSb Strained Layer Superlattices,” vol. 49, no. 2, pp. 211–217, 2013.

[95] D. A. Ramirez, E. A. Plis, S. Myers, L. A. Treider, E. Garduno, P. Morath, V. M. Cowan, S. Krishna, and S. Llc, “High operating temperature midwave infrared (MWIR) photodetectors based on type II InAs / GaSb strained layer superlattice,” vol. 9226, pp. 1–8, 2014.

[96] M. Rzeghi, S. A. Pour, E. K. Huang, G. Chen, A. Haddadi, and B. M. Nguyen, “Type-II InAs / GaSb photodiodes and focal plane arrays aimed at high operating temperatures,” vol. 19, no. 3, pp. 261–269, 2011.

[97] G. Chen, A. Haddadi, A. Hoang, R. Chevallier, and M. Razeghi, “Demonstration of type-II superlattice MWIR minority carrier unipolar imager for high operation temperature application,” vol. 40, no. 1, pp. 45–47, 2015.

[98] I. Gasb, M. Razeghi, S. A. Pour, G. Chen, and A. Haddadi, “High-operating temperature MWIR photon detectors based on Type II,” in *SPIE Defense, Security, and Sensing*, 2011.

[99] M. Hostut, M. Alyoruk, T. Tansel, A. Kilic, R. Turan, A. Aydinli, and Y. Ergun, “Superlattices and Microstructures N-structure based on InAs / AlSb / GaSb superlattice photodetectors,” *SUPERLATTICES AND MICROSTRUCTURES*, vol. 79, pp. 116–122, 2015.

[100] O. Salihoglu, A. Muti, K. Kutluer, T. Tansel, R. Turan, Y. Ergun, A. Aydinli, O. Salihoglu, A. Muti, K. Kutluer, T. Tansel, and R. Turan, “‘ N ’ structure for type-II superlattice photodetectors,” vol. 101, no. 073505, 2012.

[101] O. Salihoglu, M. Hostut, T. Tansel, K. Kutluer, A. Kilic, M. Alyoruk, C. Sevik, R. Turan, Y. Ergun, and A. Aydinli, “Infrared Physics & Technology MWIR photodetectors,” *Infrared Physics and Technology*, vol. 59, pp. 36–40, 2013.

[102] C. Shemeya and T. E. Vandervelde, “Comparison of Photonic-Crystal-Enhanced Thermophotovoltaic Devices With and Without a Resonant Cavity,” vol. 41, no. 5, pp. 928–934, 2012.

[103] P. S. Dutta and H. L. B. Kumar, “The physics and technology of gallium antimonide : An emerging optoelectronic material The physics and technology of gallium antimonide : An emerging optoelectronic material,” *Journal of Applied Physics*, vol. 81, no. 1997, pp. 5821–5870, 1997.

[104] I. P.-T. Institute, “http://www.ioffe.ru/SVA/NSM/Semicond/.” .

[105] O. V Sulima and A. W. Bett, “Fabrication and simulation of GaSb thermophotovoltaic cells,” vol. 66, 2001.

[106] K. F. Longenbach, W. I. Wang, K. F. Longenbach, and W. I. Wang, “Molecular beam epitaxy of GaSb,” vol. 59, 1991.

[107] A. Y. Polyakov, M. Stam, A. G. M. G. Wilsonz, Q. F. Rai, R. J. Hillard, and A. Y. Polyakov, “High-resistivity GaSb grown by molecular-beam epitaxy High-resistivity GaSb grown by molecular-beam epitaxy,” vol. 1316, 1992.

[108] D. F. DeMeo, N. P. Latham, C. M. Shemelya, and T. E. Vandervelde, “metamaterial selective emitters for photodiodes,” in *SPIE OPTO*, 2014, p. 89820J–89820J–7.

[109] K. M. Schirm, P. Soukiassian, P. S. Mangat, and L. Soonckindt, “Schottky-barrier and interface formation of Cs/GaSb(110) and Rb/GaSb(110) at room temperature,” *Physics Review B*, vol. 49, no. 8, p. 5490, 1994.

[110] W. E. Spicer, I. Lindau, P. Skeath, C. Y. Su, and P. Chye, “Unified Mechanism for Schottky-Barrier Formation and II-V Oxide Interface States,” *Physics Review Letters*, vol. 44, no. 420, 1980.

[111] Z. M. Lu, D. Mao, L. Soonckindt, and A. Kahn, “Overlayer morphology and metallicity: Fromation of In/GaSb(110) barriers at room and low temperature,” *Journal of Vacuum Science & Technology A*, vol. 8, no. 3, p. 1988, 1990.

[112] N. Rahimi, A. A. Aragon, O. S. Romero, D. M. Shima, T. J. Rotter, D. Sayan, G. B. F. Lester, N. Rahimi, A. A. Aragon, O. S. Romero, D. M. Shima, T. J. Rotter, S. D. Mukherjee, G. Balakrishnan, and L. F. Lester, “Low resistance palladium / molybdenum based ohmic contacts to n-GaSb grown on GaAs,” vol. 108, pp. 1–6, 2014.

[113] J. A. Robinson and S. E. Mohney, “An improved In-based ohmic contact to n-GaSb,” *Solid-State Electronics*, vol. 48, no. 9, pp. 1667–1672, 2004.

[114] A. Subekti, V. W. L. Chin, T. L. Tansley, and I. I. June, “Ohmic contacts to n-type and p-type GaSb,” vol. 39, no. 3, pp. 329–332, 1996.

[115] C. Heinz, “Ohmic contacts to p-type and n-type GaSb,” *International Journal of Electronics*, vol. 54, no. 2, pp. 247–54, 1983.

[116] X. Li and A. G. Milnes, “Ohmic Contacts Formed on n-GaSb by,” vol. 143, no. 3, pp. 1014–1020, 1996.

[117] M. Rolland, S. Gaillard, E. Villemain, D. Rigaud, M. Valenza, M. Rolland, S. Gaillard, E. Villemain, D. Rigaud, M. V. Low, and H. A. L. Id, “Low noise ohmic contacts on n and p type GaSb To cite this version :,” vol. 3, no. 9, pp. 1825–1832, 1993.

[118] E. Villemain, S. Gaillard, M. Rolland, and A. Joullie, “Characterization of ohmic contacts on n- and p-type GaSb,” vol. 20, pp. 162–164, 1993.

[119] A. Vogt, H. Hartnagel, G. Miehe, H. Fuess, and J. Schmitz, “Electrical and microstructure analysis of ohmic contacts to p- and n-type GaSb, grown by

molecular beam epitaxy," *Journal of Vacuum Science & Technology B*, vol. 14, no. 6, pp. 3514–3519, 1996.

[120] A. Vogt, A. Simon, and H. L. Hartnagel, "Ohmic contact formation mechanism of the PdGeAu system on n-type GaSb grown by molecular beam epitaxy," *Journal of APplieds Physics*, vol. 83, 1998.

[121] J. Sigmund, M. Saglam, A. Vogt, H. L. Hartnagel, and V. Buschmann, "Microstructure analysis of ohmic contacts on MBE grown n-GaSb and investigation of sub-micron contacts," vol. 228, pp. 625–629, 2001.

[122] K. Varblianska, K. Tzenev, and T. Kotsinov, "Pd-Based Ohmic COntacts to n-GaSb," *PHYSICA STATUS SOLIDI A-APPLIED RESEARCH*, vol. 163, no. 2, pp. 387–393, 1997.

[123] A. Piotrowska, T. Piotrowski, S. Kasjaniuk, M. Guziewicz, S. Gierlotka, X. W. Lin, M. S. Division, and S. Kwiatkowski, "INTERACTION OF AU WITH GaSb AND ITS IMPACT ON THE FORMATION OF OHMIC CONTACTS," vol. 87, no. 2, pp. 419–422, 1995.

[124] S. A. A. B. K. K. S. Priyabadini and M. Amann, "Low-resistive sulphur-treated ohmic contacts to n-type InAsSb," no. June, pp. 259–263, 2009.

[125] C. Lauer, O. Dier, and M. Amann, "Low-resistive metal/n + -InAsSb/n-GaSb contacts," 2006.

[126] R. K. Huang, C. A. Wang, C. T. Harris, M. K. Connors, and D. A. Shiau, "Ohmic Contacts to n-Type GaSb and n-Type GaInAsSb," vol. 33, no. 11, 2004.

[127] S. K. Noh, J. O. Kim, and S. J. Lee, "A Modified Approach to Determine the Hall Parameters of Epitaxial GaSb Grown on a Conductive GaSb Substrate," vol. 55, no. 4, pp. 1331–1334, 2009.